RECONSTRUCTING IONOSPHERIC TEC OVER SOUTH AFRICA USING SIGNALS FROM A REGIONAL GPS NETWORK

A thesis submitted in fulfillment of
the requirements for the degree

DOCTOR OF PHILOSOPHY

of

RHODES UNIVERSITY

by

BDL Opperman

28 November 2007

Author's declaration

I hereby declare that I am the sole author of this thesis. This is a true copy of the thesis, including any required final revisions, as accepted by my examiners. I understand that my thesis may be made available to the public electronically.

Abstract

Radio signals transmitted by GPS satellites orbiting the Earth are modulated as they propagate through the electrically charged plasmasphere and ionosphere in the near-Earth space environment. Through a linear combination of GPS range and phase measurements observed on two carrier frequencies by terrestrial-based GPS receivers, the ionospheric total electron content (TEC) along oblique GPS signal paths may be quantified. Simultaneous observations of signals transmitted by multiple GPS satellites and observed from a network of South African dual frequency GPS receivers, constitute a spatially dense ionospheric measurement source over the region. A new methodology, based on an adjusted spherical harmonic (ASHA) expansion, was developed to estimate diurnal vertical TEC over the region using GPS observations over the region. The performance of the ASHA methodology to estimate diurnal TEC and satellite and receiver differential clock biases (DCBs) for a single GPS receiver was first tested with simulation data and subsequently applied to observed GPS data. The resulting diurnal TEC profiles estimated from GPS observations compared favourably to measurements from three South African ionosondes and two other GPS-based methodologies for 2006 solstice and equinox dates. The ASHA methodology was applied to calculating diurnal two-dimensional TEC maps from multiple receivers in the South African GPS network. The space physics application of the newly developed methodology was demonstrated by investigating the ionosphere's behaviour during a severe geomagnetic storm and investigating the long-term ionospheric stability in support of the proposed Square Kilometre Array (SKA) radio astronomy project. The feasibility of employing the newly developed technique in an operational near real-time system for estimating and dissimenating TEC values over Southern Africa using observations from a regional GPS receiver network, was investigated.

Acknowledgements

I wish to thank Grintek Ewation for whom the initial South African GPS-derived ionospheric research was undertaken by Dr Pierre Cilliers and myself. This project supplied the inspiration for my research which culminated in this thesis. I am indebted to Dr Pierre Cilliers, formerly professor in Electronic Engineering at the University of Pretoria and colleague since 2003, who pioneered this research field in South Africa and with whom I had the privilege of collaborating for many months. I found his high standard of work and strong analytical skills a continuous inspiration. I thank the Hermanus Magnetic Observatory for their financial assistance and motivation for undertaking this research project and for nurturing a working environment which is highly conducive to research. I am grateful to Richard Wannacott and Stephan Koch of the Chief Directorate Surveys and Mapping for graciously supplying all GPS data used in this research and kindly hosting our equipment for the near real-time TEC estimation system. I thank Dr Lee-Anne McKinnell for assistance with the ionosonde data and the use of the South African Bottomside Ionosphere Model and Dr Cathryn Mitchell, University Bath, for use of MIDAS computerised ionospheric tomography software. I extend my heartfelt appreciation to my supervisor, Dr Ray Haggard, for his wise guidance and time offered in reviewing my work.

Dedication

I lovingly dedicate this thesis to my wife, Karina, for her continuous support and consideration and to my sons, Ben-Louis and Philip, for bringing such joy into my life. This is for your patience and unconditional love. Ultimately, I dedicate this work to Jesus Christ, the Author and Finisher of my faith.

Glossary

ACTA	Australian Compact Array
ASHA	Adjusted Spherical Harmonic Analysis
CDSM	Chief Directorate Surveys and Mapping (South Africa)
CIT	Computerised Ionospheric Tomography
CODE	Centre for Orbit Determination Europe
CORS	Continuously Operating Reference Station
COSPAR	Committee on Space Research
CSHA	Conventional Spherical Harmonic Analysis
CSIR	Council for Scientific and Industrial Research
DCB	Differential Clock Bias
DoD	Department of Defence
DPS	Digisonde Portable Sounder
DST	Department of Science and Technology (South Africa)
Dst	Disturbance Storm Time
EM	Electromagnetic
ECEF	Earth-Centred-Earth-Fixed (coordinates)
ENU	East-North-Up (coordinates)
EOARD	European Office of Aerospace Research and Development
EUV	Extreme Ultraviolet
FARA	Fast Ambiguity Resolution Approach
GAIM	Global Assimilative Ionospheric Model
GEONET	GPS Earth Observation Network
GIM	Global Ionospheric Map
GOES	Geostationary Operational Environmental Satellite
GPS	Global Positioning System
GSHA	Global Spherical Harmonic Analysis
GTEC	GPS-derived Total Electron Content (also TEC)

GMRT	Giant Metrewave Radio Telescope
HartRAO	Hartebeesthoek Radio Astronomy
HF	High Frequency
HMO	Hermanus Magnetic Observatory
ICTP	International Centre for Theoretical Physics
IERS	International Earth Rotation Service
IGS	International GNSS Service
IMF	Interplanetary Magnetic Field
IONEX	IONosphere Map EXchange (Format)
IPP	Ionospheric Pierce Point
IRI	International Reference Ionosphere
ITEC	Ionosonde-derived Total Electron Content
JD	Julian Date (Day)
JPL	Jet Propulsions Laboratory
KAT	Karoo Array Telescope
LAMDA	Least Squares Ambiguity Decorrelation Algorithm
LOFAR	Low Frequency Array
LOS	Line-of-sight
MIDAS	Multi-Instrument Data Analysis System
MSLM	Modified single Layer Model
NASA	National Aeronautics and Space Administration
NOAA	National Oceanographic and Atmospheric Administration
NRF	National Research Foundation
NSF	National Science Foundation
PODAAC	Physical Oceanography Distributed Active Archive Center
RIM	Regional Ionospheric Model
RINEX	Receiver Independent Exchange Format
RIOmeter	Relative Ionospheric Opacity meter
RSA	Republic of South Africa

SA	Selective Availability
SABIM	South African Bottomside Ionospheric Model
SADC	Southern African Development Community
SANAE	South African National Antarctic Expedition
SANAP	South African National Antarctic Programme
SEC	Space Environment Center
SFE	Solar Flare Effect
SH	Spheric Harmonic
SHARE	Southern Hemisphere Auroral Radar Experiment
SHM	Spherical Harmonic Model
SI	International Standard
SKA	Square Kilometre Array
SLM	Single Layer Model
SLR	Satellite Laser Ranging
SI	Sudden Impulse
SSC	Sudden Storm Commencement
STEC	Slant Total Electron Content
T/P	TOPEX/Poseidon
TAI	International Atomic Time
TDT	Terrestrial Dynamic Time
TEC	Total Electron Content (also GTEC)
TIN	Triangular Irregular Network
TOPEX	Typhoon Operational Experiment
UNB	University of New Brunswick
URSI	International Union of Radio Science
USC	University of Southern California
UTC	Co-ordinated Universal Time
VLBI	Very Long Baseline Interferometry
VTEC	Vertical Total Electron Content

Table of Contents

List of Figures

List of Tables

Chapter 1

Introduction

1.1 Problem description

This thesis reports on the investigation into developing and implementing a methodology to supplement South African ionosonde observations with Total Electron Content (TEC) measurements quantified from navigation signals observed by a dense network of ground-based dual frequency GPS receivers. A spherical harmonic-based methodology was developed and evaluated using simulated measurements from the International Reference Ionosphere (IRI) (Bilitza, 2001) and the methodology performance was compared to measured ionosonde data and other GPS methodologies (Opperman *et al,*. 2007). The methodology was also used to investigate and report on South African ionospheric conditions in support of the South African bid for hosting the Square Kilometre Array (SKA) radio telescope (Opperman *et al,*. 2005) and to describe ionospheric dynamics during a geomagnetic storm. The feasibility of near real-time application of this methodology is also investigated and discussed.

1.2 Motivation

South African ionospheric research commenced after WWII with the installation of Wadley ionosondes in Cape Town, Johannesburg and Grahamstown (Hewitt *et al.*, 1947; Wadley, 1949; Gledhill and Szendrei, 1947). In time, other instruments such as Relative Ionospheric Opacity (RIO) meters (1960's) and, to some extent, the Antarctic-based Southern Hemisphere Dual Array Network (SUPERDARN) Radar (1996) were introduced and has served South African ionospheric research well (Gledhill 1947; Kühn 1968; Poole 1985; Stoker 1987; Gledhill 1991; Poole 1991; Wilson, 2002; Haggard, 2004; McKinnell, 2004). Ionosondes, however, remained the principal South African quantative ionospheric investigative instruments to date and were frequently

upgraded to state of the art and occasionally re-located (Baker 1993) to the present operational network of three Lowell Digisonde Portable Sounder (DPS) ionosondes located at Grahamstown (26.53ºE, 33.30ºS), Louisvale (21.20ºE, 28.50ºS) and Madimbo (30.90ºE, 22.40ºS), (**Figure 1**). Measurements from the South African ionosonde network, however, remain relatively sparse with twenty-minute interval measurements operationally registered by three ionosondes approximately 1000 km apart. Advances in South African space physics research and related disciplines, however, require ionospheric information with better spatial and time resolution than was previously possible with the existing ionosonde network.

Densification of ionospheric measurements in time and space may be achieved by exploiting the ionospheric delay on GPS navigation signals, as observed by a network of ground-based dual-frequency GPS receivers. This technique has received wide-spread international attention since the 1980s and, following the work of Schaer and others (Schaer *et al.* 1995; Schaer *et al.* 1998; Schaer 1999), this technique is presently implemented operationally by several institutions and facilities to supply Global and (limited) Regional Ionospheric Maps with a more improved time and spatial resolution than is possible with sparsely distributed ionosonde measurements.

The feasibility of conducting GPS-based ionospheric research in South Africa was first investigated by Cilliers and the author (Cilliers *et al.*, 2003; Cilliers *et al*, 2004) during an investigative study into Computerised Ionospheric Tomography (CIT) for Grintek Ewation (Cilliers, 2003; Cilliers and Opperman, 2003; Opperman, 2003; Cilliers and Opperman, 2005). First results for constructing 2D Total Electron Content (TEC) maps from a South African network of GPS receivers were presented in 2004 (Opperman, 2004). With up to 350 TEC measurements per second available from an existing South African GPS network (**Figure 1**), it is feasible to create high time and spatial resolution 2D TEC maps at 0.25ºx0.25º resolution in longitude-latitude and one minute in time; a significant improvement over present publicly available products. The development of a new GPS-derived methodology and the first-time application of this technique to South African circumstances is the focus of this thesis.

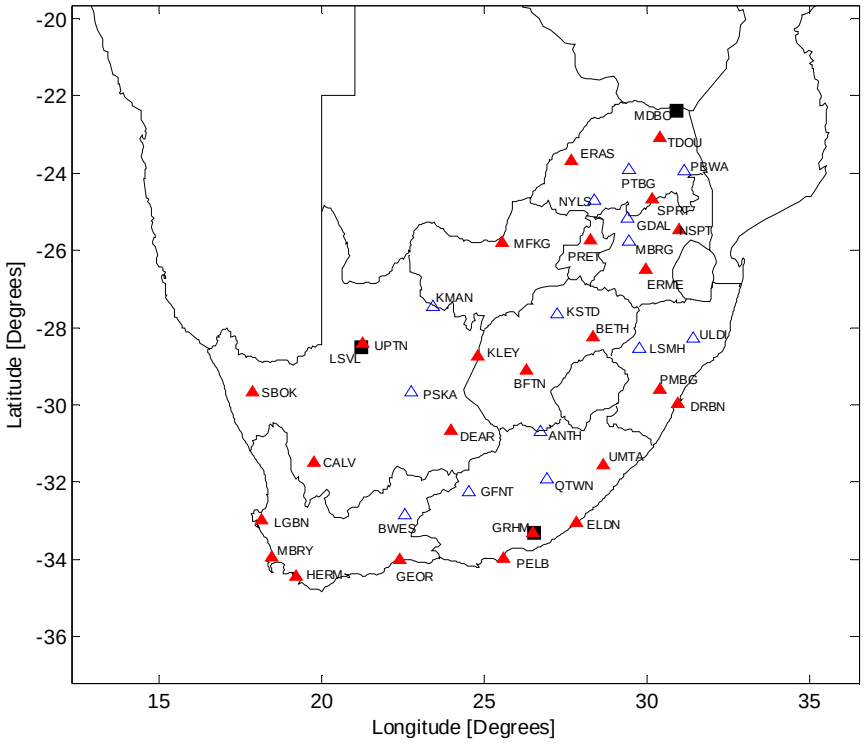

Figure 1. CDSM GPS network. Solid (red) triangles represent real-time receivers and blue (open) triangles represent off-line receivers. The three ionosondes are indicated as black squares. Note the co-located GPS receivers at Grahamstown and Louisvale ionosondes. An explanation of the receiver codes is given in Appendix B.

1.3 Thesis layout

This thesis is structured around the following chapters: Introduction and problem description (Chapter 1), Ionosophere structure (Chapter 2), Wave propagation and GPS theory (Chapter 3), GPS-based ionospheric models (Chapter 4), Model development and evaluation (Chapter 5), Application to radio astronomy (Chapter 6), Application to ionospheric response to a geomagnetic storm (Chapter 7) and Conclusions and future work (Chapter 8).

Chapter 2

Ionosphere structure and conventional measurements

2.1 Introduction

Balfour Stewart was the first person to postulate an ionosphere when, in 1882, he attributed currents in the upper atmosphere as the probable origin of the electric currents that produced the solar-controlled variation in the Earth's magnetic field, measured at the Earth's surface (Kivelson and Russel, 1995). Proving this assertion ultimately relied on the development of radio science stemming from the theoretical and experimental work of Heinrich Hertz (1893) and James Clerk-Maxwell (1873) into radio waves and electromagnetism, respectively (Hunsucker, 1991). The presence of such an upper-atmosphere electric layer was "accidently" demonstrated in 1901 when Guglielmo Marconi used a simple spark producing radio transmitter in successfully transmitting radio signals between Poldhu in Cornwall, UK and St John's in Newfoundland, Canada. To explain Marconi's 3500 km transatlantic transmissions, Heaviside and Kennely independently postulated the existence of a highly conductive ionosphere in 1902. Subsequent research revealed that Marconi's signal was reflected at least twice from the ionosphere along the transmission path. The existence of this *Heaviside-Kennelly* layer was experimentally proved by Appleton and Barnett and Breit and Tuve in 1926 during their respective experiments in determining the layer's height and charge composition from reflected radio signals. The three different layers discovered through the course of their work were named E, F and D after Appleton's designation of the vectors reflected from the different layers (Kivelson and Russel, 1995). Appleton and Hartree's work on radio propagation ultimately led to the development of the Appleton-Lassen generalised equation for determining the refractive index of an electromagnetic wave propagating through a dispersive medium such as the ionosphere (Rishbeth and Garriott , 1969).

Today, radio science remains the primary tool for obtaining measurements of the ionosphere and the original methods of Breit and Tuve, using short, vertically directed radio frequency pulses and inferring the height of the electrically reflecting layer from timing the arrival of the reflected signal, is still used in sounding the ionosphere (Kivelson and Russel, 1995).

2.2 Structure and composition of the ionosphere

The ionosphere is the region of ionised plasma extending 80-1200 km above the Earth's surface and forms the transition region between the neutral atmosphere and the fully ionized magnetospheric plasma (Baumjohann, 1999). The ionosphere is constituted of free electrons and ions which are produced during interaction of extreme ultra violet (EUV) and X-ray radiation with upper atmosphere neutral gas during *ionisation*, a process involving the stripping of electrons from neutral atoms in the atmosphere to form positively charged ions and negatively charged electrons. The net value of the number of free ions and electrons in the ionosphere is determined by the rate at which specific species of ions recombine with electrons to form neutral atoms, a process called *recombination* (McNamara, 1991). Two types of recombination are involved:

Radiative recombination. Electrons combine directly with ions, converting them into neutral atoms and emmitting a photon to conserve energy and momentum, *eg*,

$$O^+ + e^- \rightarrow O + \text{photon}$$

Dissociative recombination is a two-stage process. In the first stage, positive ions (*eg* N^+) interact with neutral molecules (*eg* O_2), replacing one of the atoms in the molecule and forming a neutral atom and a positively charged molecular ion, *eg*

$$N^+ + O_2 \rightarrow NO^+ + O$$

In the second stage, electrons combine with the newly formed molecular ion, forming two neutral atoms

$$NO^+ + e^- \rightarrow N+O$$

The dissociative recombination rate is about 1000 faster than the radiative recombination, resulting in much shorter lifetime for molecular ions than for atomic ions. Due to molecular ions' short lifespan, when their production is rapidly reduced at night, rapid recombination quickly reduces the plasma concentration. The O^+ at higher altitudes often survives the night (Kelley and Heelis, 1989). Daytime ionisation involving UV radiation is termed *photoionisation*. Because different gas atoms and molecules are more abundant in some regions of the neutral atmosphere than others, ionisation and recombination of the different species result in differing electron densities concentrated at different layers of the ionosphere. These layers are called the D, E and F regions (**Figure 2**) and their structure and composition are briefly discussed.

2.2.1 D-layer

The D-layer peaks at 90 km above the Earth. Ionisation is due to the Lyman alpha-hydrogen radiation at 121.5 nm ionising nitric oxide (NO). During periods of high solar activity (50 sunspots or more), hard X-rays (< 1nm) ionise N_2 and O_2 in this region. The maximimum electron density at noon reaches $1.5x10^4$ cm^{-3}. Recombination is high in this region with a resulting low net ionisation. High frequency (HF) radio waves are subsequently not reflected by this layer. The D-region is mainly responsible for HF absorption around 10 MHz and below with smaller absorption at night and greatest at midday. The D-layer greatly diminishes after sunset, but remains due to galactic cosmic rays.

2.2.2 E-Layer

The E-layer peaks at 110 km above the Earth with noon peak electron density values of $1.5.10^5$ cm^{-3} and nighttime highs of less than $1x10^4$ cm^{-3}. Ionisation is due to soft X-rays (1-10 nm) and ultraviolet (UV) solar radiation of molecular Oxygen (O_2). Nighttime E is due to electron and meteor bombardment.

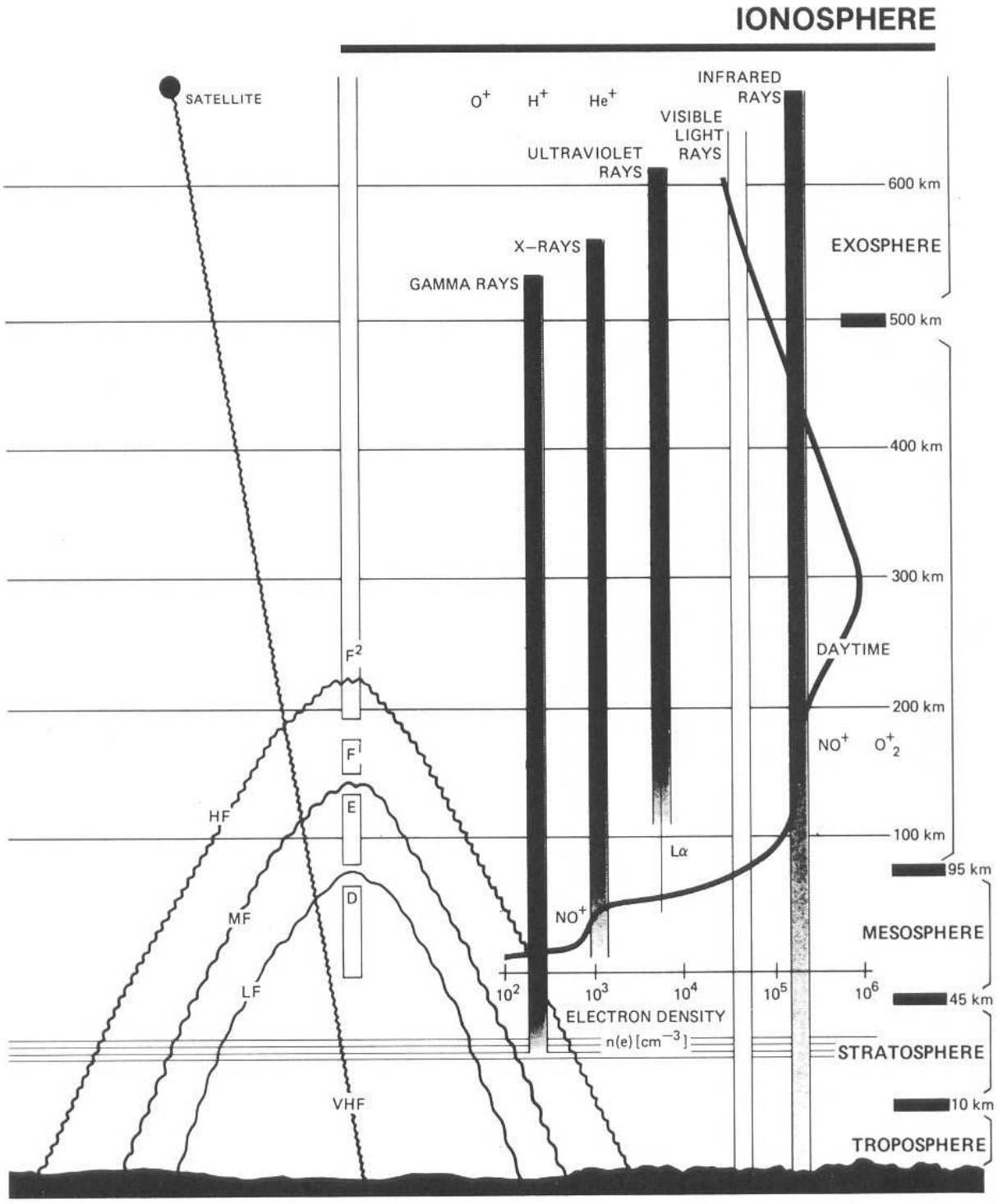

Figure 2. Structure and composition of the Earth's ionosphere. (Hunsucker, 1991)

2.2.3 F_1-layer

The F_1-layer peaks at 200 km above the Earth with noon peak electron density of $2.5x10^5$ cm^{-3}. It dissapears at night when combining with the F_2-layer to form the nighttime F-layer. Ionisation of atomic oxygen (O) by Lyman continuum or by He emmission lines, probably accompanied by N_2 ionisation which dissapears after sunset. Most of the ionisation is in molecular form and disappears by dissociative recombination.

2.2.4 F_2-layer

The F_2-layer peaks at about 300 km with peak electron density values of 10^6 cm^{-3} (noon) and 10^5 cm^{-3} (night). The F_2 layer's height and electron density is highly variable and large daily, seasonal and sunspot-cycle variations are combined with general erratic behaviour. Ionisation is due to extreme ultraviolet radiation (EUV) (10-100 nm) solar radiation of atomic oxygen (O). The ionosphere's highest electron density values are present in the F2-layer.

2.3 Parameters relevant to ionospheric measurements

The definitions of ionospheric and solar parameters and concepts relevant to this study are briefly presented:

f_oF_2 : The critical frequency of the F_2 layer

N_mF_2: The maximum electron density of the F_2 layer

h_mF_2 : The F_2 peak electron density height

K-index A three-hourly quasi-logartithmic local index of geomagnetic activity relative to an assumed quiet day curve for the recording site. The K-index measures the deviation of the most disturbed magnetic horizontal component and is an indicator of geomagnetic storm intensity. The index range is from 0-9 with 9 inidicating severe geomagnetically disturbed conditions.

K_p-index. A three-hourly planetary (global) geomagnetic index of activity based on the K-index of 12 or 13 stations distributed across the globe.

SSN The Sunspot number is an indication of solar activity and is calculated from the number of individual sunspots on the Sun and the number of sunspot groups. High SSN values indicate high solar activity. The Sun experiences an 11-year sunspot cycle with periods of relative high (Solar max) and relative low (Solar min) SSNs as illustrated in **Figure 3.**

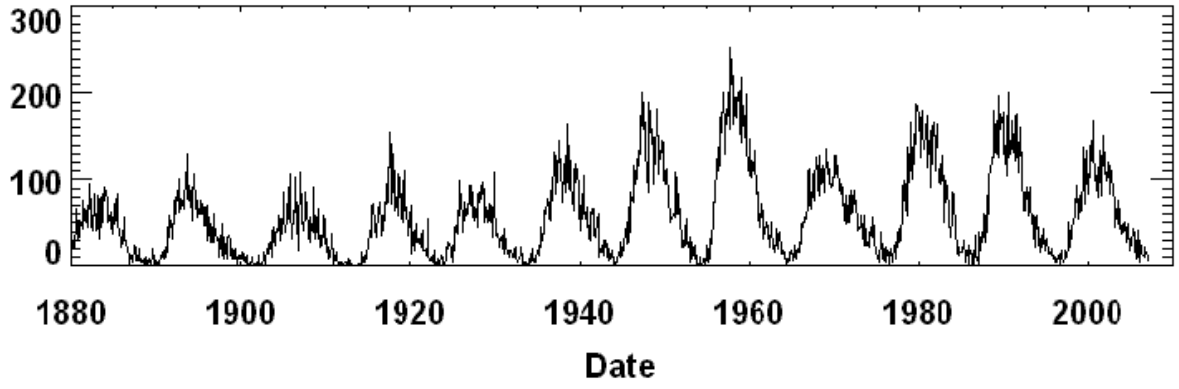

Figure 3. Time series of sunspot number observations illustrating the 11-year SSN cycle. Note the Solar maxima and minima. Image courtesy of NASA.

2.4 Ionospheric variation

As the ionosphere owes its existence to the Sun as the main ionisation energy source, the ionosphere naturally varies with time of day, season and geographic position. The following major variations are briefly discussed.

2.4.1 Diurnal variation

The day-night variation due to the Earth's rotation. Nighttime electron densities are much lower than daytime values, because of higher recombination rates in the absence of a radiation source. Daytime electron densities typically reach their peak at two hours past local noon due to the Earth's atmosphere lagging two hours behind the solid Earth's rotation.

2.4.2 Seasonal variation

At different times of year the Sun is vertically above different geographic locations. At equinox noon (March 21, Sep 23) the Sun is vertically above observers at the equator and vertically above observers at the Tropics of Capricon and Cancer on solstice dates (21 December, 21 June). As vertical illumination from the Sun results in higher ionisation rates, higher electron density concentrations are observed at these locations on these dates than at other locations.

2.4.3 Latitudinal variation

Similar to diurnal and seasonal variation, the Sun's position relative to the atmosphere plays a significant role in latitudinal variation of ionospheric densities. The solar zenith angle, χ, the angle measured from an observer's local vertical to the Sun, determines the intensity of ionisation where locations with small zenith angles are exposed to higher radiation rates. The Sun's zenith angle at the Tropic of Capricorn (23.5°S) at noon on 21 March (sourthern Autumn equinox) will be 47°, with expected lower ionisation rates and densities than at the Tropic of Cancer where the Sun will be vertically overhead (zenith angle of 0°).

2.4.4 Solar activity variation

Refers to the ionosphere's response to increased sunspot activity or sporadic phenomana like coronal mass ejections, solar flares or X-ray flares, all of which introduce raised levels of radiation, resulting in increased plasma densities in the ionosphere. As discussed in paragraph 2.3, the Sun exhibits an 11-year sunspot cycle with periods of high and low sunspot activity. As plasma production in the ionosphere is proportionate to sunspot numbers, the ionospheric densities follow the 11-year sunspot cycle. This is aptly illustrated by the long-term f_oF_2 variation measured at Grahamstown, South Africa and illustrated in **Figure 4**.

2.4.5 Equatorial anomaly

The equatorial anomaly is a region of high electron density distributed symmetrically at 15° around the geomagnetic equator. This anomaly is also know as the "fountain effect".

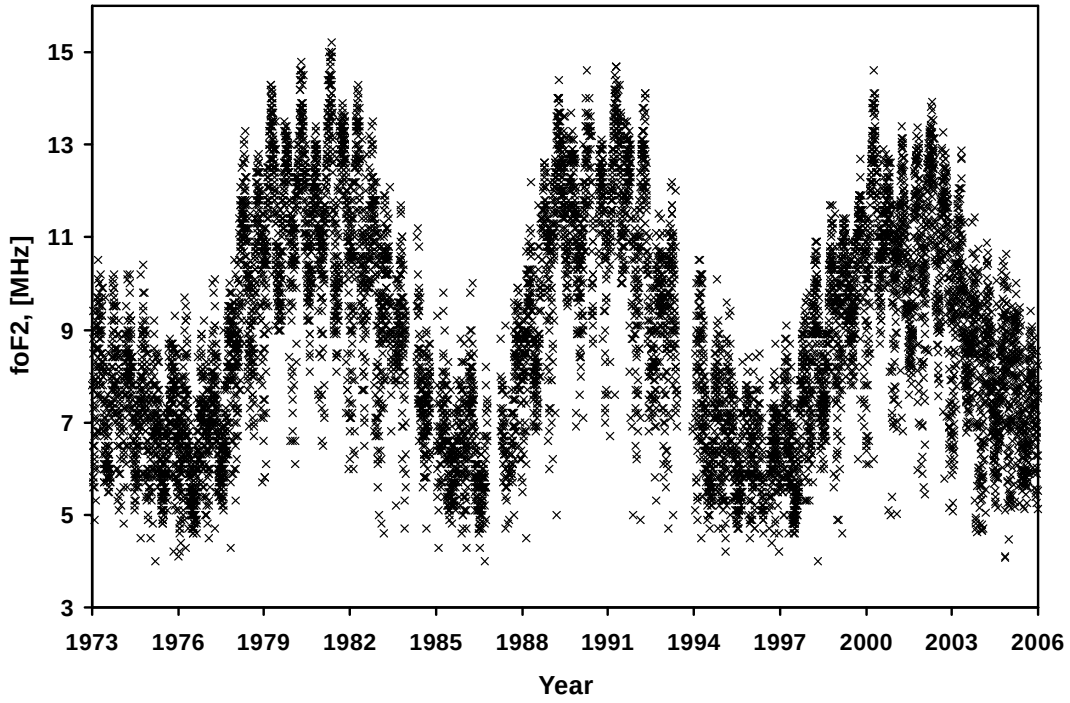

Figure 4 The variation of 10h00 UT (12h00 SAST) f_oF_2 values from the Grahamstown station for the period 1973 to 2005. Note the solar cycle variation. Image courtesy of Lee-Anne McKinnell, Hermanus Magnetic Observatory.

2.5 Conventional ionospheric measurements

2.5.1 Ionosonde

In South Africa vertical electron density profiles are measured at 15-30 minute intervals from three Lowell DPS ionosondes located respectively at Grahamstown (26.53ºE, 33.30ºS), Louisvale (21.20ºE, 28.50ºS) and Madimbo (30.90ºE, 22.40ºS). These presently constitute the only operational measurements of the ionosphere over South Africa. An ionospheric sounding constitutes a vertical sweep of the ionosphere by a pre-determined frequency band (< 30 MHz). During a sounding, electron density values are calculated from reflected radio waves corresponding

to the density-dependent critical plasma frequency, f_p ,of the ionised plasma and density heights are inferred from the time-delay of the reflected radio wave (**Figure 5**). The relation between the electron density, N_e, and density-dependent critical plasma frequency, f_p, is given by (Chen, 1984)

$$N_e = \frac{m(2\pi f)^2 \varepsilon_0}{e^2} \qquad 2.1$$

where

N_e Electron density (number of electrons/m^3)

f Reflected radio frequency (Hz) $f = f_p$

e, m Electron charge and mass respectively (1.6022x10^{-19} C, 9.1095x10^{-31} kg)

ε_0 Vacuum permittivity (8.854x10^{-12} F.m^{-1})

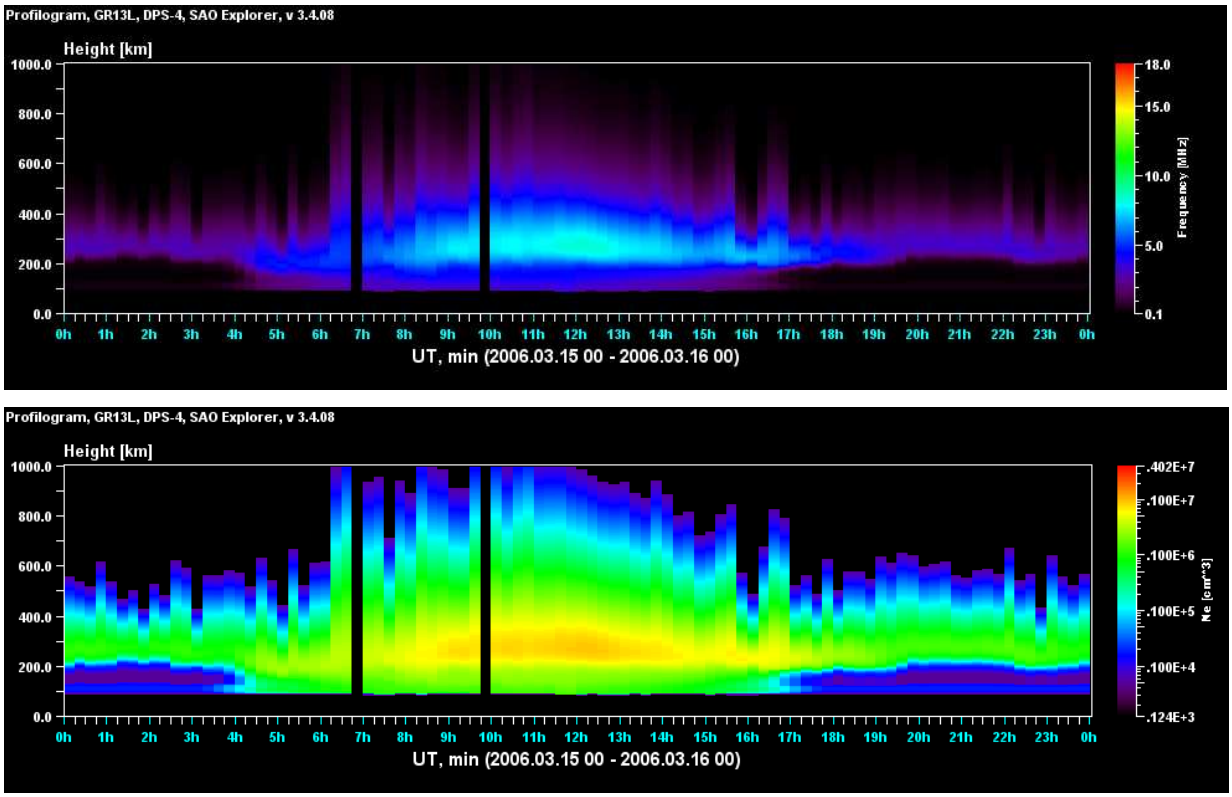

Figure 5. Profilogram illustrating reflected frequency (top) and corresponding electron density (bottom) of the lower ionosphere as observed by the Grahamstown ionsonde on 15 March 2006.

The height z_i, at which the frequency-dependent electron density value, $N_e^i(f_i)$ occurs, is calculated from the following parameters (Huang and Reinisch, 1996)

f_s Starting frequency in MHz,

f_m Ending frequency in MHz,

z_m Peak height of the layer in km,

A_j Coefficients of the shifted Chebyshev polynomials in km

$$z_i = z_m + \sqrt{g_i} \times \sum_{j=0}^{4} A_j T_j^i$$

with

$$g_i = \frac{\ln\left(\frac{f_i}{f_m}\right)}{\ln\left(\frac{f_s}{f_m}\right)}$$

where g_i is a scaling factor associated with the i^{th} reflected frequency, f_i and T_j^i are the shifted Chebyshev polynomials for j=1, … 4:

$$T_0^i = 1$$
$$T_1^i = 2g_i - 1$$
$$T_j^i = 2(2g_i - 1)\,T_{j-1}^i - T_{j-2}^i$$

The calculated electron densities and associated heights constitute an electron density profile of the bottomside ionosphere up to F_2 peak density height (h_mF_2) (**Figure 6**). Signals above the F_2 peak density frequency (f_oF_2) are transmitted through the ionosphere. Top side profiles are extrapolated by fitting Chapman-α function to the measured bottomside profile (Reinisch and Huang, 2001).

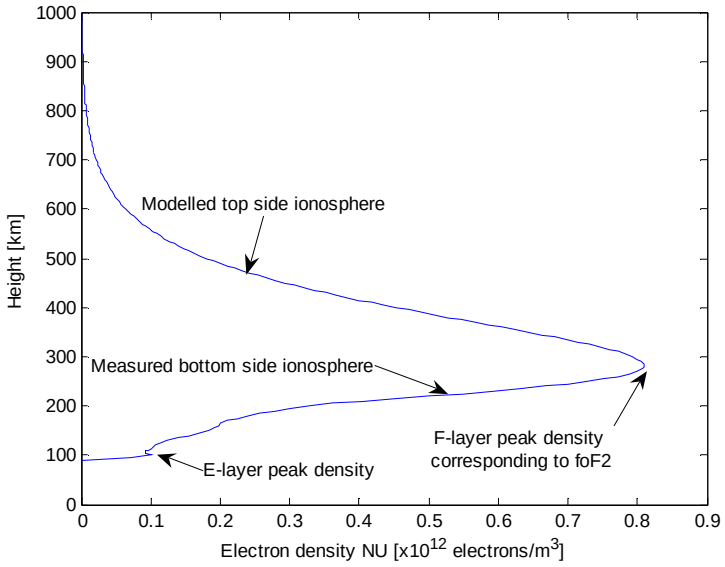

Figure 6. A typical profile of electron density vs height as obtained from ionosonde data. The specific profile pertains to 31 May 2005, 14:30 UT as recorded at the Grahamstown ionosonde. The bottomside profile (below the peak electron density value) is derived from a measured ionogram, while the top side profile is obtained by fitting a Chapman model to the peak electron density value. The total electron content (TEC) is obtained by integration of the density along the vertical height co-ordinate. For this profile the TEC was determined to be 19.6 TECU**.**

2.6 Ionospheric Models

2.6.1 Chapman function

Chapman profiles are generally used to describe seasonal, local time, and latitudinal variations of electron density and are given by (Rishbeth and Garriott, 1969)

$$N(z) = \frac{N_e(z)}{N_m F_2} \qquad 2.2$$

where $N_e(z)$, the electron density which applies at a solar zenith angle of χ is

$$N_e(z,\chi) = e^{\frac{1}{2}\left[1-z-e^{-z}\sec\chi\right]} \qquad 2.3$$

and N_mF_2 is the peak electron density of the F_2 layer. In Eq. 2.2, z is the normalised height given by

$$z = \frac{h'}{H} \qquad 2.4$$

In Eq. 2.4, *h'* is the distance above the F2-peak and *H* is the scale height

$$H = \frac{kT}{mg} \qquad 2.5$$

where

k: Boltzmann's constant

T: Kelvin temperature

m: molecular mass of gas

g: gravitational acceleration

2.6.2 International reference Ionosphere (IRI)

The IRI is an international project sponsored by the Committee on Space Research (COSPAR) and the International Union for Radio Science (URSI). For a given geographic location, time and date, the IRI model describes the elecron density, electron temperature, ion temperature and ion composition (O^+, H^+, He^+, NO^+, O_2^+), ion drift and Total Electron Content (TEC) in the altitude range 50 – 2 000 km. IRI provides monthly averages in the non-auroral ionosphere for magnetically quiet conditions. The major data sources for the IRI model development are the world-wide

network of ionosondes, incoherent scatter radar, satellite top side sounders and *in situ* instruments on several satellites and rockets (Bilitza, 2001).

2.6.3 South African Bottomside Ionospheric Model

The neural network-based SABIM ionospheric model (McKinnell 2003; McKinnell and Poole 2004) is the only regional ionospheric model specific to South Africa. It comprises a set of coefficients derived from a neural network trained with measured ionosonde data, geographic location, K_p index and sunspot number. Estimated coefficients permit the prediction of vertical electron density profiles over South Africa up to h_mF_2 within the input space defined by the training data sets.

Chapter 3

GPS-derived ionosphere

3.1 Introduction

The Global Positioning System (GPS) is a constellation of navigation satellites operated by the US Department of Defence (DoD). GPS became operational on 6 January 1980 and consists of at least 24 operational satellites distributed in 6 orbital planes with 4 satellites per plane. Each satellite has a 12-hour orbital period and 55° orbital inclination and orbits at approximately 20 200 km above the earth. Up to twelve satellites are visible at any given time. The time, position and velocity of all GPS satellites are continuously monitored by a network of ground-based radar and satellite laser ranging (SLR) instruments and reported to the master ground control which processes and regularly updates each satellite's ephemeris (positional information). GPS satellites transmit their individual ephemeris (and other information) on two carrier frequencies in the L-band for civilian use: f_1 = 1575.42 MHz (L_1) and f_2 = 1227.60 MHz (L_2). GPS receivers record accurate range measurements to each visible satellite from the observed signal travelling time (time-of-flight) and phase (number of wave cycles). From the known satellite positions and the observed range measurements it is possible to derive the GPS receiver position (position fix) by means of a least squares or Kalman filter solution (Strang and Borre, 1997). The dispersive nature of the electrically charged ionosphere, however, introduces a phase advance and group delay on observed GPS signals, causing errors in the measured range and, subsequently, errors in postion fix.

This chapter describes the theory of radio wave propagation through the electrically charged ionosphere and how the refraction-related errors may be exploited to obtain line-of-sight (LOS) measurements of the ionosphere along GPS signal paths.

3.2 GPS theory

GPS signals, like other electromagnetic (EM) waves, are affected by the electrically charged ionised plasma in the plasmasphere and ionosphere. The theory of EM interaction with a charged medium is well understood from such works by (Ginzberg, 1970; Chen, 1984; Davies, 1989; McNamara, 1991). Within the context of GPS signals propagating through the ionsosphere, this paragraph substantially relies on the work reported by (Hofmann-Wellenhof *et. al.*, 2001).

3.2.1 Wave propagation

The phase velocity of a single electromagnetic wave with wavelength λ and frequency f is denoted by

$$v_{ph} = \lambda f \tag{3.1}$$

The group velocity of a group of waves with slightly different frequencies is defined by

$$v_{gr} = -\frac{df}{d\lambda}\lambda^2 \tag{3.2}$$

The phase and group velocity can be related by taking the total differential of Eq. 3.1

$$dv_{ph} = fd\lambda + \lambda df \tag{3.3}$$

and rearranging as

$$\frac{df}{d\lambda} = \frac{1}{\lambda}\frac{dv_{ph}}{d\lambda} - \frac{f}{\lambda} \tag{3.4}$$

Substituting Eq. 3.4 into Eq. 3.2 yields

$$v_{gr} = -\lambda \frac{dv_{ph}}{d\lambda} + f\lambda \qquad 3.5$$

Noting that $v_{ph} = f\lambda$, Eq. 3.5 becomes the Rayleigh equation

$$v_{gr} = v_{ph} - \lambda \frac{dv_{ph}}{d\lambda} \qquad 3.6$$

Note. Eq. 3.2 implicitly contains dispersion, defined as the dependence of the phase velocity on the wavelength or frequency. Phase and group velocity are equal in non-dispersive media and equals the speed of light in a vacuum.

The refraction index of a medium is defined by

$$n = \frac{c}{v} \qquad 3.7$$

Applying this expression to phase and group velocity, the corresponding refractive indices n_{ph} and n_{gr} are obtained

$$v_{ph} = \frac{c}{n_{ph}},\ v_{gr} = \frac{c}{n_{gr}} \qquad 3.8$$

Differentiation of phase velocity w.r.t. λ yields

$$\frac{dv_{ph}}{d\lambda} = -\frac{c}{n_{ph}^2} \frac{dn_{ph}}{d\lambda} \qquad 3.9$$

and substituting into Eq. 3.6

$$\frac{c}{n_{gr}} = \frac{c}{n_{ph}} + \lambda \frac{c}{n_{np}^2} \frac{dn_{ph}}{d\lambda} \qquad 3.10$$

or

$$\frac{1}{n_{gr}} = \frac{1}{n_{ph}}\left(1+\lambda\frac{1}{n_{nph}}\frac{dn_{ph}}{d\lambda}\right) \qquad 3.11$$

this may be inverted to

$$n_{gr} = n_{ph}\left(1-\lambda\frac{1}{n_{nph}}\frac{dn_{ph}}{d\lambda}\right), \qquad 3.12$$

by using the approximation $(1+\varepsilon)^{-1} = 1-\varepsilon$ for $\varepsilon << 1$

Thus

$$n_{gr} = n_{ph} - \lambda\frac{dn_{ph}}{d\lambda} \qquad 3.13$$

is the modified Rayleigh equation. A slightly different form is obtained by differentiating the relation $c = \lambda f$ w.r.t. λ and f, i.e.

$$\frac{d\lambda}{\lambda} = -\frac{df}{f} \qquad 3.14$$

and by substituting the result into Eq. 3.13

$$n_{gr} = n_{ph} + f\frac{dn_{ph}}{df} \qquad 3.15$$

3.2.2 Ionospheric refraction

The ionosphere is a dispersive medium with respect to the GPS radio signal. Following (Seeber 1993), the phase refractive index may be approximated by the series

$$n_{ph} = 1 + \frac{c_2}{f^2} + \frac{c_3}{f^3} + \frac{c_4}{f^4} + \ldots \quad 3.16$$

The coefficients c_i do not depend on frequency, but on electron density, *Ne* expressed as number of electrons m^{-3}, along the propagation path. Using an approximation by trunctuating the expansion after the quadratic term yields (more than 99.9% accurate ignoring higher terms)

$$n_{ph} = 1 + \frac{c_2}{f^2} \quad 3.17$$

Differentiating

$$dn_{ph} = -2\frac{c_2}{f^3}df \quad 3.18$$

and substituting Eqs 3.17 and 3.18 into Eq. 3.15 yields

$$n_{gr} = 1 + \frac{c_2}{f^2} - f\frac{2c_2}{f^3}, \text{ or} \quad 3.19$$

$$n_{gr} = 1 - \frac{c_2}{f^2} \quad 3.20$$

It can be seen from Eqs. 3.17 and 3.20 that the group and phase refractive indices deviate from unity with opposite sign. With an estimate for c_2 (Seeber, 1993)

$$c_2 = -40.28Ne \ [\text{Hz}^2], \quad 3.21$$

the relation $n_{gr} > n_{ph}$ and thus $v_{gr} < v_{ph}$ follows, because *Ne* is always > 0. As a consequence of the different velocities, a group delay and phase advance occurs. Stated differently**,** GPS code measurements are *delayed* and the carrier phases *advanced*. Therefore, the code pseudo range measurement is *too long* and the carrier phase pseudo range measurent is *too short*, compared with the geometric (true) range between satellite and receiver. The difference is the same in both cases.

3.2.3 Total Electron Content

According to Fermat's principle, the measured range, s, is defined by

$$s = \int n ds \tag{3.22}$$

where the line integral is extended along the signal path. The geometric range, s_0, is the straight line between satellite and receiver and may be obtained by setting $n = 1$:

$$s_0 = \int ds_0 \tag{3.23}$$

The difference Δ^{iono} between measured and geometric range is called the ionospheric refraction and follows from

$$\Delta^{ion} = \int n ds - \int ds_0 \tag{3.24}$$

this may be written for a phase refractive index, n_{ph}, from Eq. 3.17 as

$$\Delta_{ph}^{ion} = \int \left(1 + \frac{c_2}{f^2}\right) ds - \int ds_0 \qquad 3.25$$

and for a group refractive index, n_{gr}, as

$$\Delta_{gr}^{ion} = \int \left(1 - \frac{c_2}{f^2}\right) ds - \int ds_0 \qquad 3.26$$

A simplification is obtained when allowing the integration for the first term in Eqs. 3.25 and 3.26 along the geometrical path. In this case, ds becomes ds_0 and the formulas become

$$\begin{aligned} \Delta_{ph}^{ion} &= +\int \frac{c_2}{f^2} ds_0 \\ \Delta_{gr}^{ion} &= -\int \frac{c_2}{f^2} ds_0 \end{aligned} \qquad 3.27$$

Substitution of Eq. 3.21 into Eq. 3.27 renders

$$\begin{aligned} \Delta_{ph}^{iono} &= -\frac{40.3}{f^2} \int Ne \cdot ds_0 \\ \Delta_{gr}^{iono} &= +\frac{40.3}{f^2} \int Ne \cdot ds_0 \end{aligned} \qquad 3.28$$

Defining the Total Electron Content (TEC) as the line integral

$$TEC = \int Ne \cdot ds_0 \qquad 3.29$$

and substituting into Eq. 3.28 yields

$$\Delta_{gr}^{ion} = +\frac{40.3}{f^2}TEC$$
$$\Delta_{ph}^{ion} = -\frac{40.3}{f^2}TEC \qquad 3.30$$

The TEC introduced by Eq**.** 3.30 is the total electron content along a signal ray path between satellite and receiver. The integral is assumed to include all the electrons in a column with a cross-section of 1 m^2 and extending from receiver to satellite and TEC is measured in TEC units with 1 TECU = 10^{16} electrons.m^{-2}.

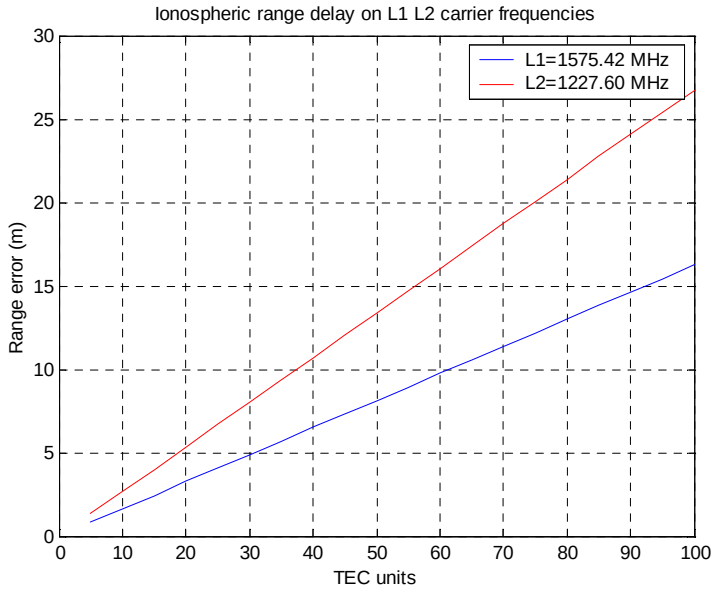

Figure 7. Ionospheric delay dependence on TEC and frequency using Eq. 3.30

It is clear from Eq. 3.30 that TEC may be quantified given an ionospheric range error, Δ^{ion}. The following section discusses the methodology for obtaining the ionospheric range error from the differential of the two carrier frequencies.

3.2.4 Relating GPS observables to Total Electron Content (TEC)

The fundamental observation equations for code and carrier phase measurements are given by (Schaer, 1999)

$$P = \rho + \Delta\rho_{ion} + \Delta\rho_{trop} + c(\Delta t_c{}^S - \Delta t_c{}^R) + c(b^S + b^R) + \varepsilon \qquad 3.31$$

$$L = \rho - \Delta\rho_{ion} + \Delta\rho_{trop} + c(\Delta t_c{}^R - \Delta t_c{}^S) + \lambda B + \mathrm{E} \qquad 3.32$$

where

ρ - geometrical range between receiver and satellite,

$\Delta t_c{}^S$, $\Delta t_c{}^R$ - satellite and receiver clocks errors,

$\Delta\rho_{ion}$, $\Delta\rho_{trop}$ - ionospheric and tropospheric refraction,

b^S, b^R - satellite and receiver hardware delays,

λ - wavelength,

c - speed of light in a vacuum,

B - frequency-specific phase ambiguity bias,

ε , E - residual random errors due to multipath interference, *etc*

Note the ionospheric delay sign difference in the and phase-derived pseudo range expressions. The implication is that the pseudo range is *increased* by the ionospheric effect, while the phase-derived pseudo range is *decreased* by the same amount.

By setting

$$\rho' = \rho + c\left(\Delta t_c^S - \Delta t_c^R\right) + \Delta\rho_{trop} \qquad 3.33$$

the equations for P-code observations and carrier phase observations from dual frequency GPS receivers can be simplified (Schaer 1999)

$$P_1 = \rho' + I + c\left(b_1^S + b_1^R\right)$$
$$P_2 = \rho' + \xi I + c\left(b_2^S + b_2^R\right) \qquad 3.34$$

$$L_1 = \rho' - I + \lambda_1 B_1$$
$$L_2 = \rho' - \xi I + \lambda_2 B_2 \qquad 3.35$$

where

$\xi = f_1^2 / f_2^2 = 1.647$ - factor relating ionospheric refraction to L_1

I - ionospheric refraction related to L_1 [metres],

B_1, B_2 - carrier phase ambiguities on L_1 and L_2

The "geometry-free" linear combinations for P-code and carrier phase observations are defined by

$$P_4 = P_2 - P_1$$
$$L_4 = L_2 - L_1 \qquad 3.36$$

When Eqs 3.36 are applied to Eqs 3.34 and 3.35, we obtain

$$P_4 = +\xi_4 I + c\left(\Delta b^S - \Delta b^R\right)$$
$$L_4 = -\xi_4 I + B_4 \qquad 3.37$$

where

$\xi_4 = 1 - f_1^2 / f_2^2 = 0.647$ - factor relating ionospheric refraction on L_4 to L_1

$B_4 = \lambda_1 B_1 - \lambda_2 B_2$ - ambiguity parameter (unknown wavelength offset)

$\Delta b^S = b_1^S - b_2^S$ - Satellite Differential Code Bias (DCB) in nanoseconds

$\Delta b^R = b_1^R - b_2^R$ - Receiver Differential Code Bias (DCB) in nanoseconds

The geometrical range, clock-offsets and tropospheric delay defined in Eq 3.33, are identical for both frequencies and are effectively eliminated by the linear combinations P_4 and L_4 in Eq. 3.36. Ionospheric modelling is conducted using the "geometry free" P_4 and L_4, as they only contain the ionospheric refraction I, the hardware delays Δb^S, Δb^R (code measurements) and the ambiguity

parameter B_4 (phase measurements). Solving for B_4 and the satellite and receiver DCBs however, is not a trivial exercise and will be discussed in the next section.

The relationship between TEC and P_4 code observations is obtained by equating the ionospheric refraction, I in Eq 3.37, with the group delay, Δ_{gr}^{ion} in Eq 3.30, ignoring the DCBs, pseudorange multipath, ambiguity parameter B_4 and phase measurements for now:

$$\begin{aligned} P_4 &= \xi_4 \Delta_{gr}^{ion} \\ &= \xi_4 . \alpha \frac{TEC}{f_1^2} \\ &= \alpha \frac{TEC}{f_1^2} \cdot \left(1 - \frac{f_1^2}{f_2^2} \right) \\ &= \alpha \cdot TEC \cdot \frac{1}{f_1^2} \cdot \left(\frac{f_2^2 - f_1^2}{f_2^2} \right) \\ &= \alpha \cdot TEC \cdot \left(\frac{1}{f_1^2} - \frac{1}{f_2^2} \right) \end{aligned} \qquad 3.38$$

Subsequently

$$TEC = P_4 \cdot \left[\alpha \left(\frac{1}{f_1^2} - \frac{1}{f_2^2} \right) \right]^{-1} \qquad 3.39$$

3.2.5 Resolving integer ambiguity and differential clock biases

3.2.5.1 Phase levelling

Carrier phase-derived TEC (TEC_L) is 2-3 orders of magnitude less noisy than TEC (TEC_P) (Wilson and Mannucci, 1994), but requires correction for the unknown ambiguity-offset, B_4 and infrequent cycle slips due to signal loss of lock. Solving B_4 is non-trivial and the subject of ongoing research, *eg* on the Fast Ambiguity Resolution Approach (FARA) (Frei and Beutler, 1990) and the Least Squares Ambiguity Decorrelation Algorithm (LAMDA) (De Jonge, 1996). A simpler approach eliminates the ambiguity-offset by means of “phase levelling”, which involves adjusting continuous

arcs of TEC_L to the mean value of the corresponding TEC_P values (Wilson and Mannucci, 1994; Runge *et. al.*, 1995).

$$TEC_L^{ij,corr} = TEC_L^{ij} + \left(\overline{TEC_P}^{i} - \overline{TEC_L}^{i}\right) \qquad 3.40$$

where

TEC_L^{ij} - j^{th} carrier phase-derived TEC value of i^{th} continuous data arc

$\overline{TEC_P}^{i}, \overline{TEC_L}^{i}$ - mean code and phase-derived TEC values of i^{th} continuous data arc

The correction of cycle slips and elimination of the ambiguity-offset by means of phase levelling is illustrated in **Figure 8**.

3.2.5.2 Differential Clock Biases (DCBs)

According to Eq. 3.37, TEC_P contains satellite and receiver DCBs, Δb^S and Δb^R. DCB values may range from 1 to 20ns, the equivalent of 3 to 57 TECU (Eq. 3.39), compared to expected summer mid-day TEC values of about 30 TECU. These DCBs are migrated to TEC_L through the levelling process (Eq. 3.40), and needs to be removed to ensure an unbiased TEC measurement. Satellite DCBs and IGS GPS receiver DCBs are regularely estimated by JPL and CODE and available at [IGS] and [DCB]. Non-IGS receiver DCBs, however, need to be determined independently. Since ionospheric delay and intrumential biases must be estimated simultaneously, the tasks of estimating biases and modelling the ionosphere are intertwined and complementary (Wilson *et. al.*, 1995). Receiver DCBs are typically resolved using least squares or Kalman filtering techniques as part of the ionospheric modelling process (Wilson and Mannucci 1993; Gao *et. al.* 1994; Sardon *et. al.* 1994; Lin and Rizos 1996). In this investigation, DCBs for individual receivers in the South African GPS network are estimated as part of the presented ionospheric modelling process using a weighted least squares method, which is detailed in Chapter 5.

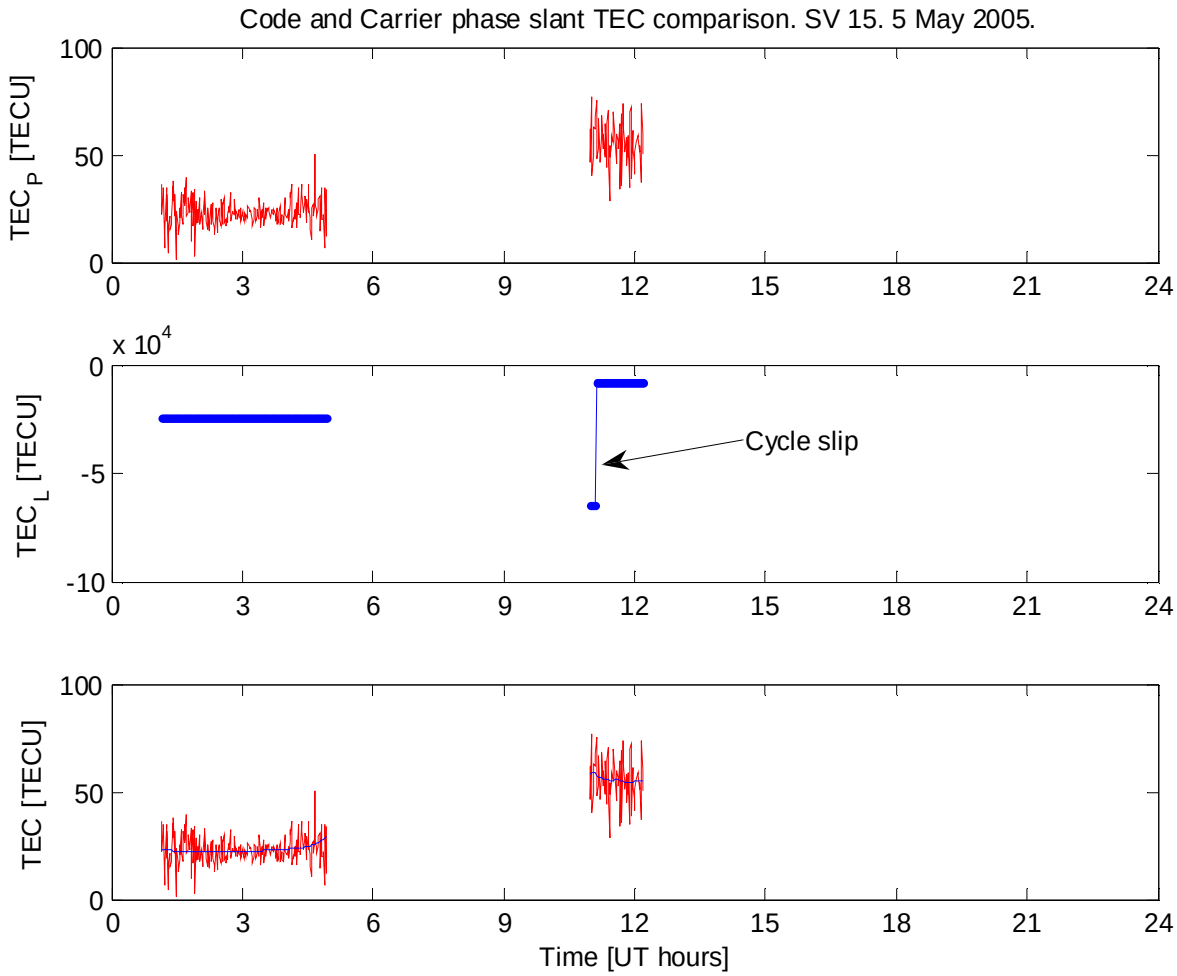

Figure 8. Comparison of code and carrier phase-derived TEC (TEC_P, TEC_L) calculated along the slant signal path of GPS satellite 15 observed from Grahamstown on 5 May 2005. The data gap between 05:00 and 11:00 UT is due to the satellite being below the horizon. The GPS receiver DCB is still present in TEC_P (top plot). The large TEC value in TEC_L (centre plot) is due to the ambiguity-offset (B_4). A cycle slip in the phase measurement is evident by the discontinuity in in the data. In the bottom plot, TEC_L has been phase-levelled to TEC_P using the approach discussed in Par 3.2.5. Note the significantly lower noise levels of the phase-derived TEC to the code-derived TEC in the bottom plot**.**

3.3 GPS time

Several time systems are used in the GPS system. For an exhaustive coverage of the topic, see (Seidelmann, 1992; Montenbruck, 2000).

The time scale to which GPS signals are referenced is referred to as GPS time. GPS time is derived from composite or paper clocks that consists of all operational monitor station and atomic clocks. At the integer second level, GPS time equaled UTC in 1980. However, due to leap seconds that have been inserted into UTC, GPS time is presently ahead of UTC by about 14 seconds. The following relations are defined.

- TAI = GPS + 19.00s (International Atomic Time)
- TAI = TDT -32.184s
- TAI = UTC +1.000*n* s

The actual integer value for *n* is annually reported by the International Earth Rotation Service (IERS). In June 2000, for example, the integer value was *n* = 33 and thus GPS time differed exactly 13 seconds from UTC at the time.

3.3.1 Julian date

The Julian date (JD) is the number of decimal days elapsed since 12:00 UTC on January 1st, 4713 BC.

3.3.2 GPS week

The GPS week is defined as the number of seven-day weeks elapsed since 06 January 1980 (JD 2444244.5). Due to computer word-length restrictions, a maximum GPS week number of 1024 was reached on 22 August 1999 (JD 2451412.5) and necessitated a GPS roll-over; this was introduced

after 22 August 1999. The desired GPS week for a given JD is calculated as the integer part of {(JD-2444244.5)/7}.

3.3.3 GPS second

The number of SI seconds in the GPS week elapsed since 00:00 hours of day 1 of the GPS week to 23:59 UTC of day 7 of the same week. A GPS week contains 604 800 SI seconds.

3.3.4 GPS and UTC1

GPS time is measured in SI seconds linked to continuous International Atomic Time (TAI). UTC1 is linked to Earth rotation (Terrestrial Time) and is update six-monthly or annually with a leap second. GPS time matched UTC1 on 6 January 1980, 00h00, but currently leads UTC1 by 19 seconds.

3.4 GPS geometry

Slant TEC calculations along oblique GPS signal paths (Eqs. 3.37 and 3.39) use measured phase and pseudo range values and are subsequently satellite geometry-independent. Satellite geometry, however, plays a significant role in satellite visibility analysis and TEC spatial mapping, as will be discussed in Chapter 4. To this end, a detailed algorithm for calculating GPS satellite position from long-term predicted mean orbital parameters (GPS Almanac) or four-hourly updated broadcast ephemerides is presented in Appendix A. The principal co-ordinate sytems required for describing satellite geometry are briefly discussed and relevant transformations between co-ordinate systems presented in Appendix A. See (Escobal, 1985; Vallado, 1997) for a detailed discussion of these co-ordinate systems and transformations.

3.4.1 Co-ordinates in orbital plane

Satellite motion around the Earth is confined in an elliptical orbit with the Earth at one focus. The shape, orientation and satellite position within the A satellite's co-ordinates in an elliptical orbital plane are sufficiently described by classical Kepler elements defining the orbit's shape and orientation and the satellite's position. See Appendix A for a definition of the Kepler elements.

3.4.2 Earth-Centred-Earth-Fixed (ECEF)

The ECEF co-ordinate system origin is centred in the Earth's geocentre and co-rotates with the Earth. Its X-axis is directed to Greenwhich, Y-axis points East and Z-axis coincides with the Earth's axis of rotation and points North.

3.4.3 East-North-Up (ENU)

The ENU co-ordinate system is a topocentric horizontal co-ordinate system centred on an observer's geographic location. The XY-plane lies in the local horizontal plane with the X-axis pointing East, the Y-axis pointing North and the Z-axis pointing to the observer's zenith.

3.4.4 Spherical co-ordinates

A satellite's spherical co-ordinates within the local horizontal co-ordinate system are described by its *azimuth* (angle from true north measured eastward), *elevation* (angle above local horizontal plane measured positive towards the zenith) and *range* (euclidian distance between observer and satellite).

3.5 GPS hardware and South African receiver infrastructure

The South African GPS network consists of fourty-seven dual frequency, twelve-channel Ashtech-FX and Trimble receivers operated by Chief Directorate Surveys and Mapping (CDSM) and two Ashtech receivers operated by Hartebeesthoek Radio Astronomy (HartRAO) on behalf of the International GNSS Service (IGS). All receivers use Ashtech choke ring antennas. The two IGS receivers continuously stream 30s sampled data to HartRAO and seventeen CDSM receivers continously stream 1Hz data to CDSM in Cape Town. The remaining CDSM receivers operate from 03:00-18:00 local time and transfer registered data off-line to CDSM. All CDSM GPS data is archived in Cape Town and available in compressed Receiver Independent Exchange (RINEX) format with twenty-four hour latency from [Trignet]. Off-site data copies are stored at the HMO in Hermanus (19.22°E, 34.42°S). The CDSM GPS distribution is illustrated in **Figure 9**.

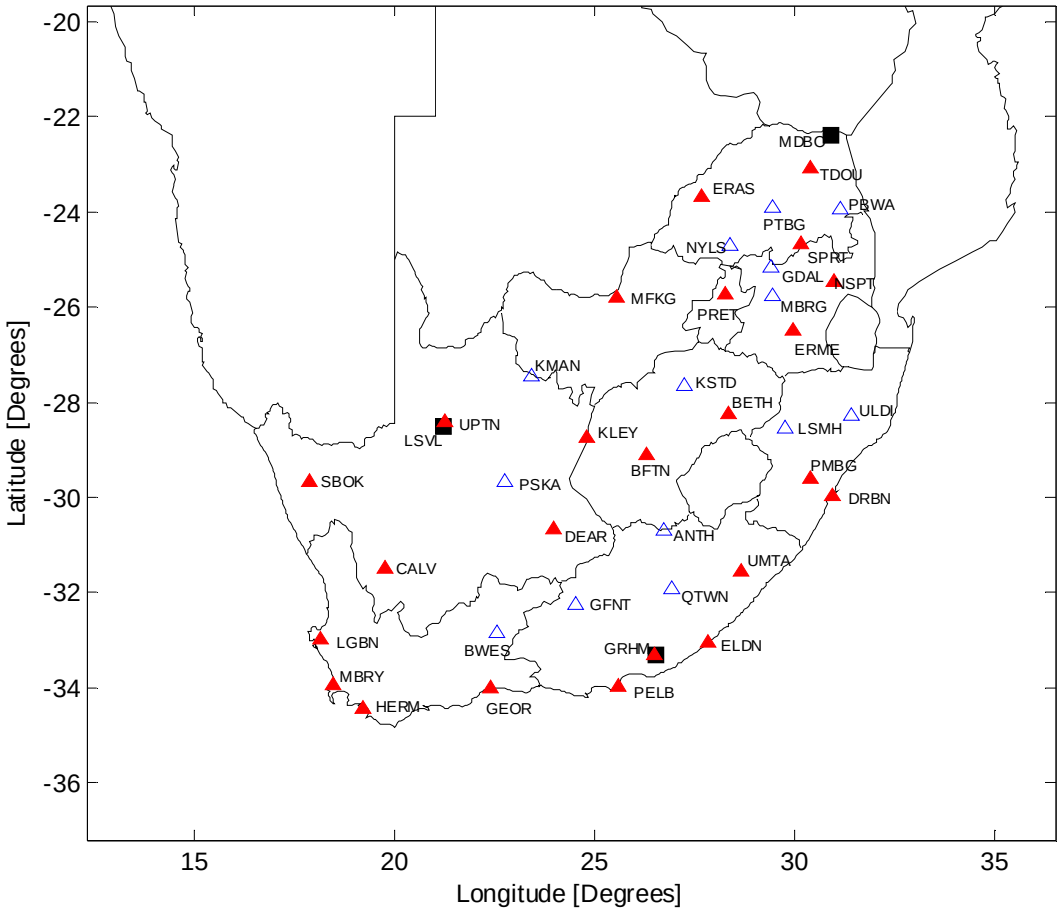

Figure 9. CDSM GPS network. Solid (red) triangles represent real-time receivers and blue (open) triangles represent off-line receivers. The three ionosondes are indicated as black squares. Note the co-located GPS receivers at Grahamstown and Louisvale ionosondes. An explanation of the receiver codes and their geographic positions is given in Appendix B.

Chapter 4

GPS-based ionospheric models

4.1 Introduction

Global and regional Global Positioning System (GPS) Total Electron Content (TEC) models employ various algorithms to resolve the three challenges of

- quantifying ionospheric TEC from dual frequency GPS code and phase measurements,
- resolving satellite and receiver differential clock biases and
- spatially relating the TEC measurements

to render a static or time-dependent two or three dimensional ionospheric product.

This chapter gives an overview of recent models and algorithms developed to resolve these challenges and which are relevant to the research of this thesis. In the context of this thesis, a GPS-derived ionospheric model refers to a data-driven mathematical model developed to estimate ionospheric and instrumental parameters from dual frequency GPS observations, occasionally supplemented by other data sources, depending on model complexity.

The notion of GPS-based ionospheric models evolved from investigative studies into improving the position solution obtained with single-frequency GPS receivers. The Klobuchar model, a set of polynomial coefficients transmitted with GPS navigation signals, was one of the first ionospheric models developed for L_1 observation improvements by reducing the ionospheric bias on single-frequency position solution (Klobuchar *et al.*, 1986). Studies like those of (Royden *et al.*, 1984; Georgiadou and Kleusberg, 1988; Lanyi and Roth, 1988; Coco *et al.*, 1991; Newby, 1992;

Komjathy *et al.*, 1995) focused on developing local ionospheric models for removing, or greatly reducing, the ionosphere-induced scale bias of GPS solutions obtained from single-frequency receivers operating close to one or more dual-frequency receivers. In his PhD thesis focusing on modelling and monitoring the ionosphere, Wild developed several local ionospheric models for a number of International GNSS Service (IGS) stations and concluded that valuable information concerning the ionosphere could be derived from the IGS network (Wild, 1994). Other early works exploiting ionospheric error on GPS signals for ionospheric mapping was described by (Lanyi and Roth, 1988; Mannucci *et al.*, 1993; 1994; Beutler, 1995).

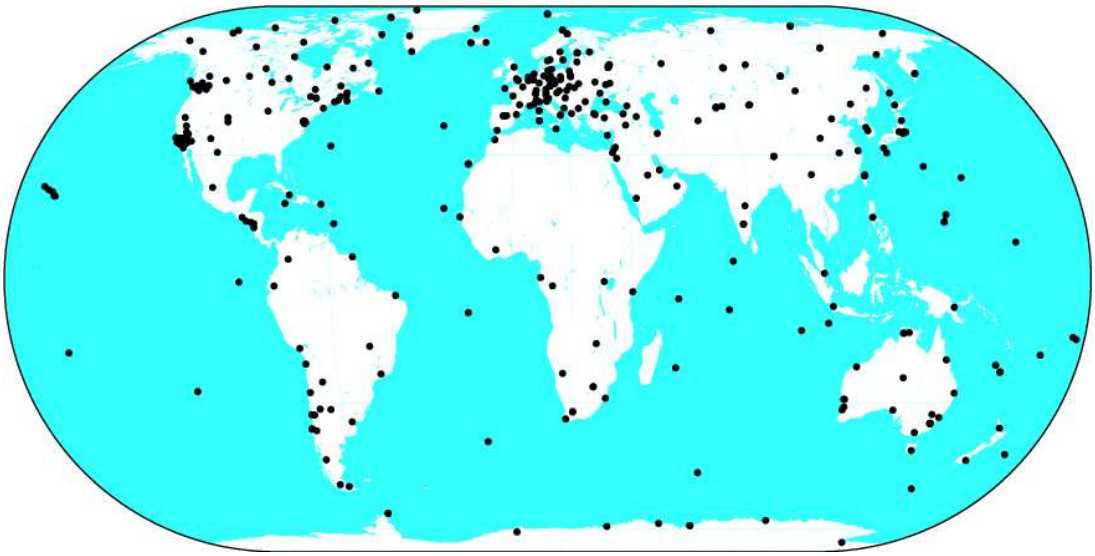

Figure 10. Present IGS network of dual frequency receivers. (http://igscb.jpl.nasa.gov)

4.2 Global Models

The IGS network for geodynamic research was formalised in 1992 (**Figure 10**) and has become a valuable resource for global ionospheric research (Zumberge *et al.*, 1994). Frequently employed techniques in global and regional TEC models include Kalman filtering, spherical harmonic analysis, least squares, computerised ionospheric tomography (CIT) and Kriging, a 2D interpolation technique. All the 2D mapping techniques employ some form of ionospheric shell model with a

fixed or variable shell height and a slant to vertical TEC mapping function to geographically tie down the oblique TEC measurement. Several individuals and groups have contributed to developing global ionospheric models using signals from the IGS network and the models most relevant to this thesis' research are briefly discussed. A brief explanation of the Kalman filter is given in Appendix C.

4.2.1 Klobuchar Model

The Klobuchar ionospheric delay model is a global, polynomial-based model developed for correcting the single-frequency receivers' L_1 signals for ionospheric delay. Though not as accurate as recent models, Center for Orbit Determination Europe (CODE) supplies a global TEC product derived from Klobuchar coefficients. The Klobuchar model approximates the ionospheric delay, T_g, by a polynomial (Klobuchar, 1986; Grewel *et al.*, 2001; Hofmann-Wellenhof *et al.*, 2001).

$$T_g = dc + A\left[1 - \frac{x^2}{2} + \frac{x^4}{4}\right], \quad |x| \le \frac{\pi}{2}$$

where

$$x = \frac{2\pi\left(t - T_p\right)}{P} \text{ (radians)}$$

with

dc	constant offset
T_p	constant phase
A	amplitude (calculated from broadcast polynomial coefficients)
P	period (calculated from broadcast polynomial coefficients)
t	local time at ionospheric pierce point (IPP).

A mean ionospheric shell height of 350km is assumed and the constant offset, dc and phasing, T_p, are respectively held constant at 5 ns and 14:00 (50400 s) local time. The amplitude (A) and period (P) are modelled as third-order polynomials constructed from broadcast coefficients, α_n, β_n and

from the IPP's geomagnetic latitude, ϕ_{ipp}^{m}, which corresponds to a simple dipolar model's geomagnetic latitude

$$A = \sum_{n=0}^{3} \alpha_n \left(\phi_{ipp}^{m}\right)^n \ , \ P = \sum_{n=0}^{3} \beta_n \left(\phi_{ipp}^{m}\right)^n \text{ [seconds]}$$

The IPP geomagnetic latitude, ϕ_{ipp}^{m}, is calculated from IPP longitude and latitude (λ_{ipp}, ϕ_{ipp}) and geographic co-ordinates of the magnetic pole (λ_P, ϕ_P) = (291.0°E, 78.3°N)

$$\phi_m = \phi_{ipp} + 11.6^{\circ}\left(\lambda_{ipp} - 291^{\circ}\right)$$

$$\cos\phi_{ipp}^{m} = \sin\phi_{ipp}\sin\phi_P + \cos\phi_{ipp}\cos\phi_P\cos\left(\lambda_{ipp} - \lambda_P\right)$$

The Klobuchar model approximates IPP longitude and latitude values from satellite azimuth (*az*), elevation (*el*) and approximated subtended Earth angle (γ), the angle between the GPS receiver, Earth centre and satellite:

$$\phi_{ipp} = \phi_{Rx} + \gamma\cos(az)$$

$$\lambda_{ipp} = \lambda_{Rx} + \gamma\frac{\cos(az)}{\cos(\phi_{ipp})}$$

$$\gamma = \frac{445}{el + 2\times10^{-4}}$$

The ionospheric time delay, in seconds, is finally calculated as

$$T_g = \begin{cases} k\left[dc + A\left(1 - \dfrac{x^2}{2} + \dfrac{x^4}{4}\right)\right], & |x| \le \dfrac{\pi}{2} \\ k \cdot dc, & |x| \ge \dfrac{\pi}{2} \end{cases}$$

where k is an elevation scaling factor:

$$k = 1 + 2\left[\frac{96^\circ - el}{90^\circ}\right]^3$$

4.2.2 Mannucci and Wilson (Jet Propulsions Laboratory)

The global model developed by Mannucci and Wilson was motivated by ionospheric calibration requirements for deep space tracking and navigation purposes (Mannucci *et al.*, 1993). The model uses a Kalman filter technique to generate time-sequential global TEC maps that are individually constructed from a set of locally supported vertical TEC-functions defined on a tessellation of the sphere into 1280 triangles (Wilson *et al.*, 1995; Mannucci *et al.*, 1998). The individual maps are constructed by employing a (350 km) spherical thin-shell elevation mapping function to convert all receiver-to-satellite TEC measurements to equivalent vertical TEC at unique IPPs (Lanyi and Roth, 1988; Mannucci *et. al,.* 1993; 1994) and interpolating vertical TEC estimates between pierce points using weighted base functions defined on the triangles. Interpolation accuracy is ensured by defining each triangle vertex in an orthogonal co-ordinate system, defined by a near Sun-fixed longitude (local time) and geomagnetic latitude system, to provide for diurnal and geomagnetic TEC variation. Model details can be found in (Mannucci *et al.*, 1993; 1998).

4.2.3 Komjathy (University of New Brunswick, Canada)

The UNB algorithm uses a spatial linear approximation of the TEC above each GPS receiver with stochastic parameters estimated in a Kalman filter optimisation to describe the local time and geomagnetic latitude dependence of TEC (Komjathy, 1997). A thin-shell mapping function, based on an IRI-derived variable shell height, is introduced to map slant to vertical TEC values and accounts for the temporal and spatial variability of the assumed ionospheric shell height. The UNB model is briefly discussed.

For each receiver $j = 1, 2 \ldots N$ in a network, the following observation equation is constructed:

$$I_{r_j}^{s_i}(t_k) = M\left(e_{r_j}^{s_i}\right) \cdot \left[a_{0,r_j}(t_k) + a_{1,r_j}(t_k)\delta\lambda_{r_j}^{s_i} + a_{2,r_j}(t_k)\delta\phi_{r_j}^{s_i}\right] + b_{r_j} + b^{s_i} \qquad 4.1$$

where

$I_{r_j}^{s_i}(t_k)$	L_1-L_2 phase-levelled TEC measured by receiver r_j observing satellite s_i at time t_k
$M\left(e_{r_j}^{s_i}\right)$	thin-shell elevation angle mapping function mapping the slant TEC measurement to a vertical with $e_{r_j}^{s_i}$ being the elevation angle of satellite s_i observed by receiver r_j
$a_{0,r_j}, a_{1,r_j}, a_{2,r_j}$	parameters for spatial linear approximation of TEC to be estimated per station r_j
$\delta\lambda = \lambda_{r_j}^{s_i} - \lambda_0$	longitude difference between the IPP and that of the mean Sun.
$\delta\phi = \phi_{r_j}^{s_i} - \phi_{r_j}$	geomagnetic latitude difference between the IPP and that of receiver.
b_{r_j}, b^{s_i}	receiver and satellite differential delays.

After estimating the three stochastic parameters for each GPS receiver, hourly TEC maps are computed using a (1°x1°) grid for regional TEC maps and (5°x5°) grid for global TEC maps. TEC is evaluated at the i^{th} grid point using a weighted distance function and TEC estimations at the nearest four GPS receivers

$$TEC_i = \frac{\sum_{j=1}^{4} \frac{1}{d_j^2} TEC_j}{\sum_{j=1}^{4} \frac{1}{d_j^2}} \qquad 4.2$$

4.2.4 Schaer (Center for Orbit Determination Europe)

Unlike the aforementioned JPL and UNB models, Schaer's model does not depend on a number of local models. Schaer improved on Wild's local ionospheric models (Wild, 1994) by developing a single global ionospheric model based on a spherical harmonic expansion, which integrated observations from multiple receivers into a single model for regional or global application (Schaer *et al.*, 1995; Schaer 1999).

$$TEC(\phi,\lambda) = \sum_{n=0}^{N}\sum_{m=0}^{n} \bar{P}_{nm}[\sin\phi]\left(\bar{C}_{nm}\cos(m\lambda) + \bar{S}_{nm}\sin(m\lambda)\right) \qquad 4.3$$

where

ϕ	IPP geographic (or geomagnetic) latitude
$\lambda = \lambda_{ipp} - \lambda_{sun}$	IPP sun-fixed longitude
$\lambda_{ipp}, \lambda_{sun}$	geographic longitude of IPP and Sun respectively
N	maximum degree of the spherical harmonic expansion
$\bar{P}_{nm}$	normalised associated Legendre function of degree *n* and order *m*
$\bar{C}_{nm}, \bar{S}_{nm}$	unknown spherical harmonic coefficients and global ionospheric map parameters respectively.

Schaer's model employs a (450km) thin-shell elevation mapping function to convert slant to vertical TEC values at the ionospheric pierce points. The SH coefficients, $\bar{C}_{nm}, \bar{S}_{nm}$ are estimated in a weighted least squares solution and are used in Eq. 4.3 to interpolate TEC on a global (or regional) scale. The model developed for this thesis is based on the work of Schaer and will be presented in Chapter 5.

Schaer's model has been implemented by the Center for Orbit Determination Europe (CODE) in an operational system computing two-hourly Global Ionospheric Maps (GIMs) from the IGS network (Schaer, 1996). GIMs are generated on a daily basis using data from about 150 IGS and other institutions' GPS receivers. The VTEC is modelled in a solar-geomagnetic reference frame using a spherical harmonics expansion up to degree and order 15. The spatial resolution is 5° and 2.5° in

longitude and latitude respectively. Instrumental biases for all GPS satellites and ground stations are estimated as constant values for each day. The parameters required to represent the global VTEC distribution are distributed in the IONEX format (Schaer *et al.*, 1998). Four analysis centres presently provide IGS VTEC maps, i.e. CODE, JPL, ESA and UPC. These GIMS are properly combined in terms of IGS VTEC maps. CODE also calculates Global Ionospheric Maps derived from Klobuchar coefficients.

4.3 Regional Models

Though the IGS network inspired the development of global ionospheric models, regional models are valuable tools for applications such as studying the effects of geomagnetic storms on the ionosphere (Rideout and Coster, 2006). The higher time and spatial resolution imaging achievable with regional models permits observation of localised ionospheric structure and dynamics not observable on a global scale. One such an example is the observation of ionospheric plumes using observations from dense regional GPS networks (Coster *et al.*, 2001). Two operational regional models are the Japanese GEONET TEC system and the United States TEC model.

4.3.1 GPS Earth Observation Network GEONET (Japan)

The Japanese GPS Earth Observation Network (GEONET) is managed by the Japanese Geographical Survey Institute and consists of more than 1000 GPS receivers spaced about 25km apart (Miyazaki *et al.*, 1997). TEC measurements are obtained for all satellite-receiver paths at 30 s intervals and a grid-based least squares fitting tecnique, developed by (Otsuka *et al.*, 2002), is used to remove instrumental biases and generate TEC maps at 30 s time and 0.15°x0.15° longitude/latitude spatial resolution. Other models developed for GEONET include Ma's improvement on Otsuka's model (Ma and Maruyama, 2003) and Gao's 2D and 3D models (Gao and Liu, 2002). GEONET TEC products are distributed by [GEONET].

4.3.2 NOAA real-time US Total Electron Content (US_TEC)

US_TEC is a data assimilation model developed at the National Oceanic and Atmospheric Administration (NOAA) Space Environment Center (SEC). The current ionospheric products are

generated using real-time data from about 60 GPS receivers in the Continuously Operating Reference Station (CORS) network and the products are calculated with a sample interval of 15 minutes (Fuller-Rowell *et al.*, 2006). The US-TEC model uses an emprical model with a Kalman filter based on the MAGIC software developed by (Spencer *et al.*, 2004).

4.4 Ionospheric shell model

To facilitate the geographic mapping of TEC measurements, several models assume a spherical ionosphere located at some shell height (*H*) (**Figure 11**). A simple (cosec) elevation mapping function (Eq 4.4) is applied to convert the slant TEC measurement to vertical TEC values. The vertical TEC measurement is then assigned to the geographic location at the Ionospheric Pierce Point (IPP). Different models use different shell heights which approximately correspond to the F2 peak density height (*hmF2*). CODE's GIM assumes an infinitely thin-shell, fixed at 450 km above the Earth, (Schaer, 1999), the UNB model assumes an IRI-derived, time-dependent variable shell height (Komathy, 1997) and the JPL VTEC values are calculated using three slab/shell height assumptions (Mannucci *et al.*, 1993). Several studies have investigated the accuracy of different shell heights (Komjathy and Langley, 1996).

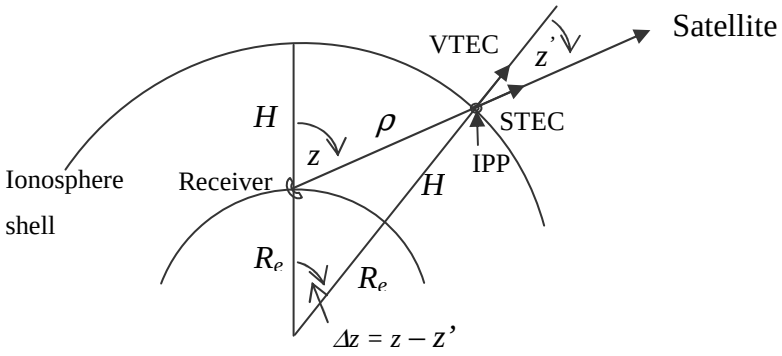

Figure 11. Geometry of slant to vertical TEC (VTEC) mapping function. Assumed ionospheric shell height, H, corresponds to typical F2 peak density height (*hmF2* ~ 300-450 km). VTEC is mapped at the geographic location of the IPP, distinct from the receiver location.

The elevation mapping function for converting slant to vertical TEC measurements is given by

$$STEC = \frac{VTEC}{\cos z'}, \quad \sin z' = \frac{R_e}{R_e + H} \sin z \qquad 4.4$$

with

z	satellite zenith angle,
R_e	Earth equatorial radius (6378.134 km),
H	assumed ionospheric shell height.

4.5 Data assimilation models

Current research in ionospheric characterisation using GPS signals focuses on *data assimilation* and near real-time ionospheric mapping (Liu *et al.*, 2005). Data assimilation techniques evolved from simple two-dimensional, time-varying TEC mapping methodologies to more complex techniques capable of reconstructing four-dimensional (longitude, latitude, height and time) electron density distributions from GPS signals and other data sources. Examples of these are the Multi Instrument Data Assimilation System (MIDAS) (Mitchell and Spencer, 2002; 2003), MAGIC (Spencer *et al.*, 2004) and the Global Assimilative Ionospheric Model (GAIM) (Wang *et al.*, 2004).

4.5.1 Multi Instrument Data Assimilation System (MIDAS) and MAGIC.

The Multi Instrument Data Assimilation System, developed by the University of Bath (Mitchell and Spencer, 2002; 2003), is based on Computerised Ionospheric Tomography (CIT) principles utilising a set of orthogonal basis functions and slant TEC derived from GPS differential phase. MIDAS inverts the four-dimensional ionisation distribution in the ionosphere as electron density values contained in volume elements (voxels). In MIDAS, GPS TEC observations may be supplemented with ionosonde profiles, LEO occultation observations, Typhoon Operational Experiment (TOPEX/Poseidon or T/P) TEC or incoherent scatter data. MIDAS is scale invariant and can be

applied in a regional or a global context. The inversion process, however, requires an integration period of up to one hour, placing a restriction on observing short-term varying phenomena.

MAGIC, developed by (Spencer *et al.*, 2004), evolved from MIDAS. The major difference between the two is MAGIC's utilisation of a Kalman filter, which provides a means of optimally updating a solution to a linear least squares problem by combining time-dependent observations and a prior model estimate of the solution.

4.5.2 Global Assimilative Ionospheric Model (GAIM)

Jet Propulsions Laboratory (JPL) and University Southern California (USC) jointly developed the Global Assimilative Ionospheric Model (GAIM). GAIM is a three-dimensional, time-dependent model constructed by combining first principle ionospheric, plasmaspheric and neutral wind models with a Kalman filter optimisation technique, which allows the assimilation of various types of ionospheric measurements (Liu *et al.*, 2005). Ionospheric data used in GAIM includes ground and space-based GPS measurements, ionosonde profiles, satellite UV limb scans, UV airglow radiances, *in situ* electron and neutral densities, plasma drifts, neutral winds, neutral densities, *etc* (Wang *et al.*, 2004). GAIM's Kalman filter optimization provides a predictive capability, making it comparable to a numerical weather prediction (NWP) model. The GAIM model is routinely validated against T/P and Jason TEC measurements. More details on GAIM are available at (Hajj *et al.*, 2004; Wang *et al.*, 2004; [GAIM]).

Another GAIM is the Utah State University's Global Assimilative Ionsopheric Model, USU-GAIM, developed by (Schunk *et al*., 2002; Schunk *et al*., 2005). This model uses a Gauss-Markov Kalman Filter (GMKF) model, which uses a physics-based model of the ionosphere and a Kalman filter as a basis for assimilating a diverse set of real-time (or near real-time) measurements (Scherliess *et al*., 2002; Scherliess *et al*., 2004; Scherliess *et al*., 2006). The physics-based model is the (global) Ionosphere Forecast Model (IFM), which covers the E-region, F-region, and topside from 90 to 1400 km. It takes account of five ion species (NO+, O2+, N2+, O+ and H+). The main output of the model is a 3-dimensional electron density distribution at user specified times. In addition, auxiliary parameters are also provided, including NmE, hmE, NmF2, hmF2, slant and vertical TEC.

The Gauss-Markov Kalman Model assimilates bottom-side Ne profiles from a variable number of ionosondes, slant TEC from a variable number of ground GPS/TEC stations, in situ Ne from four DMSP satellites, and line-of-sight UV emissions measured by satellites.

4.6 Other ionospheric TEC resources

4.6.1 Very Long Baseline Interferometry (VLBI)

Very Long Baseline Interferometry is a space geodesy technique which measures and utilises the time differences in the arrival of microwave signals from extragalactic radio sources (quasars, pulsars *etc*) received at two or more radio observatories, to compute (sub-millimetre) accurate positions of the receiving antennae. The geodetic applications of VLBI include Earth rotation and orientation parameters determination, co-ordinate reference frame definition and refinement and crustal movement monitoring. Similar to GPS navigation signals, extragalactic radio signals are attenuated by the Earth's ionosphere and are corrected by removing the ionospheric delay using two receiving frequencies, *eg* 2.28 and 8.4 GHz, depending on the application. Ionospheric TEC may be quantified from VLBI observations by using techniques similar to those used in GPS signals. VLBI-derived TEC has been used in several studies to evaluate or compliment GPS TEC measurements (Sekido *et al.*, 2003; Hobiger *et al.*, 2006).

4.6.2 TOPEX/Poseidon (T/P) and Jason-1

The Typhoon Operational Experiment (TOPEX/Poseidon) is a co-operative satellite project between the USA (NASA) and France (CNES) to observe the Earth's oceans using radar altimetry (Fu *et al.*, 1994; Mannucci *et al.*, 1994). TOPEX was launched on 10 August 1992 and orbits Earth at 1300 km with orbital period of 112 minutes and repeat ground track every 10 days (one cycle). A successor satellite, Jason-1, was launched on 7 December 2001 to compliment T/P. Both satellites are still operational with the Jason-1 orbit lagging T/P by 70 seconds. The main payload on T/P and Jason-1 is a dual-frequency radar altimeter operating simultaneously at 13.6 GHz (Ku band) and 5.3 GHz (C band). Measurements made at these two frequencies are combined to obtain altimeter

ocean-height (corrected for ionosphere), neutral wind speed and wave height (Benada, 1997). Vertical ionospheric range delay values are calculated at 1 s, permitting 1 Hz calculation of ionospheric TEC using the relation (Benada, 1997)

$$TEC = -\frac{Iono\_corr}{f^2} \cdot 403 \qquad 4.5$$

with

Iono_corr the ionospheric delay in mm

f the carrier frequency in GHz.

As T/P and Jason-1 orbit above the ionosphere, they are well suited for a variety of ionospheric studies and are frequently used for comparing or complimenting other ionospheric measurements or techniques (Mannucci *et al.*, 1994; Ho *et al.*, 1997; Ping *et al.*, 2004; Reinisch *et al.*, 2004). T/P and Jason-1 measurements, however, are restricted to open oceans and large inland lakes and biases in the measurements have been pointed out (Zhao *et al.*, 2004). T/P and Jason-1's radar altimeter ionospheric delay measurements, as well as DORIS measurements and Bent model ionospheric parameters, are archived and distributed by NASA's Physical Oceanography Distributed Active Archive Center [PO.DAAC].

Chapter 5

South African Regional TEC Model

5.1 Introduction

This chapter presents the original research conducted in this study to establish a working methodology for estimating ionospheric TEC from a regional South African GPS receiver network. In his research, Schaer (Schaer *et al.*, 1995; Schaer 1999) pointed out the applicability and relevance of his global model as a regional model. After successfully implementing this model in software and evaluating it for South African latitudes, the question arose as to whether this model, developed for a global application, might be adapted to take advantage of densely distributed observations in a relatively small geographic region. In this study, an adaptation to Schaer's global ionospheric model is presented and evaluated for application in a regional context. The new Adjusted Spherical Harmonic Analyses (ASHA) model introduced in this study is based on the Conventional Spherical Harmonic Analysis (CSHA) methodology introduced by (Schaer, 1999) and implemented by the Center for Orbit Determination in Europe [CODE]. This chapter discusses the similarities and differences of the two models. It also presents the mathematical description and tests the software implementation of both algorithms as well as evaluate both algorithms' ability to estimate the TEC for a single GPS receiver and also to construct 2D TEC maps from multiple GPS receiver observations.

5.2 Model development

5.2.1 Spherical Harmonic Model

Conventional spherical harmonic analysis (CSHA) models TEC as a spherical harmonic expansion:

$$TEC(\lambda,\phi) = \sum_{n=0}^{N}\sum_{m=0}^{n} \overline{P}_{nm}[\cos(\phi)]\{a_{nm}\sin(m\lambda) + b_{nm}\cos(m\lambda)\}$$

λ = IPP Sun-fixed longitude $\in \left[0^{\circ}, 360^{\circ}\right]$,

ϕ = IPP co-latitude $\in \left[0^{\circ}, 180^{\circ}\right]$, 5.1

$\overline{P}_{nm}$ = Normalized associated Legendre functions of degree n and order m,

a_{nm}, b_{nm} = Desired SHM coefficients and

n, m = Degree and order of SHM expansion

A spherical harmonic expansion is a two-dimensional Fourier series defined on a sphere and comprises the product of latitude-dependent associated Legendre functions and the sum of longitude-dependent sine and cosine terms (the Fourier series). The spherical harmonic expansion tessellates the sphere into a number of rectangular tiles with the boundaries between adjacent tiles representing the roots of the orthonormal Fourier functions. The number of tiles is determined by the *degree* and *order* of the expansion, with higher degree and order implying a larger number of tiles. Within the context of this study, the *degree* corresponds to the number of wavelengths spanning the latitudinal space and the *order*, the number of wavelengths spanning longitude. An example of a 15x10 degree/order SHM is given in **Figure 12**.

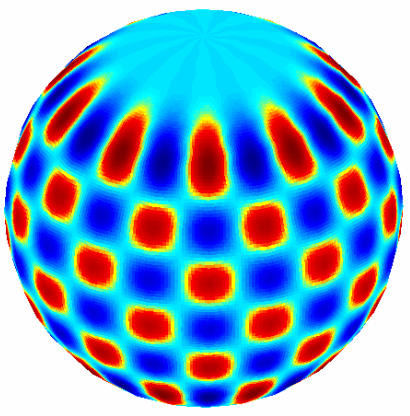

Figure 12. Example of spherical harmonic orthogonal basis functions of degree 15 and order 10.

The associated Legendre function, $P_{nm}[\cos\phi]$, in Eq. 5.1 is given by

$$P_{nm}[\cos\phi] = (-1)^m (\sin\phi)^m \frac{d^m}{d(\cos\phi)^m}\left(P_n[\cos\phi]\right)$$

where $P_n[\cos\phi]$ represents the n^{th} degree orthogonal Legendre function

$$P_n[\cos\phi] = \frac{1}{2^n n!}\frac{d^n}{d(\cos\phi)^n}\left[\left(\cos^2\phi - 1\right)^n\right]$$

The associated Legendre functions can be efficiently computed by recursion (Vallado, 1997)

$$P_{n,0}[\cos\phi] = \frac{(2n-1)\cdot\cos\phi\cdot P_{n-1,0}[\cos\phi] - (n-1)\cdot P_{n-2,0}[\cos\phi]}{n}, n \geq 2$$

$$P_{n,m}[\cos\phi] = P_{n-2,m}[\cos\phi] + (2n-1)\cdot\cos\phi\cdot P_{n-1,m-1}[\cos\phi], m \neq 0, m < n$$

$$P_{n,n}[\cos\phi] = (2n-1)\cos\phi P_{n-1,n-1}[\cos\phi], m \neq 0$$

with starting values

$$P_{0,0}[\cos\phi] = 1, \quad P_{1,0}[\cos\phi] = \cos\phi, \quad P_{1,1}[\cos\phi] = -\sin\phi.$$

Similarly, the trigonometric functions can be calculated recursively

$$\sin(m\lambda) = 2\cos(\lambda)\sin\{(m-1)\lambda\} - \sin\{(m-2)\lambda\}$$
$$\cos(m\lambda) = 2\cos(\lambda)\cos\{(m-1)\lambda\} - \cos\{(m-2)\lambda\}.$$

Normalization is achieved by letting (Vallado, 1997)

$$\overline{P}_{nm}[\alpha] = \frac{P_{nm}[\alpha]}{\prod_{nm}}$$

Where the normalization operator, $\prod_{nm}$, is given by

$$\prod_{nm} = \sqrt{\frac{(n+m)!}{(n-m)!(2n+1)k}}$$

k = 1 for m = 0;

k = 2 for m >1,

5.2.2 Co-ordinate System

5.2.2.1 Sun-fixed longitude

The adjusted spherical harmonic (ASHA) methodology introduced in this study utilises the IPPs Sun-fixed longitude, λ_s, i.e., the longitude expressed relative to the Sun's mean geographic longitude. Sun-fixed longitude conveniently encapsulates the IPPs time and longitudinal variation in a single angular observation spanning 360º over a twenty-four hour revolution and is calculated from the geographical longitude, λ, by

$$\lambda_s = \left(180^\circ - \Omega_e \cdot t\right) - \lambda,$$

where Ω_e represents the Earth rotation rate and t the time elapsed since midnight UT. The conventional spherical harmonic model used in CODE's global ionospheric TEC mapping also employs Sun-fixed longitude.

5.2.2.2 Legendre functions and co-latitude

An *n*-degree, *zero*-order spherical harmonic expansion is a *zonal harmonic*, which is an associated Legendre function P_{nm}, reduced to the Legendre function $P_n = P_{n0}$. Zonal harmonics are latitudinal-dependent functions defined along a longitude meridian and, in the context of global modelling, have a terrestrial wavelength, λ_t, of 360°/*n* degrees ($2\pi R/n$ km with R the Earth radius). For example, a 15-degree Legendre function has a terrestrial wavelength of 24° (~2672 km). The 15-degree Legendre function's latitudinal coverage of a sphere and a hemisphere is illustrated in **Figure 13**. In a 15-degree and order conventional spherical harmonic analysis applied to observations from a global GPS receiver network, the large spatial coverage of observations justifies a 24° wavelength for modelling and interpolating TEC at the present 2.5° latitude resolution. The geometry of IPPs from the South African regional GPS network, however, constitutes a spherical cap with spherical angle of about 20° (~2226 km), which constitutes a regional, rather than a global observation data set. In Sun-fixed longitude, co-latitude co-ordinates, this spherical cap translates to a spherical segment confining the IPPs in a relatively narrow, regional latitude band on the globe (**Figure 14**). In a regional context, less than one wavelength of a 15-degree Legendre function spans the South African 20° latitudinal spherical angle (**Figure 13**, top). The relatively dense IPP distribution observed from the South African regional GPS receiver network, however, permits a higher spatial resolution TEC interpolation than it does on a global scale. To achieve an equivalent 7.5 terrestrial wavelengths on a 20° spherical angle would, however, require a Legendre function of degree $\left(\frac{20}{15}\times 360 = 480\right)$. This will not be computationally efficient because of the substantial increase in mathematical operations. An equivalent number of terrestrial wavelengths, however, can be fitted into a 20° spherical angle by introducing an appropriate scaling function.

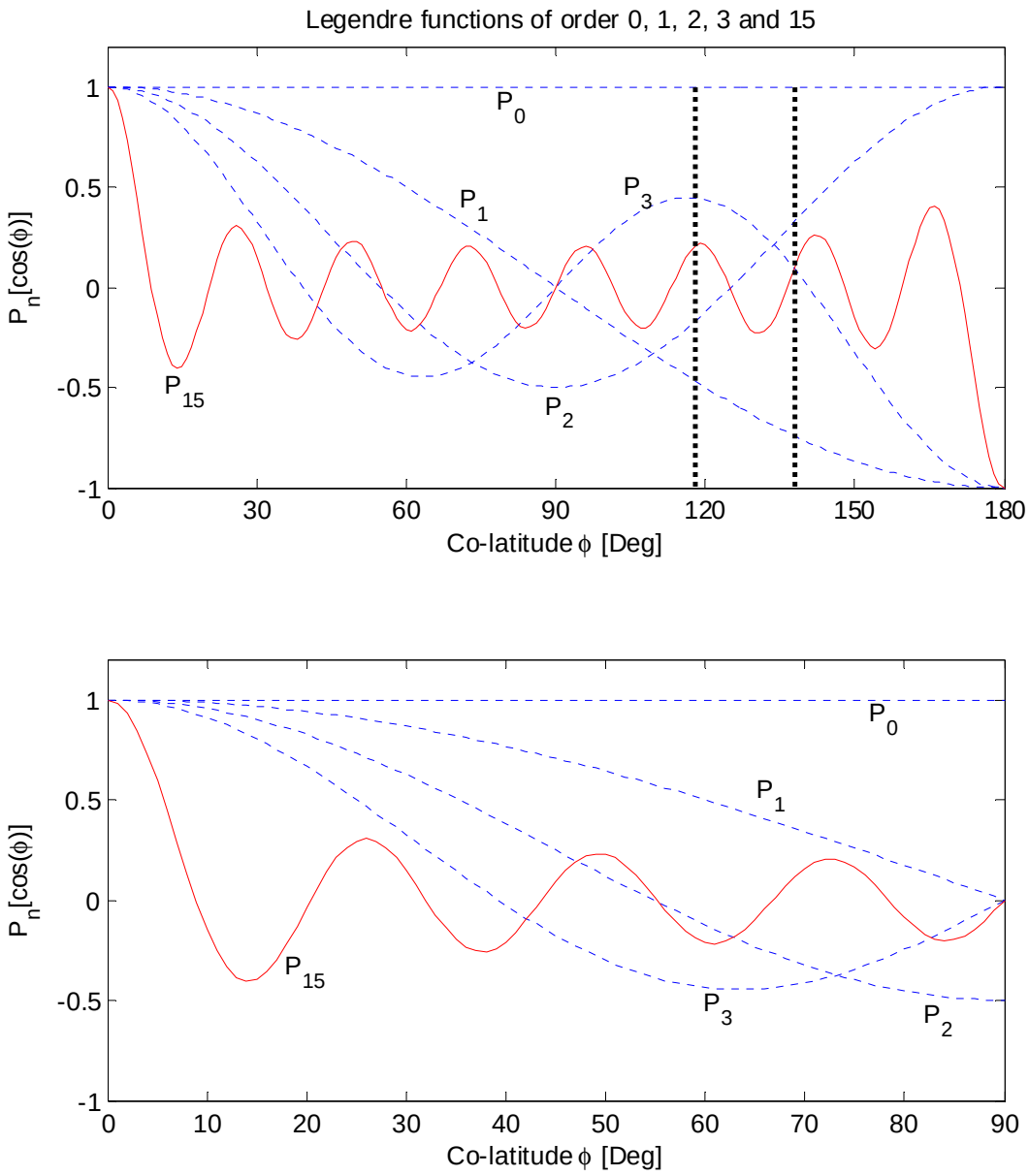

Figure 13. Legendre functions defined on the sphere (top) and the hemisphere (below). A typical South African regional 20° latitudinal spherical angle is indicated by the IPP co-latitude region [118°, 138°] (top). Notice the < 1 terrestrial wavelength spanning the 20° latitudinal spherical angle (top).

A new approach introduced in this study involves scaling the regional IPP co-latitude from a spherical angle to a hemisphere prior to applying the conventional spherical harmonic model. The scaling function is similar to that introduced by De Santis, 1991, and involves translating and scaling the IPP co-latitude by employing the minimum co-latitude of the IPPs, ϕ_0, and the spherical angle, θ, of the observations:

$$\phi' = \frac{90^\circ}{\theta} \cdot (\phi - \phi_0) \qquad 5.2$$

The IPP co-latitude, ϕ, in Eq. 5.1 is subsequently replaced by the scaled co-latitude, ϕ', defined on a hemisphere [0°, 90º] and used in the conventional spherical harmonic model and henceforth referred to as the *adjusted spherical harmonic* (ASHA) model. This transformation is valid as the Legendre polynomials form a set of orthogonal functions on [0°, 180º], but may be used as two sets of orthogonal functions on [0°, 90º] to fit any general functions defined in this interval (De Santis, 1992).

The number of terrestrial wavelengths for an *n*-degree Legendre function fitting a hemisphere is *n*/4. The equivalent, scaled terrestrial wavelength, λ_t', for an *n*-degree Legendre function, scaled from a spherical angle θ to a hemisphere, is

$$\lambda_t' = \frac{\theta}{\frac{\pi}{2} n} \times 2\pi = \frac{4\theta}{n} \qquad 5.3$$

From Eq. 5.3 the scaled terrestrial wavelength for a 15-degree Legendre function on a 20° spherical angle is calculated as 5.33° (~593 km). Let P_n and P_n' respectively denote the Legendre functions constructed from the *spherical* co-latitude range $\phi \in$ [0°, 180º] and from the adjusted *hemispherical* latitude range $\phi' \in$ [0°, 90º]. The difference between P_n and P_n' on a 20° spherical angle and the equivalent fit of P_n and P_n' on the interval $\phi \in$ [0°, 180º], are illustrated in **Figure 15.**

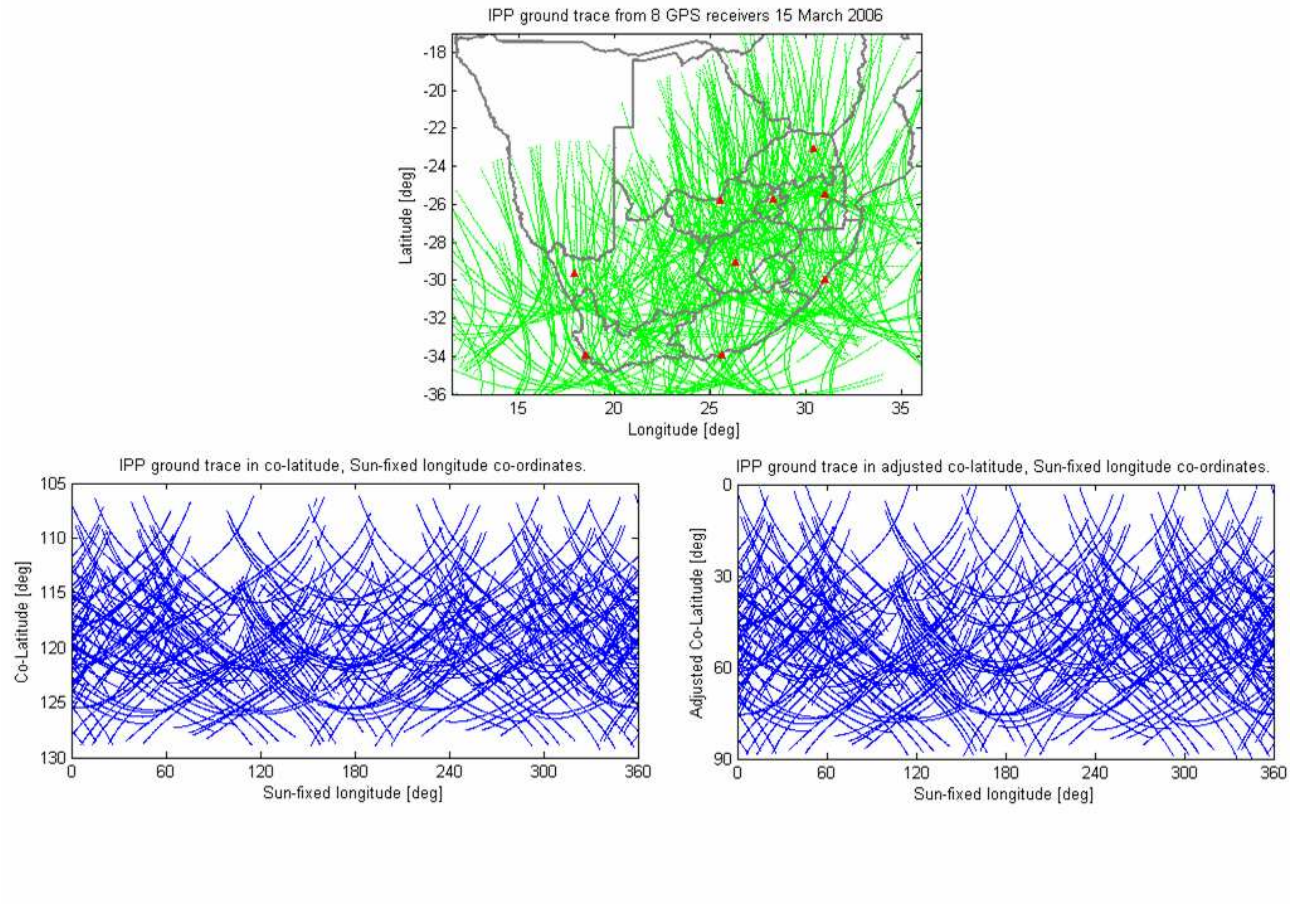

Figure 14. Ionospheric Pierce Point ground trace from 8 GPS receivers (red triangles, Table 4) expressed in geographic co-ordinates (top), Sun-fixed longitude and co-latitude (left) and Sun-fixed longitude and adjusted co-latitude (right). The IPP co-ordinates were calculated using a fixed assumed ionospheric shell height of 350 km.

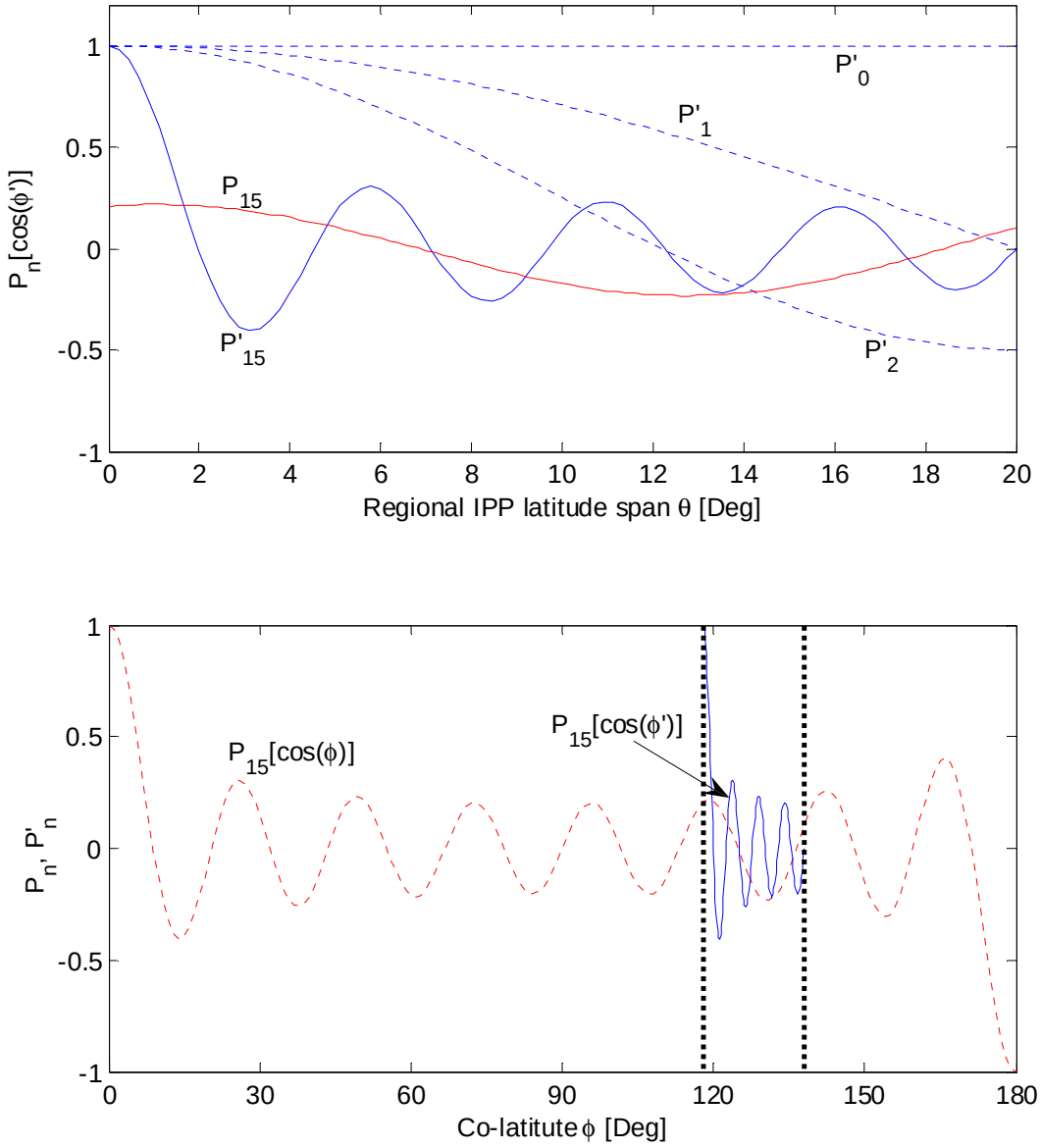

Figure 15. Comparison of $P_n^{'}$ and P_n for n = 0, 1, 2, 3 and 15. The top figure illustrates the 24° terrestrial wavelength of P_{15} (red), spanning the spherical 20° co-latitude interval [118°, 138°], superimposed on the equivalent 5.33° scaled terrestrial wavelength of $P_{15}^{'}$ (blue), on the same interval. The bottom figure relates this comparison in context of the spherical co-latitude.

5.2.3 Algorithm

Having presented the slant TEC quantification from GPS observables (Eqs. 3.39 and 3.40) and the adjusted co-latitude adaptation for the conventional spherical harmonic analysis, what remains is the derivation of the observation equations from which the spherical harmonic coefficients a_{nm}, b_{nm} (Eq. 5.1) and the satellite differential clock biases Δb^S, Δb^R (Eq. 3.37), required to calculate time and position-dependent TEC, are estimated.

Define the parameter μ from the speed of light, c and the L_1 carrier frequency f_1:

$$\mu = \frac{40.28}{c f_1^{\,2}} \tag{5.4}$$

The ionospheric time delay, $\Delta\tau_{ion}$, is defined from Eqs 3.30 and 5.4

$$\Delta\tau_{ion} = \mu \cdot TEC \tag{5.5}$$

The *slant* ionospheric delay (including DCBs (Δb_R, Δb_S) follows from Eqs. 3.37 - 3.40.

$$\begin{aligned} \Delta\tau_{ion} &= \mu \cdot \frac{VTEC}{\cos z'} + (\Delta b_R - \Delta b_S) \\ &= \mu\gamma \cdot VTEC + (\Delta b_R - \Delta b_S) \end{aligned} \tag{5.6}$$

Separate the SHM representation of the VTEC

$$VTEC(\lambda,\phi) = \sum_{n=0}^{N}\sum_{m=0}^{n}\overline{P}_{nm}[\cos(\phi)]\{a_{nm}\sin(m\lambda) + b_{nm}\cos(m\lambda)\} \qquad 5.7$$

into

$$VTEC(\lambda,\phi) = \sum_{n=0}^{N}\sum_{m=0}^{n}\overline{P}_{nm}[\cos(\phi)]\cdot a_{nm}\sin(m\lambda) + \sum_{n=0}^{N}\sum_{m=0}^{n}\overline{P}_{nm}[\cos(\phi)]\cdot b_{nm}\cos(m\lambda) \qquad 5.8$$

and substitute into Eq. 5.6, which renders the observational equation

$$\Delta\tau_{ion} = \mu\gamma\cdot\left(\sum_{n=0}^{N}\sum_{m=0}^{n}\overline{P}_{nm}[\cos(\phi)]\cdot a_{nm}\sin(m\lambda) + \sum_{n=0}^{N}\sum_{m=0}^{n}\overline{P}_{nm}[\cos(\phi)]\cdot b_{nm}\cos(m\lambda)\right) + \left(\Delta b_R - \Delta b_S\right) \qquad 5.9$$

5.2.4 Least squares solution

Let $\mathbf{X} = (a_{nm}, b_{nm}, \Delta b_R, \Delta b_S)$ represent the desired unknowns in the observational equation (Eq.5.9) and $F(\mathbf{X})_i \cong \Delta\tau_{ion,i}$ represent an estimated measurement calculated from $\mathbf{X}$ at the i^{th} epoch. The objective of the least squares solution is to determine those values of $\mathbf{X}$ which will minimise the sum of the squares of the residuals of the observations and the estimated (modelled) observations

$$\min\left(\sum_{i=1}^{p}\left(\Delta\tau_{ion,i} - F\left(\mathbf{X}\right)_i\right)^2\right),$$

where p represents the total number of observations.

Let $\mathbf{T} = [\Delta\tau_{ion}]_i$, $i = 1,\ldots p$ denote all the ionospheric delay observations. By considering all observations and unknowns in matrix notation, the observation model (Eq.5.9) is obatined by taking the partial derivatives of the measurements, $\Delta\tau_{ion}$ in Eq.5.9, w.r.t. the unknowns:

$$\mathbf{J} = \frac{\partial\mathbf{F}\left(\mathbf{X}\right)}{\partial\mathbf{X}}$$

with each matrix element J_{ij} given by

$$J_{ij} = \frac{\partial \mathbf{F}_i(\mathbf{X})}{\partial \mathbf{X}_j}$$
$$= \frac{\partial \Delta\tau_{ion,i}}{\partial \mathbf{X}_j}, i = 1,..p,\ j = 1,..q$$

where q represents the number of unknowns.

The partial derivatives contained in the Jacobian, are explicitly given by

$$\frac{\partial \mathbf{F}}{\partial a_{nm}} = \mu\gamma \sum\sum \bar{P}_{nm}[\cos\phi] \cdot \cos(m\lambda) \equiv \mathbf{J}_a$$
$$\frac{\partial \mathbf{F}}{\partial b_{nm}} = \mu\gamma \sum\sum \bar{P}_{nm}[\cos\phi] \cdot \sin(m\lambda) \equiv \mathbf{J}_b$$
$$\frac{\partial \mathbf{F}}{\partial \Delta b_R} = +1 \equiv \mathbf{J}_{bR} \qquad 5.10$$
$$\frac{\partial \mathbf{F}}{\partial \Delta b_S} = -1 \equiv \mathbf{J}_{bS}$$
$$\mathbf{J} = [\mathbf{J}_a \quad \mathbf{J}_b \quad \mathbf{J}_{bR} \quad \mathbf{J}_{bS}]$$

The total number of unknowns to be estimated is given by

$$q = 2\left(\sum_{n=0}^{N} n\right) + N_R + N_S$$

where N, N_R and N_S are respectively the SH degree, the number of GPS receivers and the number of GPS satellites.

Finally, the unknowns, **X**, are solved by weighted least squares

$$\mathbf{X} = \left(\mathbf{J}^{\mathrm{T}}\mathbf{W}\mathbf{J}\right)^{-1}\mathbf{J}^{\mathrm{T}}\mathbf{W}\mathbf{T} \qquad 5.11$$

where $\mathbf{W}_{pxp}$ is a weighted (diagonal) matrix constructed from observation variances

$$W_{ij} = \begin{cases} \sigma_i^{-2}, & i = j \\ 0, & i \neq j \end{cases}$$

5.2.5 Shell height assumptions

A Single Layer Model (SLM) ionosphere, using two different shell height assumptions in the cosec mapping function, was investigated in this study. The two height assumptions were a fixed single layer model (SLM, Eq. 4.4) with 350 km assumed shell height and a time-dependent shell height based on modelled *hmF2* values from the neural network-based South African Bottomside Ionosphere Model (SABIM) (McKinnell, 2003; McKinnell and Poole, 2004).

The variable shell height is an attempt at a more realistic presentation of the diurnal F2 peak density height (*hmF2*) variation. For this study, *hmF2* values were obtained from the South African Bottomside Ionosphere Model (SABIM). The SABIM is a neural network-based model developed using relevant geomagnetic parameters and South African ionosonde measurements (Grahamstown, Louisvale and Madimbo) and has been rigorously tested and evaluated in this region. The trained model calculates *hmF2* (and other ionospheric parameters) using time (year, day of year and UT hour) and geographic location as input parameters. The diurnal South African *hmF2* variation modelled from SABIM is illustrated in **Figure 16** as 2-hour interval contour maps for 20 March 2005.

Neural networks interpolate well within the data input space, but caution should be exercised otherwise. In the case of the SABIM, the ionosonde locations define the geographic input space. The SABIM models ionospheric parameters well within the region between the ionosondes, but values outside this region might not represent the actual values accurately; the south-western part of South Africa being a point in case due to lack of ionospheric measurements in this region. The SABIM-*hmF2* values calculated in this region (**Figure 16**) are probably higher than expected due to model extrapolation. The diurnal *hmF2* variation modelled at four distinct geographic locations (**Figure 17**) for 2005 equinox and solstice dates (**Figure 18**) further illustrates the interpolation/extrapolation.

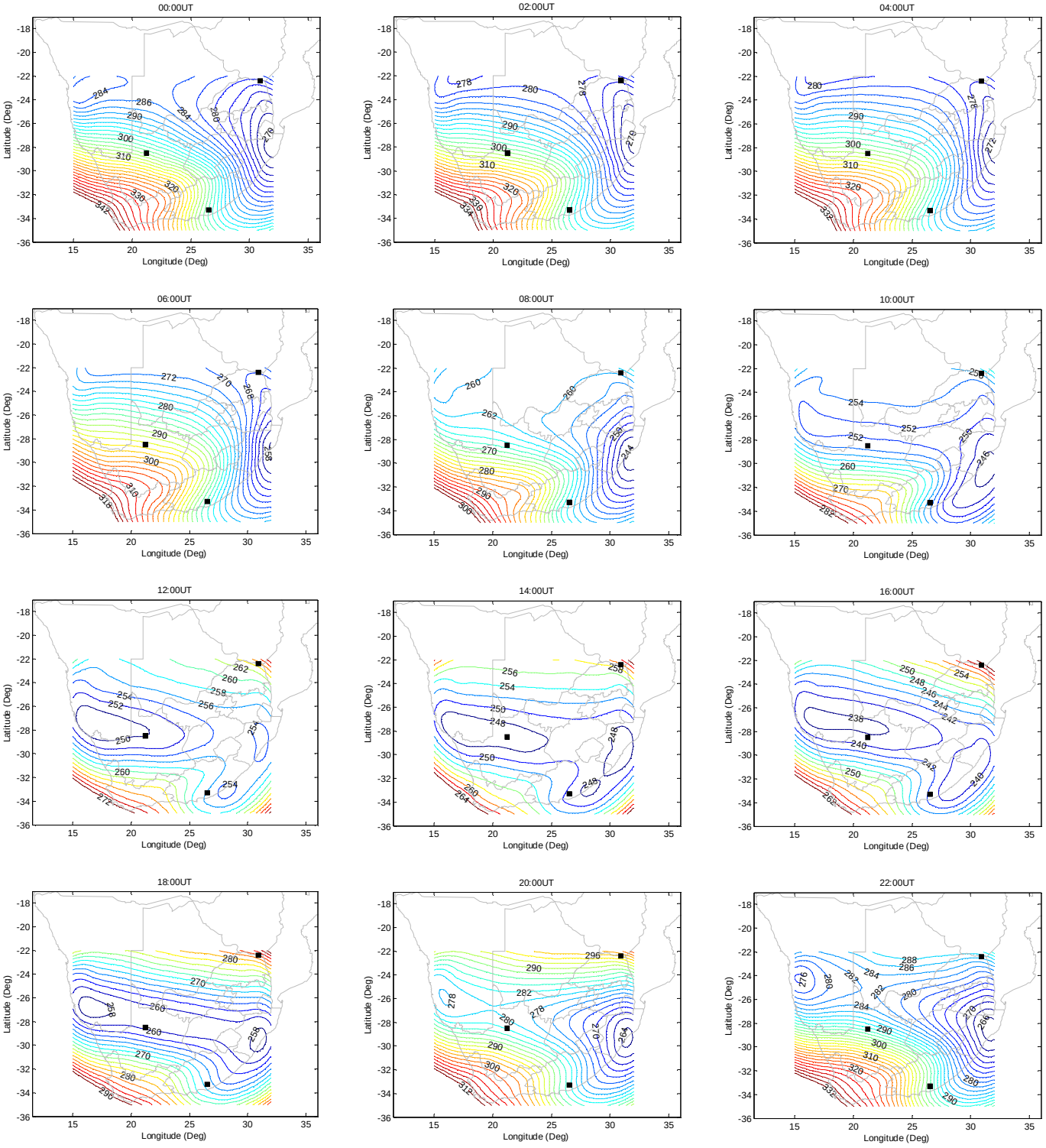

Figure 16. Modelled diurnal variation of ionospheric F2 peak density height (*hmF2*) over South Africa using neural network based South African Bottomside Ionosphere Model (SABIM) for 20 March 2005. Contour interval is 2 km. The black squares represent the three ionosonde locations.

The Thohoyandou, Grahamstown and Kimberly *hmF2* values for these dates do not differ by more than 30 km, but the SABIM modelled Cape Town values, however, exceed Thohoyandou *hmF2* by 60 km, which is not realistic as Thohoyandou *hmF2* should be higher than Cape Town because of its closer proximity to the equator. A comparison of IRI-derived *hmF2* values (**Figure 19**) confirms this. It is subsequently reasonable to assume that Cape Town *hmF2* values are over estimated due to aforementioned NN restrictions and, qualitatively, lower *hmF2* values could safely be assumed. Cape Town *hmF2* values are expected to agree more with Grahamstown values.

For the purpose of this study, the diurnal *hmF2* values modelled at Kimberley (24.81E, 28.74S), the approximate geographic centre of South Africa, are taken as the representative mean for the country and implemented as such in the thin-shell model. The assumption is reasonable as the Kimberley *hmF2* values represent a reasonable first order approximate mean between Grahamstown and Thohoyandou *hmF2* values (**Figure 18**). In the model implementation, diurnal *hmF2* values are calculated for the Kimberley location at 6-minute intervals and assumed constant between samples. These values then represent the thin-shell height in the cosec mapping functions for all observations from all South African GPS receivers. It is expected that a better agreement between ionosonde TEC and GPS-derived TEC might be achieved using the *hmF2* for shell height, especially at night, as the F2 peak density height significantly varies during the day and could have a significant impact on the spatial distribution of TEC values. The SABIM-*hmF2* heights should also be more realistic than IRI-*hmF2*.

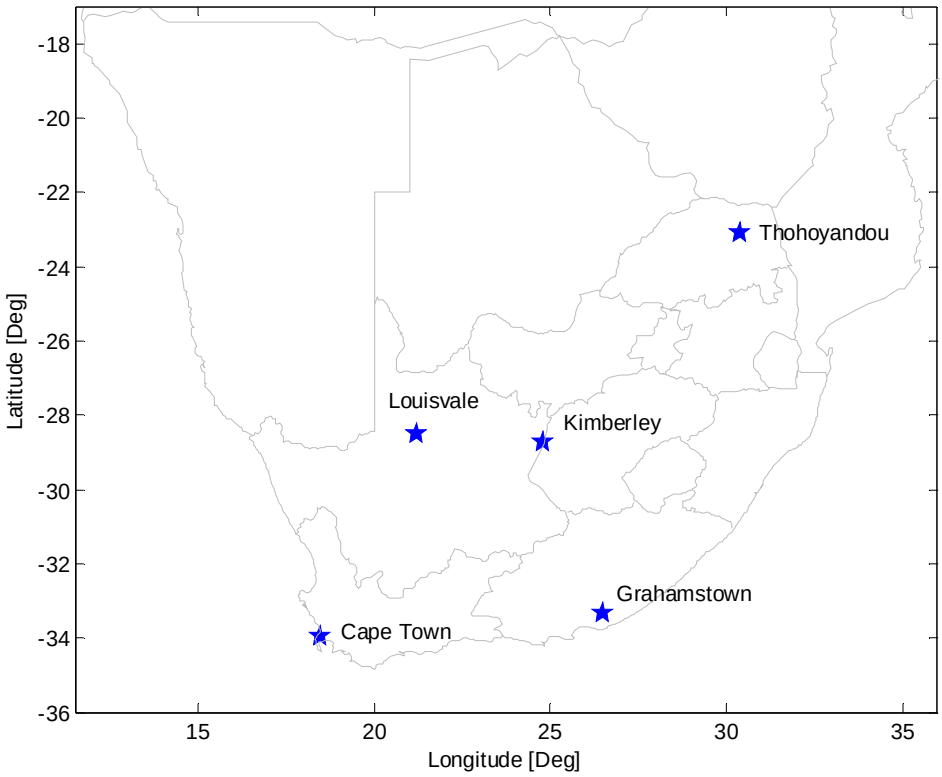

Figure 17. Geographic locations for which SABIM and IRI 2005 solstice and equinox diurnal *hmF2* values were compared. Thohoyandou (30.84°E, 23.08°S), Kimberley (24.81°E, 28.74°S), Cape Town (18.46°E, 33.95°S) and Grahamstown (26.53°E, 33.30°S).

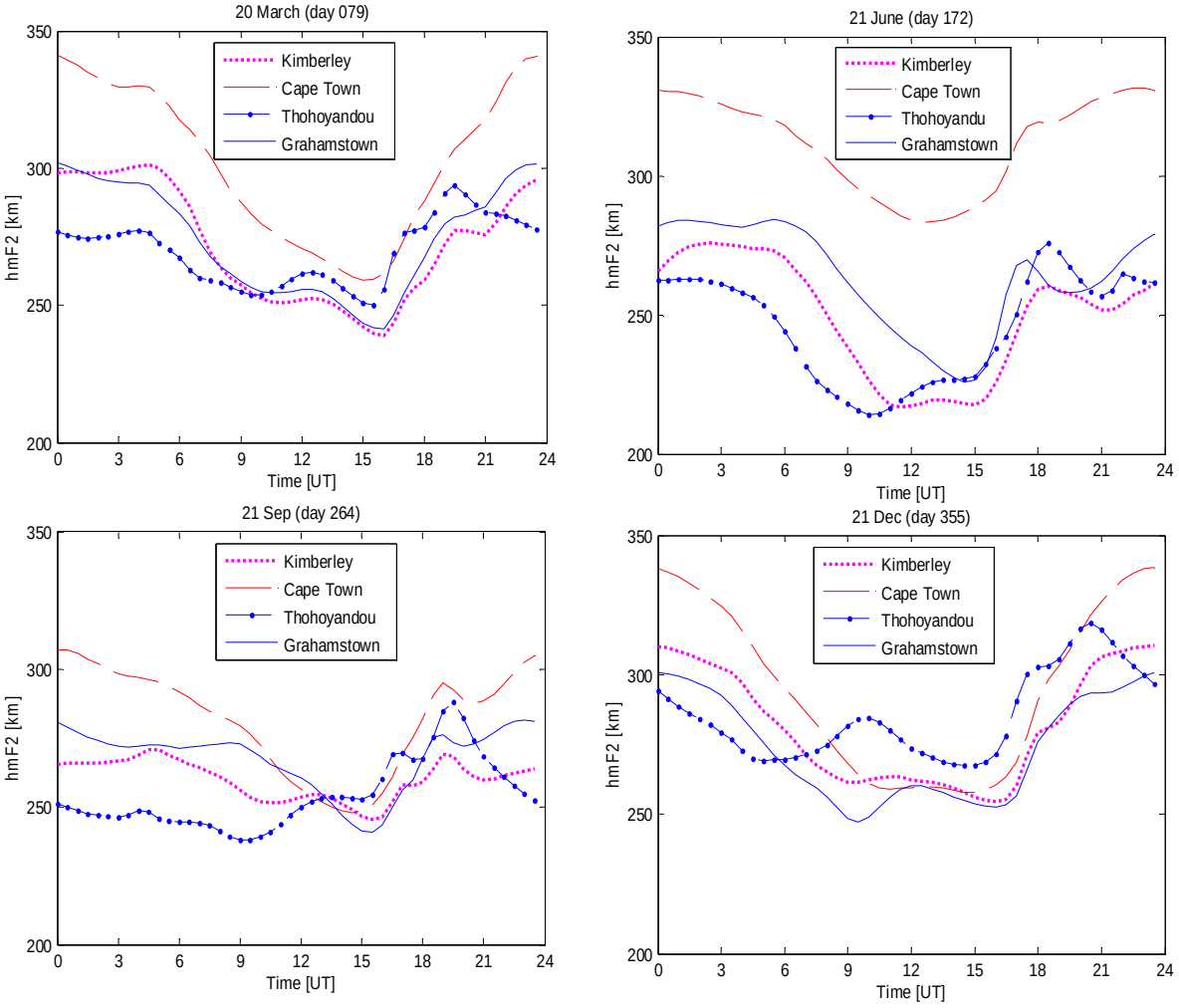

Figure 18. SABIM-modelled diurnal *hmF2* variation at four South African locations for 2005 equinox and solstice dates. The SABIM has as yet not been trained to accommodate 2006 ionospheric predictions.

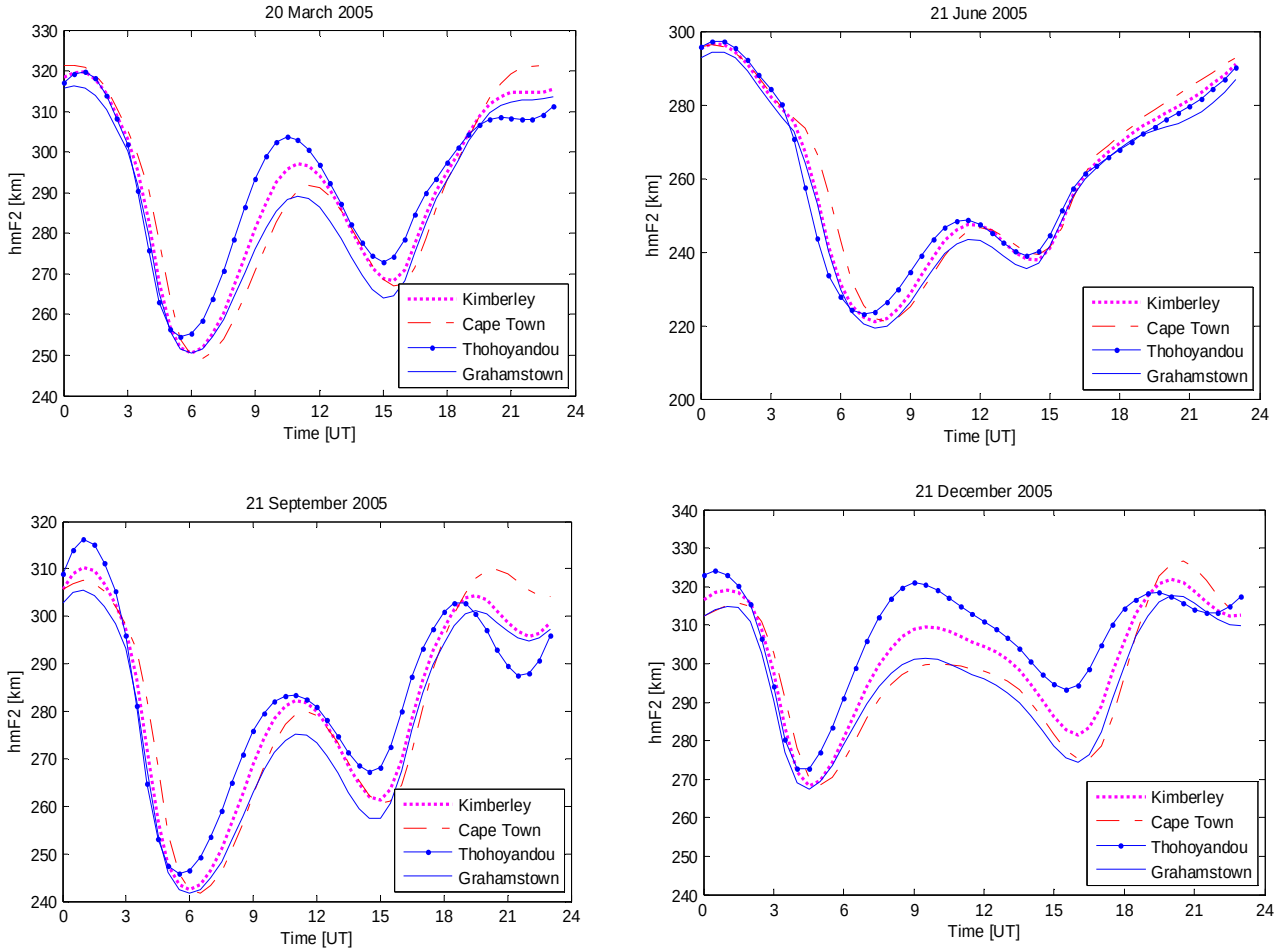

Figure 19 IRI-modelled *hmF2* variation at four South African locations for 2005 equinox and solstice dates.

5.2.6 Software implementation of spherical harmonic model

For the purpose of this study, the presented mathematical model was implemented in MATLAB®, a high-level interpreter software language. A schematic layout of the major steps is presented in Table 1.

Table 1 Summary of HMO_TEC program.

Step 1	Procure and pre-process relevant RINEX GPS observation data and sp3 data satellite position files; conduct data integrity testing and create necessary directory structures.
Step 2	Batch reading of RINEX observables and satellite positions.
Step 3	Time-synchronise all code and phase pseudo range observables from all receivers.
Step 4	Calculate geographic locations of IPPs using the thin-shell model.
Step 5	Calculate code- and phase-derived TEC (Eqs 3.37 and 3.39).
Step 6	Phase-level phase-derived TEC measurements (Eq. 3.40).
Step 7	Assimilate all phase-derived TEC measurements and associated IPP locations for all receivers and all satellites.
Step 8	Calculate statistics (standard deviation) on all slant phase-derived TEC observations.
Step 9	IPP longitude and latitude scaling to sun-fixed longitude and (adjusted) co-latitude.
Step 10	Construct Jacobian matrix from TEC time-delay measurements (Eq. 5.10).
Step 11	Estimation of spherical harmonic coefficients and satellite and receiver DCBs by weighted least squares method (Eq. 5.11).
Step 12	Create diurnal or time-dependent TEC maps by SHM interpolation using estimated coefficients.
Step 13	Save estimated SHM coefficients, satellite and receiver DCBs and estimated diurnal TEC.

5.3 Model testing using simulated (IRI) data.

The software implementation of the ASHA algorithm was tested using TEC observations simulated from the IRI2001 model (Bilitza, 2001). Simulated *slant* TEC observations along actual GPS satellite signal paths were generated using the IRI model with a time interval of 60 seconds for a twenty-four hour period for 2006 equinox and solstice days. For any given epoch, a raypath's azimuth and elevation were used to calculate the geographic location of a point on the raypath where the vertical altitude was 80km. A single electron density value was then calculated from the IRI model for the given epoch and position. The vertical height was subsequently incremented by *dh* (20 km) to 100 km and the electron density was calculated at this epoch and position as before. The process was repeated by calculating individual electron density values along the raypath up to 2000 km vertical

height, rendering N_d electron density values on the signal path. The slant distance corresponding to the *dh* vertical height increase, given by *dh*/sin(*elevation*), was used to integrate through the N_d electron density values to arrive at a slant IRI-TEC values for the given epoch. The simulated TEC values were converted to time delays and used as input in the ASHA model (Eq. 5.9) to estimate the spherical harmonic coefficients and instrumental DCBs using a 15-degree and order spherical harmonic expansion. An IRI reference diurnal *vertical* TEC profile was calculated with 60-second time interval. A diurnal vertical TEC profile was interpolated from the estimated spherical harmonic coefficients (Eq. 5.11). The interpolated diurnal vertical TEC profiles were compared to the IRI-derived reference diurnal vertical TEC profiles for the dates in case (**Figure 20**). The estimated DCBs were compared to the reference DCBs. A good agreement between the interpolated and reference profiles would be an indication of the correct software implementation of the mathematical model. By definition, TEC must be positive. The difference between the reference vertical IRI TEC profile and ASHA and CSHA estimated diurnal TEC profiles are illustrated in **Figure 21**. The differences between the reference and estimated satellite and receiver DCBs are listed in **Table 2**.

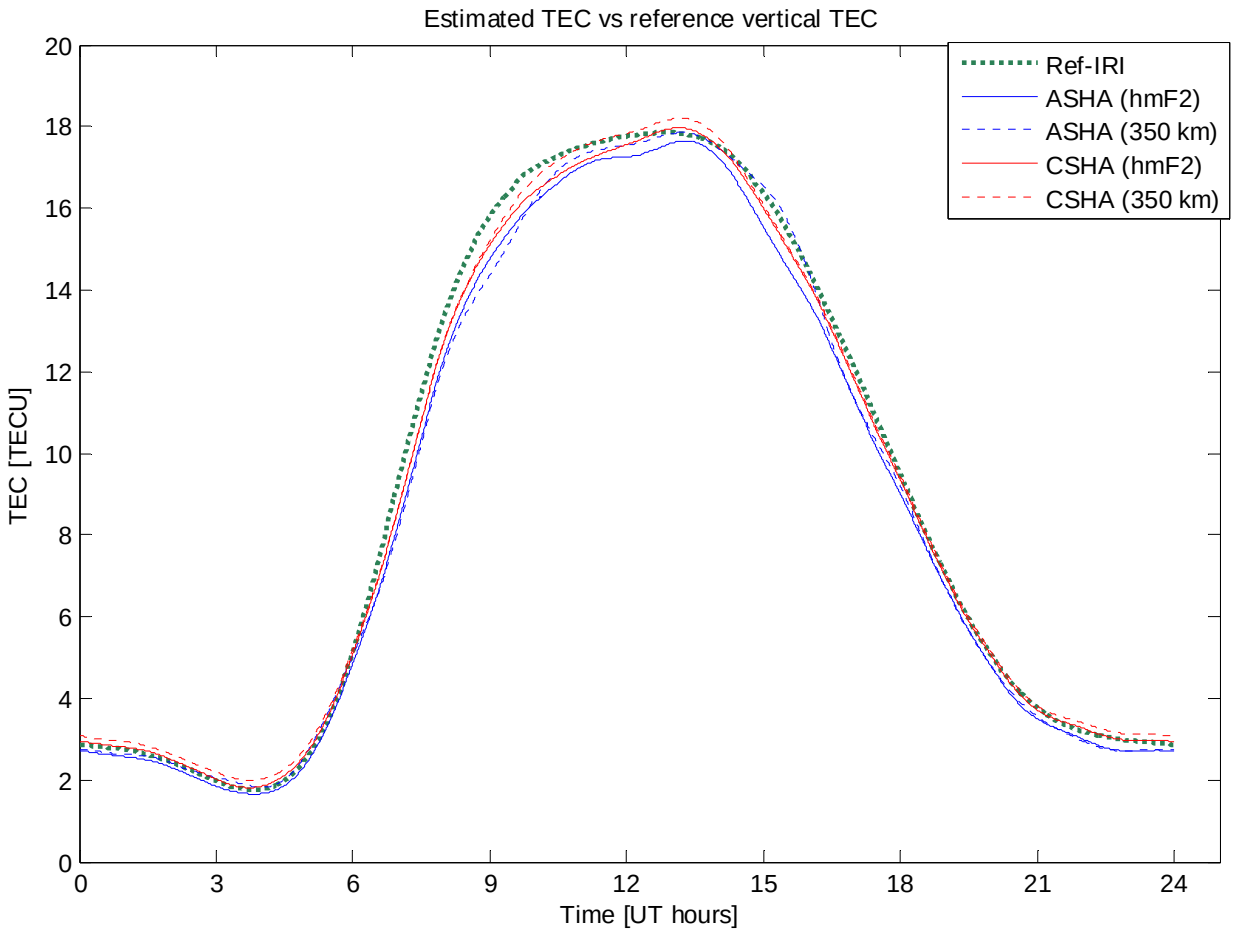

Figure 20 Comparison of reference diurnal vertical IRI-TEC variation (thick broken green line) and GPS-TEC estimated from slant IRI-simulated TEC measurements using different implementations of the ASHA algorithm. Results are indicated for ASHA (blue) and the conventional CSHA (red) employing the single layer mapping (SLM) function with a fixed assumed ionospheric shell height of 350 km and an IRI-derived *hmF2*-varying shell height. Observations were simulated for the Grahamstown location on 15 March 2006.

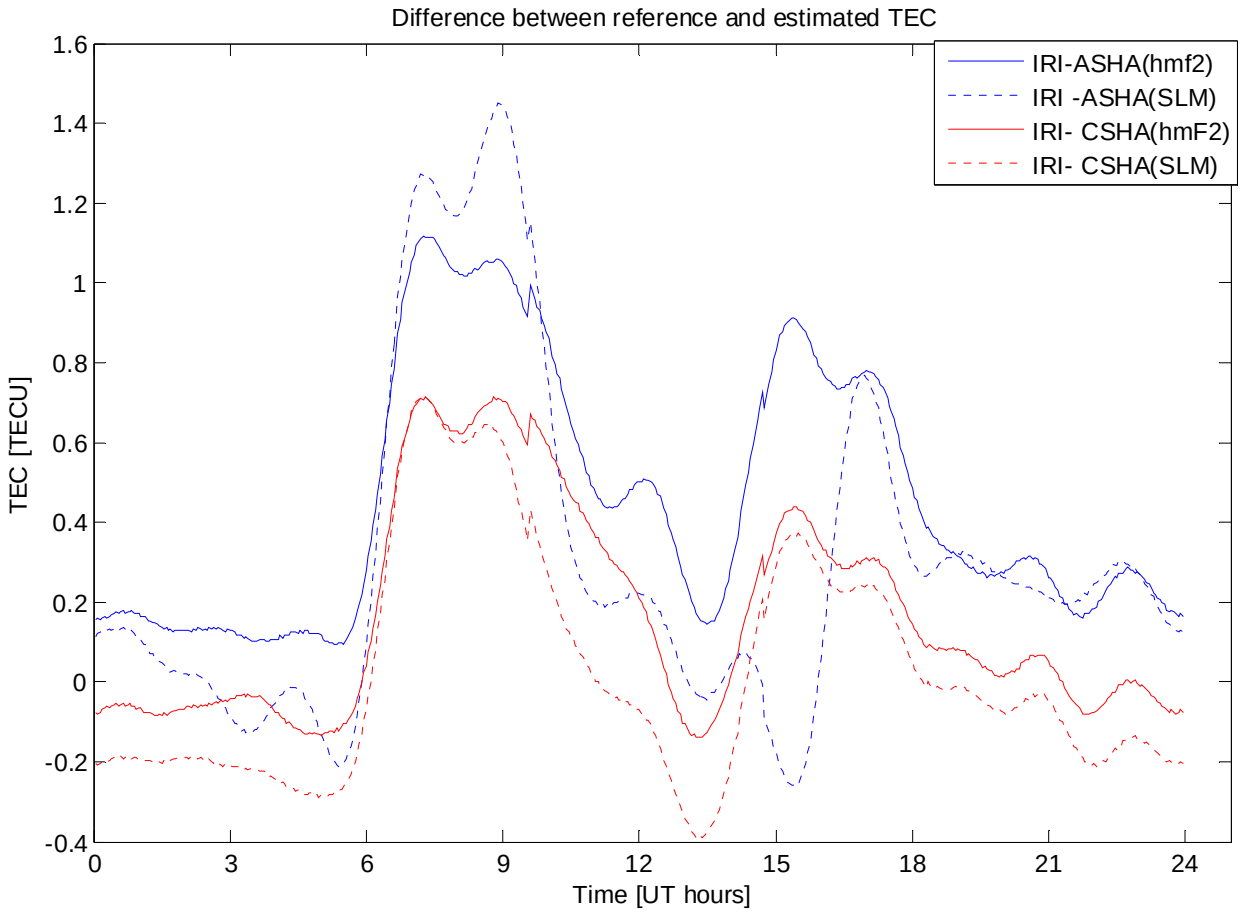

Figure 21. Differences between the reference IRI vertical TEC and the various ASHA TEC results estimated from simulated slant IRI-TEC observations. The rms, in TECU, of the respective differences are 0.5437 (IRI-ASHA(*hmf2*), 0.5200 (IRI-ASHA (SLM), 0.3044 (IRI-CSHA (*hmf2*) and 0.2812 (IRI-CSHA(SLM)).

Table 2. Estimated GPS receiver (Rx) and satellite DCBs in nanoseconds (ns), using ASHA and CSHA options with simulated observations for a single GPS receiver located at Grahamstown, 15 March 2006 using different shell height assumptions**.**

Instrument	Ref DCBs	ASHA (*hmf2*)	Ref - ASHA (*hmf2*)	ASHA (SLM)	Ref - ASHA (SLM)	CSHA (*hmf2*)	Ref - CSHA (*hmf2*)	CSHA (SLM)	Ref - CSHA (SLM)
PRN#1	-1.3534	-1.248	-0.1054	-1.348	-0.0054	-1.192	-0.1614	-1.308	0.0454
PRN#2	1.3534	1.225	0.1284	1.276	0.0774	1.23	0.1234	1.234	-0.1194
PRN#3	-1.3534	-1.509	0.1556	-1.531	0.1776	-1.487	0.1336	-1.541	-0.1876
PRN#4	1.3534	1.208	0.1454	1.264	0.0894	1.217	0.1364	1.223	-0.1304
PRN#5	-1.3534	-1.347	-0.0064	-1.268	-0.0854	-1.468	0.1146	-1.484	-0.1306
PRN#6	1.3534	1.186	0.1674	1.181	0.1724	1.182	0.1714	1.172	-0.1814
PRN#7	-1.3534	-1.523	0.1696	-1.533	0.1796	-1.52	0.1666	-1.527	-0.1736
PRN#8	1.3534	1.48	-0.1266	1.534	-0.1806	1.334	0.0194	1.351	-0.0024
PRN#9	-1.3534	-1.57	0.2166	-1.669	0.3156	-1.543	0.1896	-1.57	-0.2166
PRN#10	1.3534	1.242	0.1114	1.291	0.0624	1.251	0.1024	1.256	-0.0974
PRN#11	-1.3534	-1.125	-0.2284	-1.093	-0.2604	-1.229	-0.1244	-1.172	0.1814
PRN#13	1.3534	1.198	0.1554	1.267	0.0864	1.167	0.1864	1.174	-0.1794
PRN#14	-1.3534	-1.079	-0.2744	-0.902	-0.4514	-1.148	-0.2054	-1.169	0.1844
PRN#15	1.3534	1.26	0.0934	1.171	0.1824	1.28	0.0734	1.306	-0.0474
PRN#16	-1.3534	-1.292	-0.0614	-1.359	0.0056	-1.205	-0.1484	-1.313	0.0404
PRN#17	1.3534	1.259	0.0944	1.332	0.0214	1.287	0.0664	1.313	-0.0404
PRN#18	-1.3534	-1.46	0.1066	-1.48	0.1266	-1.44	0.0866	-1.437	-0.0836
PRN#19	1.3534	1.509	-0.1556	1.153	0.2004	1.46	-0.1066	1.48	0.1266
PRN#20	-1.3534	-1.214	-0.1394	-1.104	-0.2494	-1.235	-0.1184	-1.17	0.1834
PRN#21	1.3534	1.195	0.1584	1.174	0.1794	1.236	0.1174	1.226	-0.1274
PRN#22	-1.3534	-0.933	-0.4204	-0.752	-0.6014	-1.003	-0.3504	-0.904	0.4494
PRN#23	1.3534	1.4	-0.0466	1.386	-0.0326	1.463	-0.1096	1.409	0.0556
PRN#24	-1.3534	-1.46	0.1066	-1.389	0.0356	-1.432	0.0786	-1.408	-0.0546
PRN#25	1.3534	1.367	-0.0136	1.279	0.0744	1.448	-0.0946	1.326	-0.0274
PRN#26	-1.3534	-1.519	0.1656	-1.52	0.1666	-1.462	0.1086	-1.457	-0.1036
PRN#27	1.3534	1.509	-0.1556	1.097	0.2564	1.408	-0.0546	1.438	0.0846
PRN#28	-1.3534	-1.42	0.0666	-1.361	0.0076	-1.392	0.0386	-1.366	-0.0126
PRN#29	1.3534	1.187	0.1664	1.198	0.1554	1.244	0.1094	1.256	-0.0974
PRN#30	-1.3534	-1.183	-0.1704	-1.022	-0.3314	-1.271	-0.0824	-1.236	0.1174
rms (ns)			**0.1620**		**0.2126**		**0.1377**		**0.1476**
rms (TECU)			**0.2993**		**0.3928**		**0.2545**		**0.2728**
Rx DCB (ns)	**-1.8947**	**-1.658**		**-1.727**		**-1.819**		**-1.898**	
Rx DCB (TECU)	**-3.5**	**-3.0627**		**-3.1902**		**-3.3601**		**-3.5061**	

5.4 Model evaluation

The relatively good comparisons of the estimated TEC and DCBs in the presented test case gave sufficient confidence in the successful mathematical implementation of the ASHA algorithm in software. The ASHA algorithm was subsequently quantatively evaluated by comparing its estimated TEC results with ionosonde measurements, MIDAS and GIM GPS results and with TOPEX/Poseidon and Jason-1 satellite based radar altimeter TEC measurements. The following test cases were investigated

5.4.1 Test case 1: Single receiver comparisons with ionosonde, MIDAS and GIM TEC.

The ASHA model was evaluated for single receivers by comparing diurnal TEC profiles estimated from single GPS receivers located at Grahamstown (**Test case 1A)**, Thohoyandou (**Test case 1B)** and Upington (**Test case 1C)** and compared with ionosonde measurements respectively recorded at Grahamstown, Madimbo and Louisvale close to 2006 equinox/solstice dates. These days were geomagnetically quiet with maximum K-index value of 3 as illustrated by the K-index values recorded at Hermanus, South Africa (**Figure 22**). The estimated ASHA GPS-TEC results were for these dates and locations were also compared to GPS-TEC values from MIDAS and CODEs Global Ionospheric Map TEC values. MIDAS TEC values for these dates and locations were obtained by conducting computerised ionospheric tomography using observations from between 32 and 36 GPS receivers distributed through South Africa and by integrating through the CIT-derived electron density profiles. The results for the test cases are presented in **Figure 23** (**Test case 1A**), **Figure 24** (**Test case 1B)** and **Figure 25** (**Test case 1C)**. In **Table 3** the satellite DCBs estimated in **Test case 1A** using the ASHA method, is compared to those estimated and disseminated by CODE for the same dates**.**

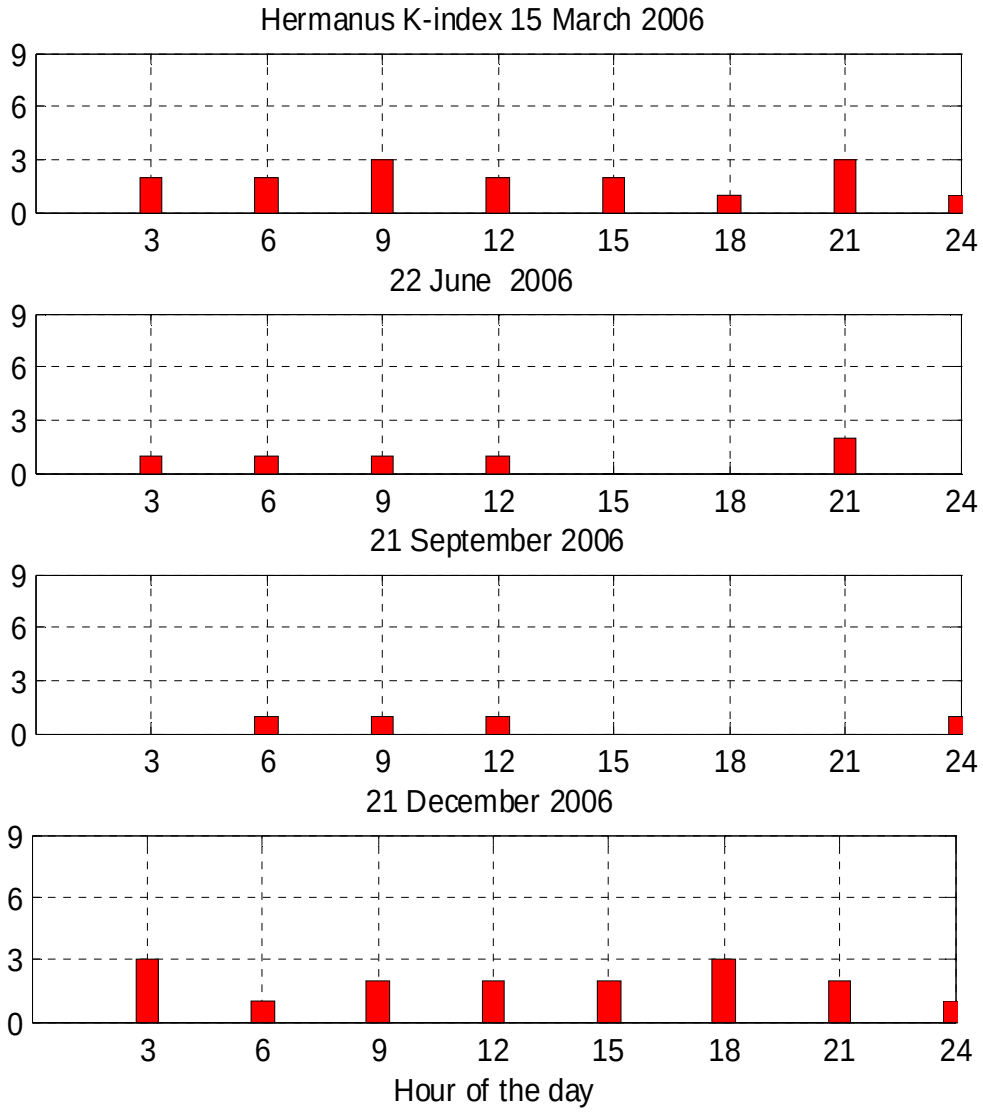

Figure 22. K-indices produced by the Hermanus Magnetic Observatory for 2006 near solstice and equinox dates. The low K-indices for these dates indicate magnetically quiet conditions.

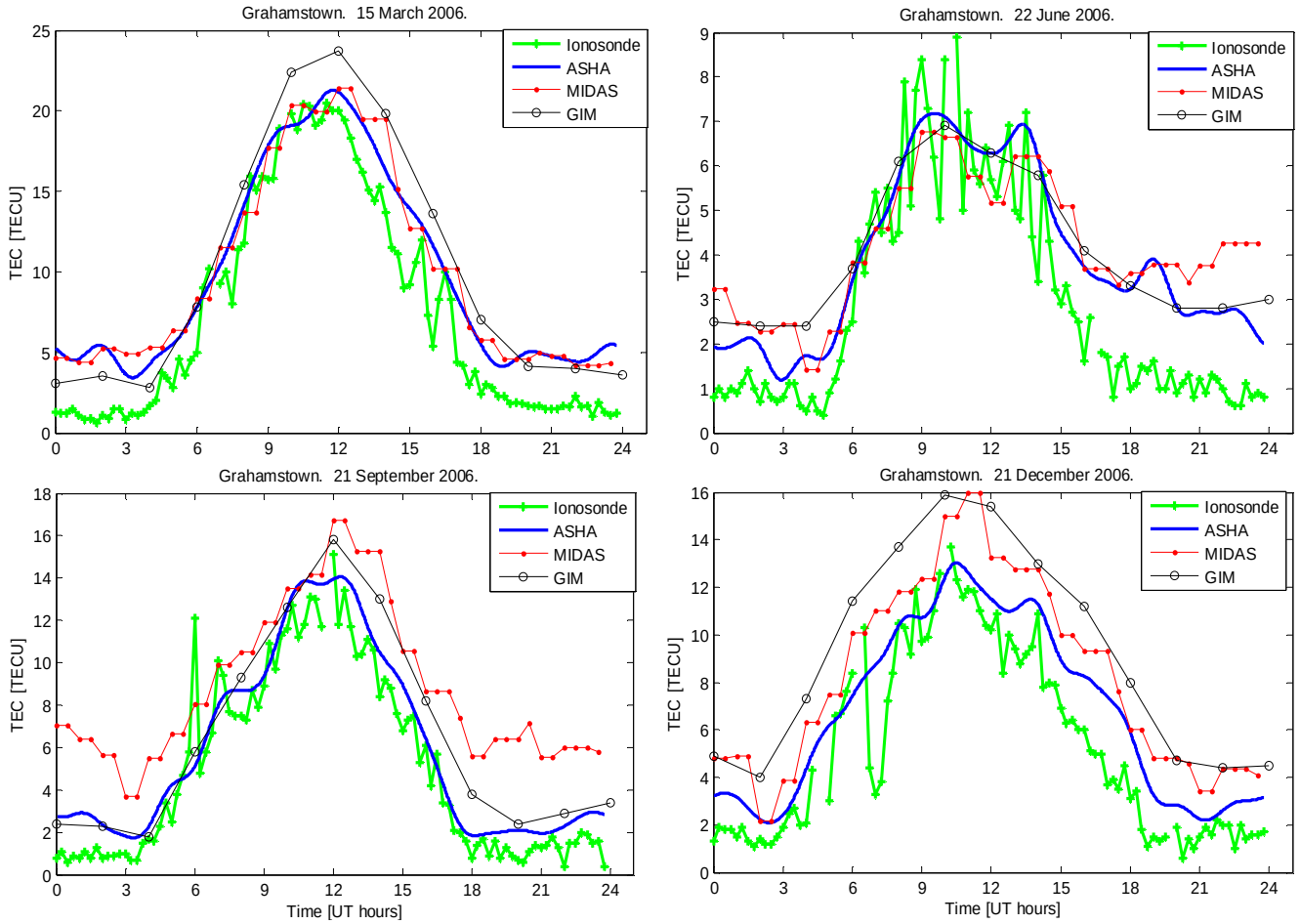

Figure 23. Test case 1A: Comparison of measured Grahamstown ionosonde TEC with ASHA, MIDAS and GIM GPS-derived TEC results close to 2006 solstice and equinox dates.

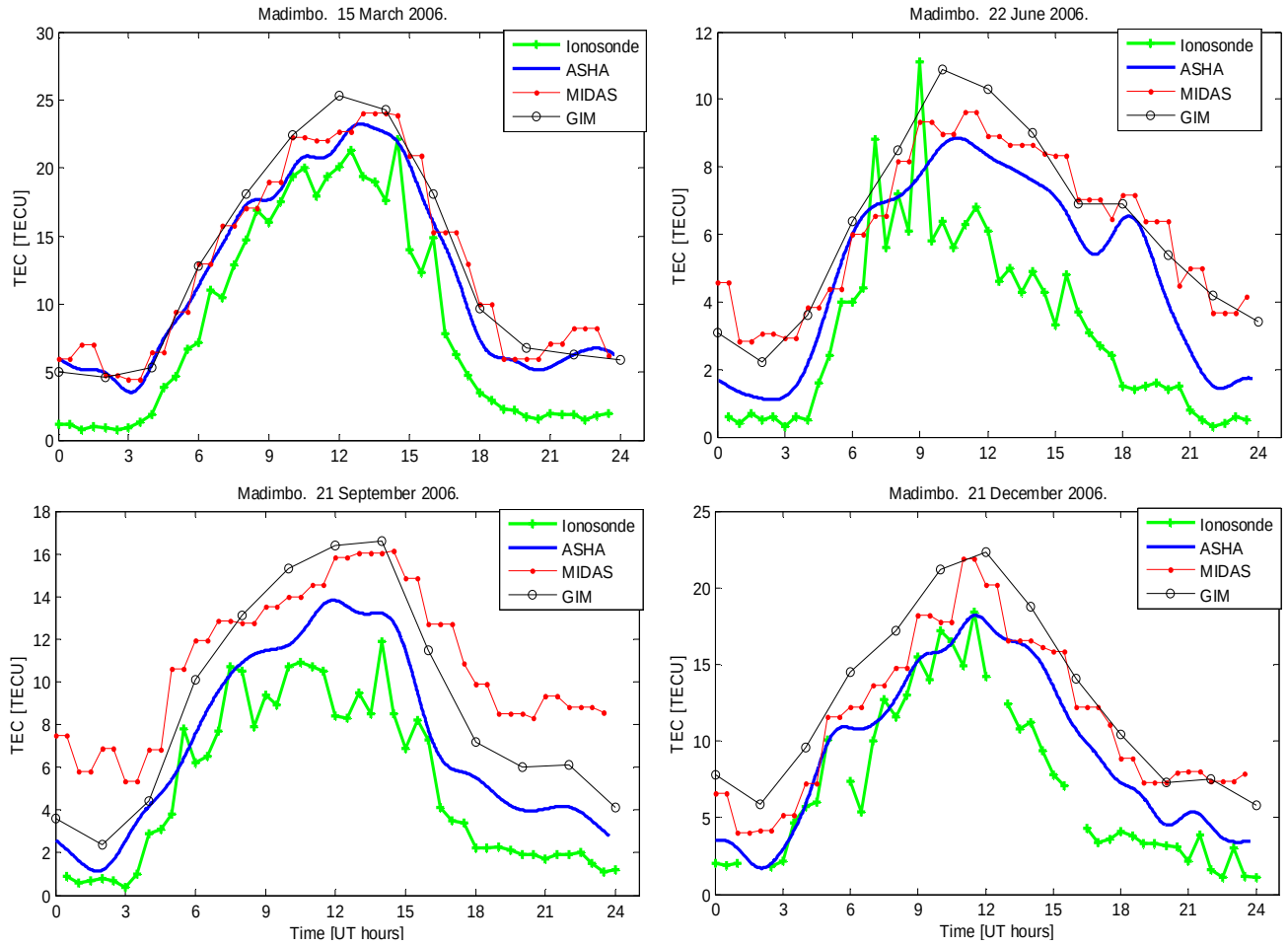

Figure 24. Test case 1B: Comparison of measured Madimbo ionosonde TEC with ASHA, MIDAS and GIM GPS-derived TEC results close to 2006 solstice and equinox dates.

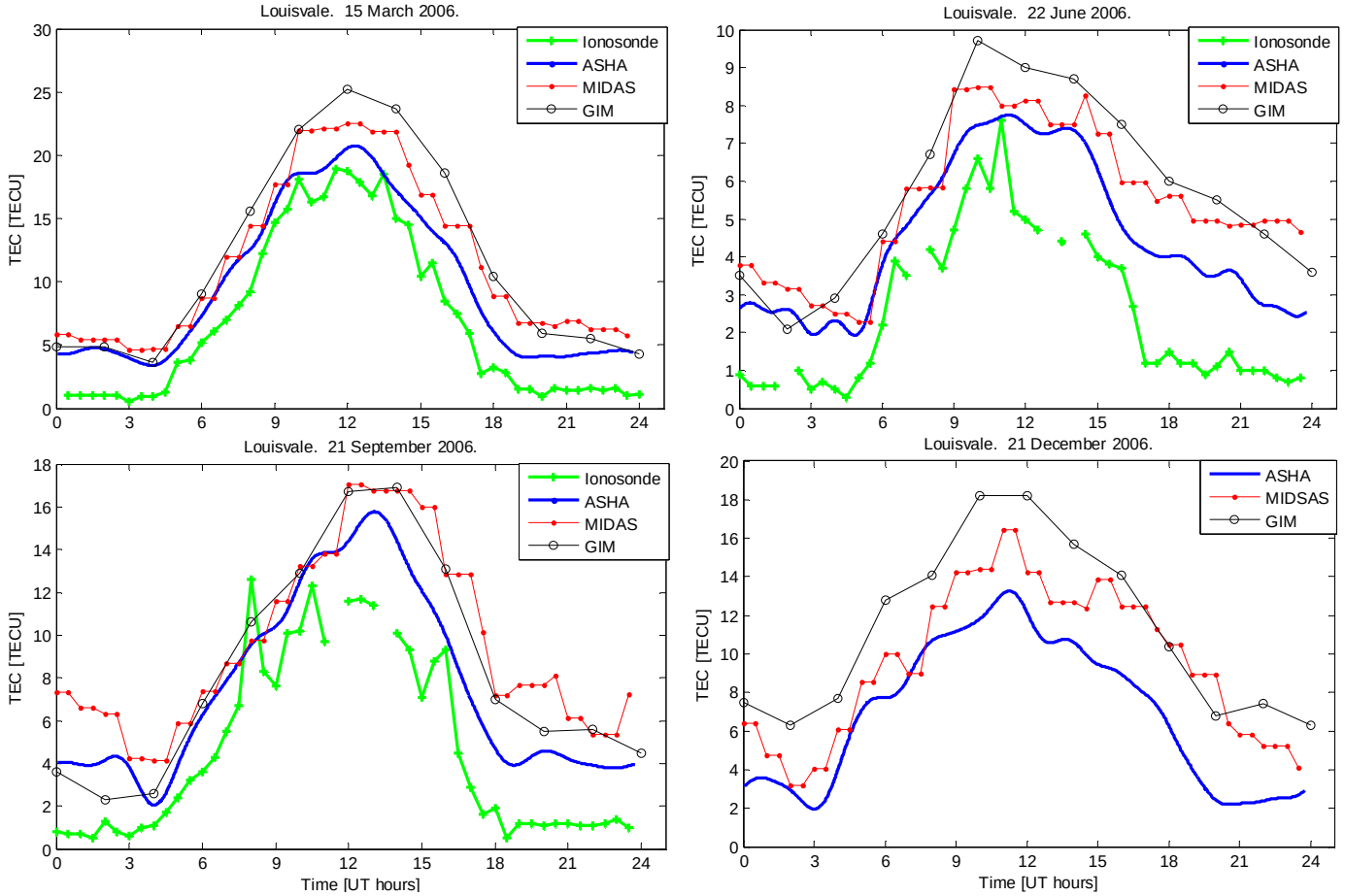

Figure 25. Test Case 1C: Comparison of measured Louisvale ionosonde TEC with ASHA, MIDAS and GIM GPS-derived TEC results close to 2006 solstice and equinox dates. No ionosonde data was registered at Louisvale during the period 1 Dec 2006 – 1 May 2007.

Table 3. Satellite DCBs as estimated by the ASHA algorithm from Grahamstown GPS receiver data for 2006 dates (**Test case 1A**). DCBs are compared to those estimated by CODE from a global GPS receiver network. DCBs are given in TEC units.

	15 Mar		22 June		21 Sep		21 Dec	
GPS sat	CODE	GRHM	CODE	GRHM	CODE	GRHM	CODE	GRHM
1	-3.09	10.88	-3.03	8.63	-3.07	6.65	-3.21	6.87
2	5.83	-17.49	5.87	-16.67	5.89	-17.69	5.69	-17.17
3	-2.52	7.29	-2.61	6.99	-2.51	3.79	-2.70	3.93
4	-1.35	2.70	-1.21	3.53	-1.33	5.87	-1.53	6.49
5	-2.58	8.36	-2.46	6.96	-2.48	3.01	-2.84	3.92
6	-2.11	5.56	-2.15	6.09	-2.18	5.32	-2.28	5.41
7	-4.01	10.57	-4.03	11.66	-4.05	7.52	-4.18	3.85
8	-2.88	7.42	-2.79	8.08	-2.92	5.87	-3.07	6.86
9	-1.69	4.91	-1.66	4.71	-1.68	3.06	-1.89	4.54
10	-3.74	9.04	-3.79	11.34	-3.78	3.54	-3.95	4.84
11	2.43	-5.47	2.42	-6.64	2.37	-6.28	2.21	-6.06
12	na	na	na	na	na	na	2.25	-2.35
13	2.16	-6.22	2.12	-5.71	2.04	-2.11	1.85	-2.16
14	0.80	-0.76	0.84	-1.49	0.79	-2.83	0.63	-2.65
15	-3.61	9.99	-3.69	10.93	-3.69	na	-3.92	na
16	1.10	-2.22	1.08	-2.58	1.07	-6.03	0.90	-5.82
17	1.04	-2.05	0.92	-2.60	1.55	-0.75	1.33	-1.33
18	1.50	-3.69	1.56	-4.11	1.75	-7.13	1.58	-6.11
19	4.15	-11.00	4.04	-10.53	4.02	-17.43	3.77	-17.31
20	-0.95	4.47	-0.86	3.22	-0.95	-1.59	-1.20	-2.42
21	2.45	-7.56	2.35	-6.14	2.37	-8.35	2.17	-7.90
22	6.55	-17.47	6.49	-18.62	6.45	-17.20	6.32	-16.67
23	8.69	-23.29	8.72	-23.25	8.60	-24.29	8.40	-23.04
24	-4.51	12.65	-4.54	12.48	-4.61	11.04	-4.76	11.20
25	-0.79	1.54	-0.44	na	-0.46	1.27	-0.59	0.39
26	-1.11	2.34	-1.24	3.09	-1.20	5.00	-1.48	5.47
27	-2.38	6.38	-2.35	6.85	-2.48	4.43	-2.63	4.63
28	1.44	-3.45	1.37	-2.58	1.37	-4.94	1.26	-5.67
29	-0.84	0.91	-1.00	2.11	-0.96	3.17	-1.24	3.04
30	0.01	0.89	0.05	-0.82	0.09	3.99	-0.12	4.71
31	na	na	na	na	na	na	3.20	-5.00

5.4.2 Test Case 2: Two-dimensional evaluation using IRI -simulated and observed GPS observations.

To evaluate the ASHA algorithm's capability at estimating two-dimensional TEC over a large region such as South Africa, *slant* IRI-TEC observations were simulated for multiple South African GPS receivers (**Table 4**) and 2D vertical TEC maps were interpolated on a 0.25°x0.25° longitude/latitude grid using the estimated spherical harmonic coefficients from a 12-degree model (Eq. 5.11). The procedure was repeated for the CSHA algorithm. The ASHA and CSHA algorithms were evaluated by comparing 2D TEC maps derived using time-varying IRI-*hmF2* values in the cosec mapping function (**Test cases 2A and 2C**) and a fixed assumed ionospheric shell height of 350 km (**Test cases 2B and 2D**) to 2D *vertical* IRI reference TEC maps. Finally, the ASHA and SCHA 2D TEC maps derived from actual GPS measurements (**Table 4**) were compared (**Test case 2E**). The results for selected hours on 15 March 2006 are presented in **Figure 26** (**Test case 2A**), **Figure 27** (**Test case 2B**), **Figure 28** (**Test case 2C**), **Figure 29** (**Test case 2C**) and **Figure 30** (**Test case 2E)**. For DCB analysis, biases of respectively +/- 2.5 TECU (1.3534 ns) for satellites and +/- 3.5 TECU (1.8947 ns) for receivers were used in the IRI-simulated test cases **2A-D**. Statistics on the differences between reference and estimated DCBs are presented in **Table 5**-**Table 8**. In **Table 9** the estimated satellite and receiver DCBs are compared for test cases **2A-D**. Statistics on the difference between ASHA and CSHA for **Test case 2E** is presented in **Table 10**. For the sake of completeness, the estimated DCBs for **Test case 2E** is presented in **Table 11**. A maximum IRI-height of 2 000 km was considered.

Table 4. Location of GPS receivers used for Test case 2: 2D TEC map evaluation

Receiver code	Receiver	Position (Longitude, Latitude)
BFTN	Bloemfontein	26.30, -29.10
MBRY	Cape Town	18.47, -33.95
DRBN	Durban	30.95, -29.97
MFKG	Mafikeng	25.54, -25.81
NSPT	Nelspruit	30.98, -25.48
PELB	Port Elizabeth	25.61, -33.98
PRET	Pretoria	28.28, -25.73
SBOK	Springbok	17.88, -29.67
TDOU	Thohoyandou	30.38, -23.10

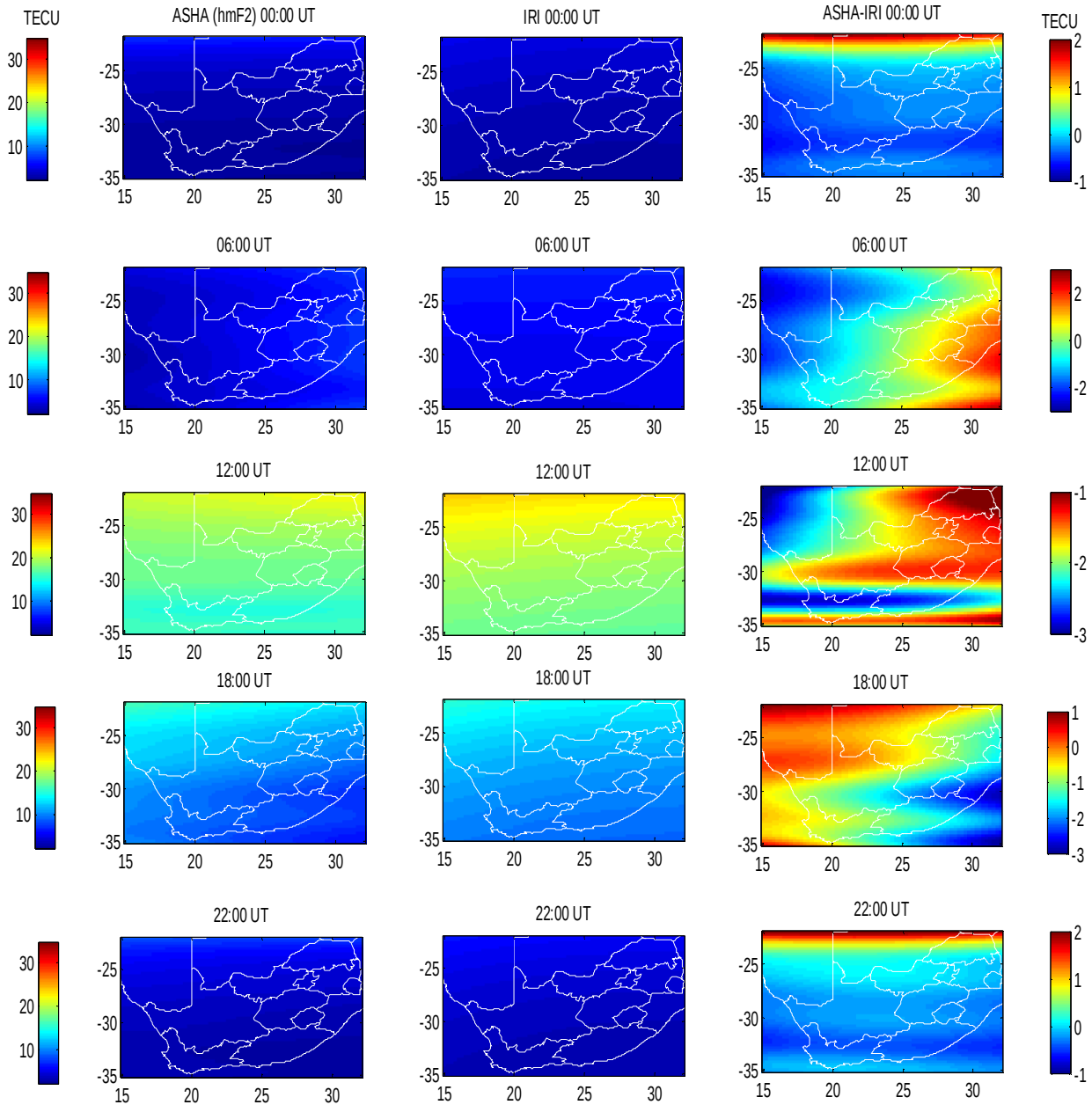

Figure 26. Test case 2A: Comparison of ASHA estimated 2D vertical TEC maps using simulated IRI slant TEC observed by eight receivers and reference 2D vertical IRI TEC maps for 15 March 2006 (day 74). A 12th degree and order harmonic expansion and an IRI-derived *hmF2* varying thin-shell height were used in the analysis. The 3rd column illustrates the difference between the estimated and reference TEC results.

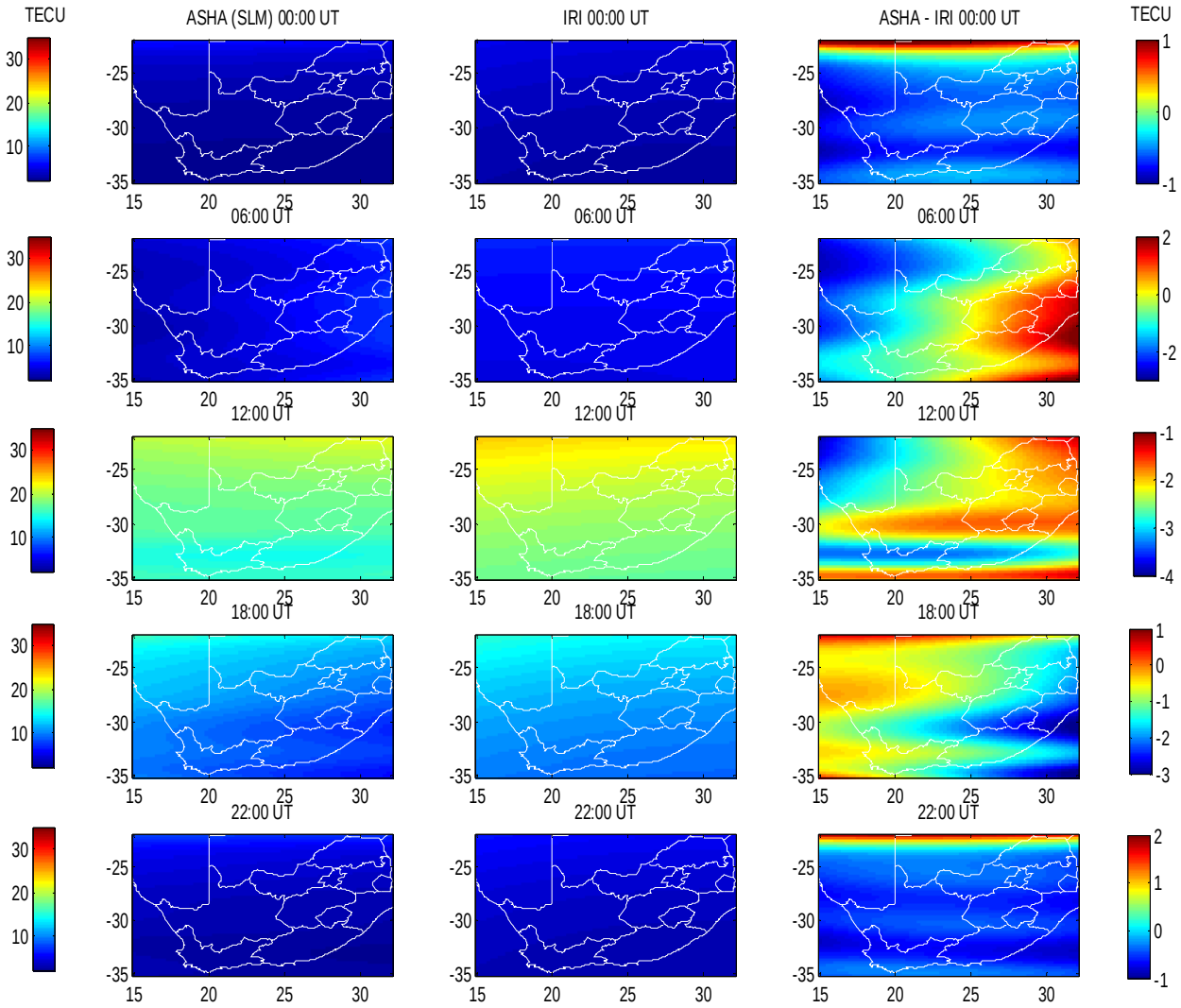

Figure 27. Test case 2B: Comparison of ASHA estimated 2D vertical TEC maps using simulated IRI slant TEC observed by eight receivers and reference 2D vertical IRI TEC maps for 15 March 2006 (day 74). A 12th degree and order harmonic expansion and an 350 km assumed ionospheric shell height were used in the analysis. The 3rd column illustrates the difference between the estimated and reference TEC results.

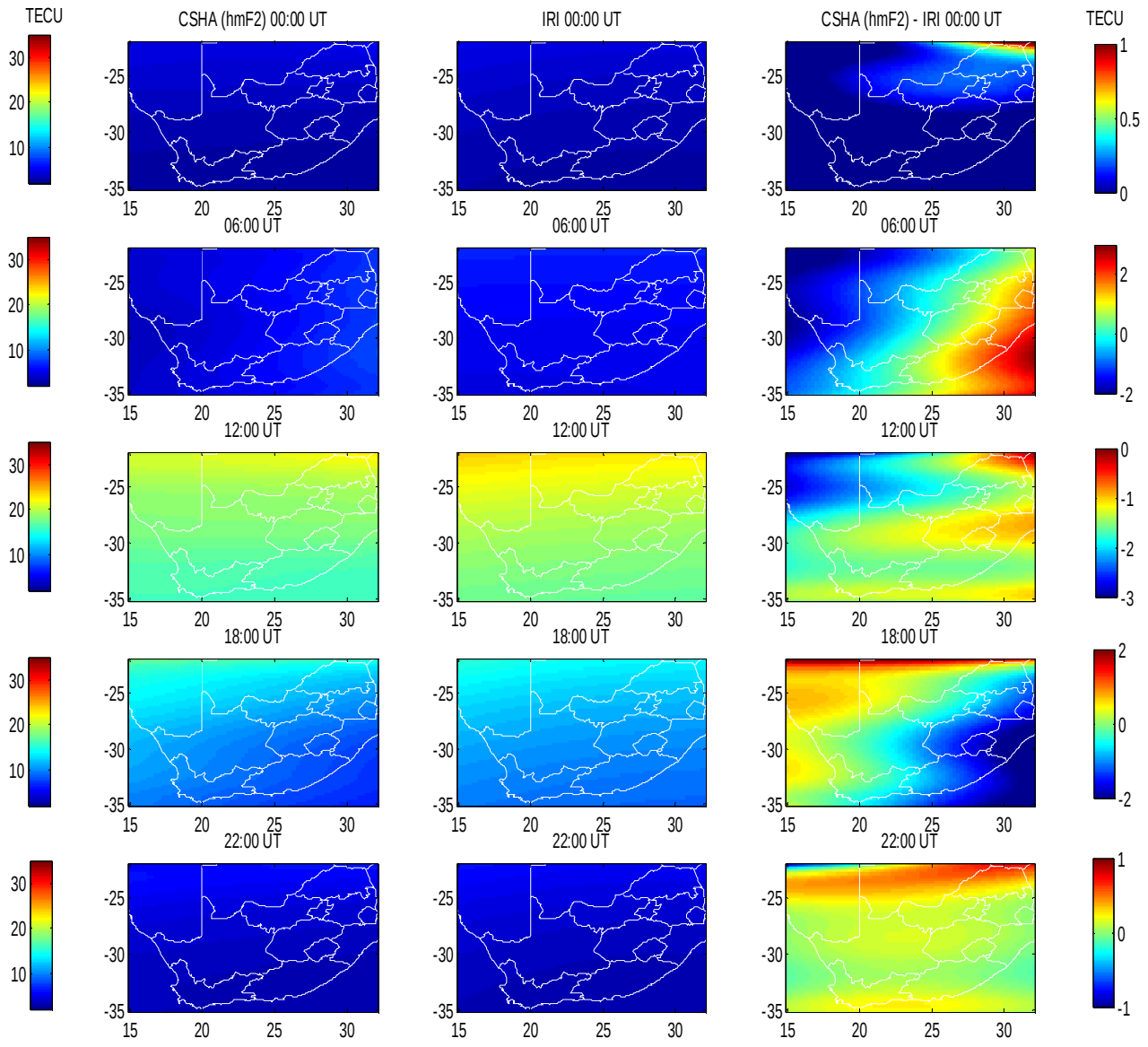

Figure 28. Test case 2C: Comparison of CSHA estimated 2D vertical TEC maps using simulated IRI slant TEC observed by multiple receivers and reference 2D vertical IRI TEC maps for 15 March 2006 (day 74). A 12th degree and order harmonic expansion and an IRI-derived *hmF2* varying thin-shell height were used in the analysis. The 3rd column illustrates the difference between the estimated and reference TEC results.

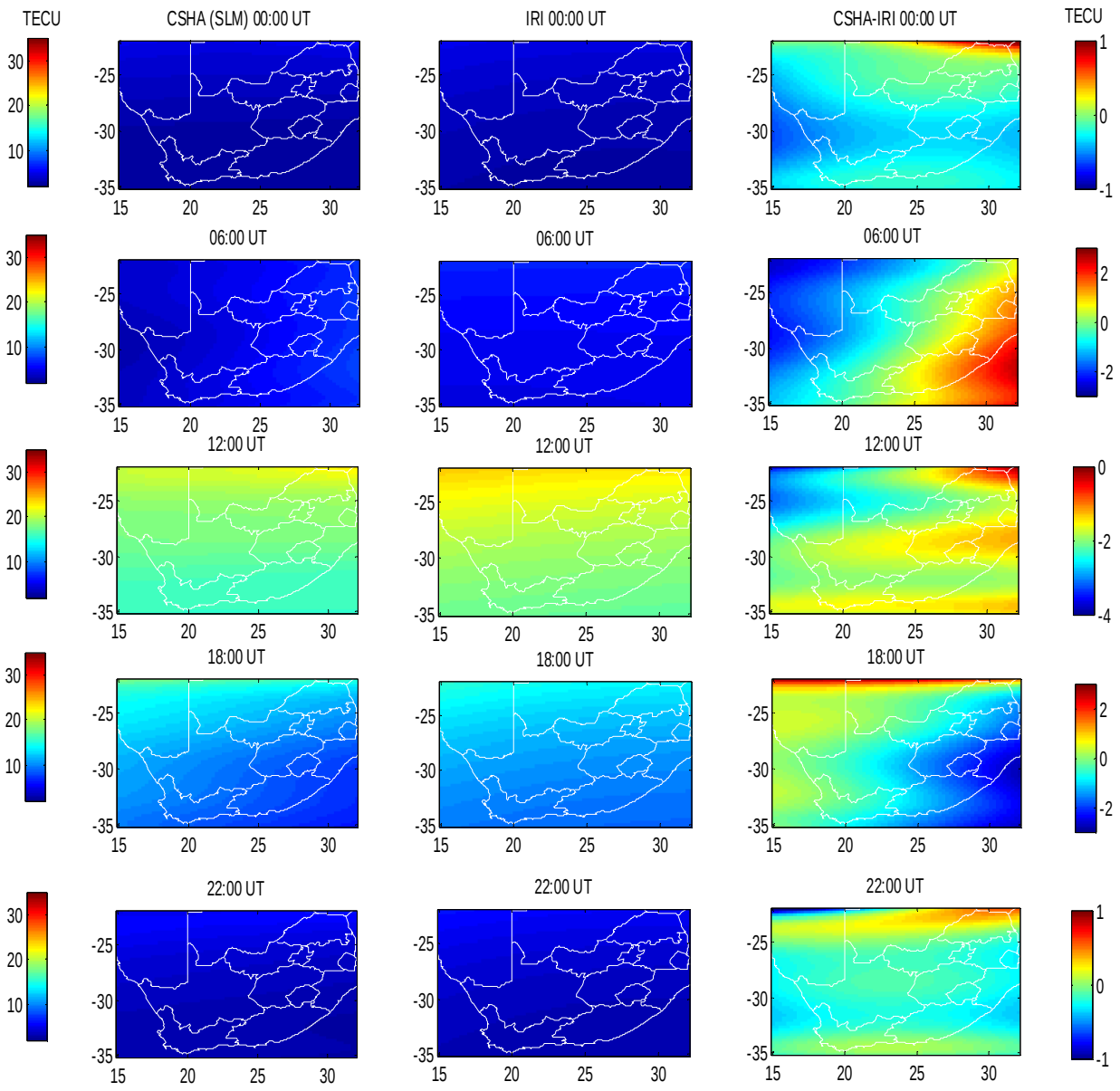

Figure 29. Test case 2D: Comparison of CSHA estimated 2D vertical TEC maps using simulated IRI slant TEC observed by multiple receivers and reference 2D vertical IRI TEC maps for 15 March 2006 (day 74). A 12th degree and order harmonic expansion and a 350 km assumed ionospheric shell height were used in the analysis. The 3rd column illustrates the difference between the estimated and reference TEC results.

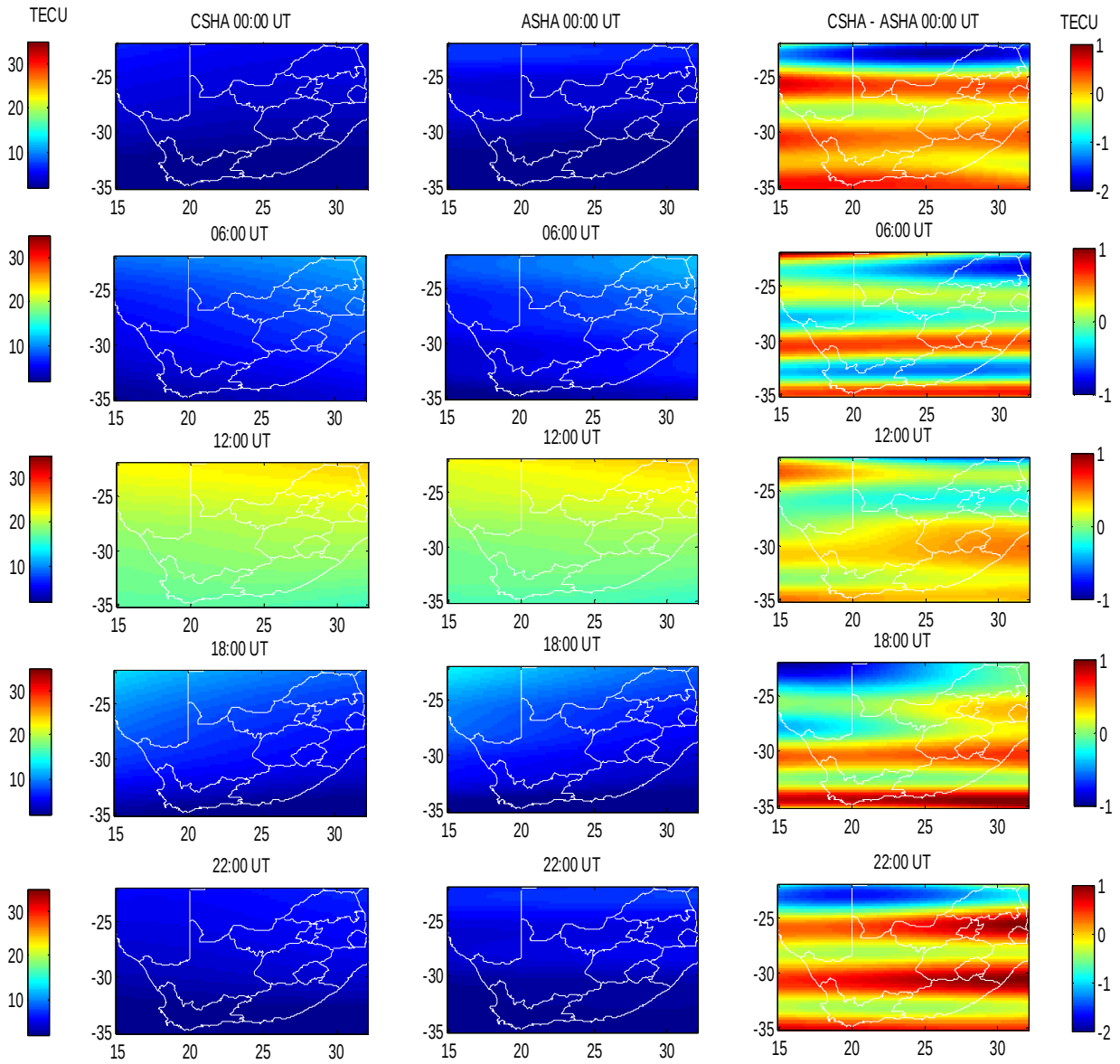

Figure 30. Test case 2E: Comparison of CSHA and ASHA estimated 2D vertical TEC results from actual GPS data from eight receivers (Table 4) on 15 March 2006 (day 74). A 12th degree and order harmonic expansion and (*hmF2*) varying ionospheric shell height were used in the analysis. The horizontal features in the column 2 images are subtracted from column 1 images, rendering the "differenced" images in column 3, attributed to the difference between the terrestrial wavelength and the adjusted terrestrial wavelength of the Legendre functions (See **paragraph 5.2.2.2**).

Table 5. Test case 2A statistics on difference in ASHA (*hmF2*)-IRI 2D TEC maps for 15 March 2006.

Hour	Min TEC	Max TEC	Mean TEC	Stdev	RMS
00:00	-0.6662	1.9131	-0.1003	0.5202	0.5297
06:00	-2.5498	2.6855	-0.3801	1.1393	1.2008
12:00	-3.4377	-0.6296	-1.8770	0.5101	1.9450
18:00	-2.9738	0.9032	-0.8295	0.8087	1.1584
22:00	-0.5602	2.1695	0.0335	0.5444	0.5454

Table 6. Test case 2B statistics on difference in ASHA (SLM)-IRI 2D TEC maps for 15 March 2006.

Hour	Min TEC	Max TEC	Mean TEC	Stdev	RMS
00:00	-0.9197	1.3233	-0.4460	0.3968	0.5969
06:00	-2.7591	2.4209	-0.5657	1.1435	1.2756
12:00	-3.8619	-1.2711	-2.3671	0.5452	2.4290
18:00	-3.1045	0.5796	-1.1332	0.7141	1.3394
22:00	-0.8239	1.8188	-0.3239	0.4694	0.5703

Table 7. Test case 2C statistics on difference in CSHA (*hmF2*)-IRI 2D TEC maps for 15 March 2006.

Hour	Min TEC	Max TEC	Mean TEC	Stdev	RMS
00:00	-0.6299	1.2326	-0.2212	0.2054	0.3019
06:00	-2.6287	2.5871	-0.2952	1.2408	1.2753
12:00	-3.6694	-0.1352	-1.8984	0.4509	1.9512
18:00	-2.7447	2.5428	-0.6214	0.9998	1.1771
22:00	-1.2347	0.5511	-0.1031	0.1825	0.2096

Table 8. Test case 2D statistics on difference in CSHA (SLM)-IRI 2D TEC maps for 15 March 2006

Hour	Min TEC	Max TEC	Mean TEC	Stdev	RMS
00:00	-0.3567	1.2425	0.0003	0.1693	0.1692
06:00	-2.3894	2.8664	-0.0535	1.2465	1.2475
12:00	-3.2289	-0.1285	-1.5658	0.4267	1.6229
18:00	-2.4398	2.3529	-0.3704	0.9642	1.0328
22:00	-0.7197	0.7266	0.1581	0.1617	0.2261

Table 9. Comparison of estimated GPS receiver (Rx) and satellite (PRN) DCBs using ASHA and CSHA options in **Test Cases (TC) 2A-2D.** All DCBs are given in nanoseconds (ns).

Device	Ref DCBs	ASHA (*hmF2*) **TC2A**	Ref – **TC2A**	ASHA (SLM) **TC2B**	Ref – **TC2B**	CSHA (*hmF2*) **TC2C**	Ref – **TC2C**	CSHA (SLM) **TC2D**	Ref – **TC2D**
BFTN Rx	-1.8947	-1.546	-0.3487	-1.467	-0.4277	-1.708	-0.1867	-1.568	-0.3267
DRBN Rx	1.8947	2.344	-0.4493	2.444	-0.5493	2.131	-0.2363	2.274	-0.3793
MBRY Rx	-1.8947	-1.562	-0.3327	-1.473	-0.4217	-1.701	-0.1937	-1.612	-0.2827
MFKG Rx	1.8947	2.142	-0.2473	2.293	-0.3983	1.927	-0.0323	2.057	-0.1623
PELB Rx	-1.8947	-1.566	-0.3287	-1.476	-0.4187	-1.699	-0.1957	-1.608	-0.2867
PRET Rx	1.8947	2.153	-0.2583	2.304	-0.4093	1.938	-0.0433	2.068	-0.1733
SBOK Rx	-1.8947	-1.495	-0.3997	-1.409	-0.4857	-1.662	-0.2327	-1.524	-0.3707
TDOU Rx	1.8947	2.056	-0.1613	2.14	-0.2453	1.833	0.0617	1.932	-0.0373
rms			**0.3270**		**0.4272**		**0.1685**		**0.2756**
PRN#1	-1.3534	-1.017	-0.3364	-0.955	-0.3984	-1.043	-0.3104	-0.986	-0.3674
PRN#2	1.3534	1.142	0.2114	1.154	0.1994	1.14	0.2134	1.149	0.2044
PRN#3	-1.3534	-0.939	-0.4144	-0.903	-0.4504	-0.952	-0.4014	-0.92	-0.4334
PRN#4	1.3534	1.091	0.2624	1.105	0.2484	1.084	0.2694	1.094	0.2594
PRN#5	-1.3534	-1.454	0.1006	-1.381	0.0276	-1.586	0.2326	-1.527	0.1736
PRN#6	1.3534	1.247	0.1064	1.312	0.0414	1.213	0.1404	1.273	0.0804
PRN#7	-1.3534	-1.438	0.0846	-1.374	0.0206	-1.463	0.1096	-1.405	0.0516
PRN#8	1.3534	1.841	-0.4876	1.88	-0.5266	1.591	-0.2376	1.655	-0.3016
PRN#9	-1.3534	-2.057	0.7036	-2.08	0.7266	-1.989	0.6356	-1.978	0.6246
PRN#10	1.3534	1.187	0.1664	1.202	0.1514	1.186	0.1674	1.194	0.1594
PRN#11	-1.3534	-0.652	-0.7014	-0.634	-0.7194	-0.849	-0.5044	-0.826	-0.5274
PRN#13	1.3534	1.621	-0.2676	1.68	-0.3266	1.641	-0.2876	1.696	-0.3426
PRN#14	-1.3534	-0.62	-0.7334	-0.662	-0.6914	-0.84	-0.5134	-0.785	-0.5684
PRN#15	1.3534	0.778	0.5754	0.785	0.5684	0.823	0.5304	0.832	0.5214
PRN#16	-1.3534	-0.976	-0.3774	-0.917	-0.4364	-0.933	-0.4204	-0.885	-0.4684
PRN#17	1.3534	1.178	0.1754	1.196	0.1574	1.196	0.1574	1.206	0.1474
PRN#18	-1.3534	-1.89	0.5366	-1.887	0.5336	-1.915	0.5616	-1.899	0.5456
PRN#19	1.3534	2.279	-0.9256	2.321	-0.9676	2.226	-0.8726	2.273	-0.9196
PRN#20	-1.3534	-0.816	-0.5374	-0.819	-0.5344	-0.922	-0.4314	-0.931	-0.4224
PRN#21	1.3534	0.748	0.6054	0.757	0.5964	0.806	0.5474	0.818	0.5354
PRN#22	-1.3534	-1.165	-0.1884	-1.139	-0.2144	-1.221	-0.1324	-1.192	-0.1614
PRN#23	1.3534	2.171	-0.8176	2.241	-0.8876	2.13	-0.7766	2.188	-0.8346
PRN#24	-1.3534	-1.328	-0.0254	-1.305	-0.0484	-1.386	0.0326	-1.373	0.0196
PRN#25	1.3534	1.617	-0.2636	1.667	-0.3136	1.571	-0.2176	1.619	-0.2656
PRN#26	-1.3534	-1.632	0.2786	-1.611	0.2576	-1.559	0.2056	-1.546	0.1926
PRN#27	1.3534	2.488	-1.1346	2.514	-1.1606	2.271	-0.9176	2.334	-0.9806
PRN#28	-1.3534	-1.201	-0.1524	-1.197	-0.1564	-1.108	-0.2454	-1.074	-0.2794
PRN#29	1.3534	1.134	0.2194	1.154	0.1994	1.198	0.1554	1.209	0.1444
PRN#30	-1.3534	-0.812	-0.5414	-0.748	-0.6054	-1.251	-0.1024	-1.191	-0.1624
rms			**0.4946**		**0.5111**		**0.4252**		**0.4447**

Table 10. Test case 2E. Statistics on difference in CSHA and ASHA estimated 2D GPS TEC maps for 15 March 2006. All values in TECU.

Hour	Min TEC	Max TEC	Mean TEC	Stdev	RMS
00:00	-1.9215	0.7176	-0.1552	0.6348	0.6534
06:00	-0.8148	1.0376	0.0228	0.3722	0.3729
12:00	-0.5478	0.5725	0.1525	0.2121	0.2612
18:00	-0.9420	1.0354	0.1339	0.3980	0.4199
22:00	-1.6181	1.0038	-0.0511	0.6174	0.6194

Table 11. Test case 2E. Estimated DCBs compared to CODE DCBs. All values in nanoseconds.

Rx	CODE	ASHA	SHM
BFTN	na	6.146	6.001
DRBN	na	1.706	1.554
MBRY	na	9.638	9.554
MFKG	na	8.693	8.58
PELB	na	13.742	13.649
PRET	na	10.239	10.16
SBOK	na	6.393	6.218
TDOU	na	6.244	6.105

Sat nr	CODE	ASHA	SHM
PRN#1	-5.708	7.211	7.119
PRN#2	10.7694	-7.005	-7.054
PRN#3	-4.6551	6.067	5.996
PRN#4	-2.4938	4.049	3.956
PRN#5	-4.7659	6.797	6.784
PRN#6	-3.8977	5.024	5.03
PRN#7	-7.4074	7.648	7.659
PRN#8	-5.3201	6.356	6.296
PRN#9	-3.1218	4.437	4.48
PRN#10	-6.9087	6.999	6.971
PRN#11	4.4888	-0.59	-0.655
PRN#12	na	na	na
PRN#13	3.99	-0.404	-0.442
PRN#14	1.4778	1.34	1.249
PRN#15	-6.6685	7.309	7.372
PRN#16	2.032	0.542	0.534
PRN#17	1.9211	0.654	0.56
PRN#18	2.7709	-0.135	-0.181
PRN#19	7.6661	-3.868	-3.96
PRN#20	-1.7549	4.692	4.579
PRN#21	4.5257	-2.012	-1.932
PRN#22	12.0994	-7.627	-7.678
PRN#23	16.0525	-10.969	-11.024
PRN#24	-8.3311	9.035	8.943
PRN#25	-1.4593	2.988	2.871
PRN#26	-2.0504	3.064	3.156
PRN#27	-4.3964	5.389	5.409
PRN#28	2.66	0.529	0.47
PRN#29	-1.5517	2.737	2.837
PRN#30	0.0185	2.548	2.477

5.4.3 Test Case 3: TOPEX/Poseidon (T/P) and Jason-1 (J-1)

T/P and Jason-1 TEC measurements were used as another independent reference source for evaluating the ASHA TEC estimation algorithm. Because T/P and Jason-1 measurements are restricted to open ocean regions, vertical TEC results estimated from an IGS GPS receiver installed on Gough Island (9.88°W, 40.35°S) were used in this study and compared to T/P and Jason-1 TEC measurements taken along orbits passing near-vertically over the GPS receiver. Relevant T/P and Jason-1 data arcs were identified as those sections of orbits passing within 15° of the Gough GPS receiver's zenith. T/P and Jason-1 orbits are ordered in cycles, with each 10-day cycle containing 127 passes and measurements are stored in binary Merged Geophysical Data Records-B (MGDRB) data files available at [PO.DAAC]. An example of selected T/P passes of cycle 461 are presented in **Figure 31** and **Figure 32** and the cycles/passes relevant to this study are listed in Table 12. Diurnal GPS-TEC estimated at Gough close to 2005 equinox and solstice dates are illustrated in **Figure 34**.

Table 12. T/P and Jason-1 orbit footprints intersecting Gough GPS receiver's 40° elevation footprint close to 2005 equinox/solstice dates.

Cycle (TOPEX)	Cycle (Jason-1)	Pass	Date (2005)	Day of year	Time (UTC)
461		48	22 March	81	05:06-05:12
461		109	24 March	83	13:46-13:53
	118	109	24 March	83	13:38-13:51
	118	226	29 March	88	No GPS data
470		48	19 June	170	10:53-10:59
470		109	21 June	172	19:33-19:39
	127	109	21 June	172	19:25-19:37
	127	226	26 June	177	09:28-09:40
480		48	26 September	269	14:38-14:45
480		109	28 September	271	23:19-23:25
	137	109	28 September	271	23:10-23:23
	137	226	03 October	276	13:13-13:25
	145	109	17 December	351	06:59-07:11
	145	226	21 December	355	21:02-21:14

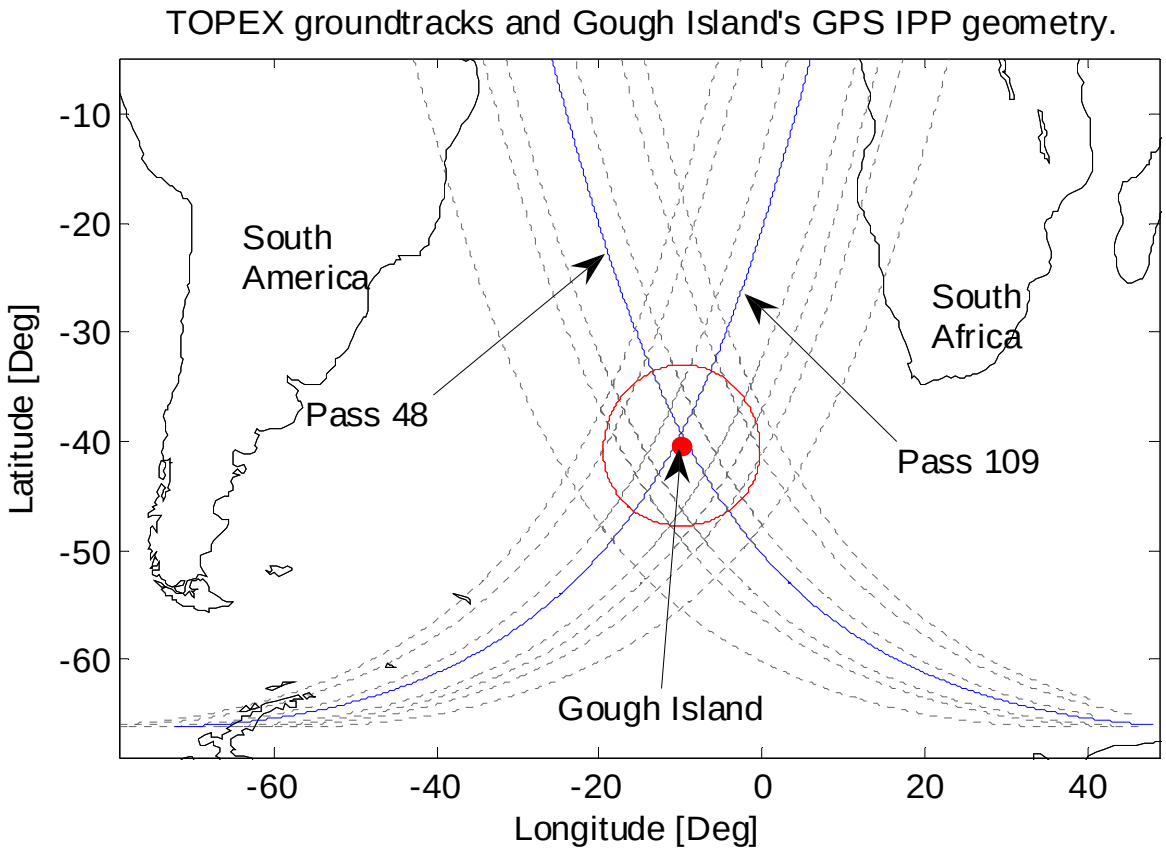

Figure 31. Selected T/P ground tracks for cycle 461, highlighting passes 48 (22 March 2005) and 109 (24 March 2005), passing close to Gough Island zenith. A GPS IPP footprint corresponding to a 40° elevation angle (~800 km) around Gough Island is illustrated. Jason-1 ground tracks are very similar to T/P.

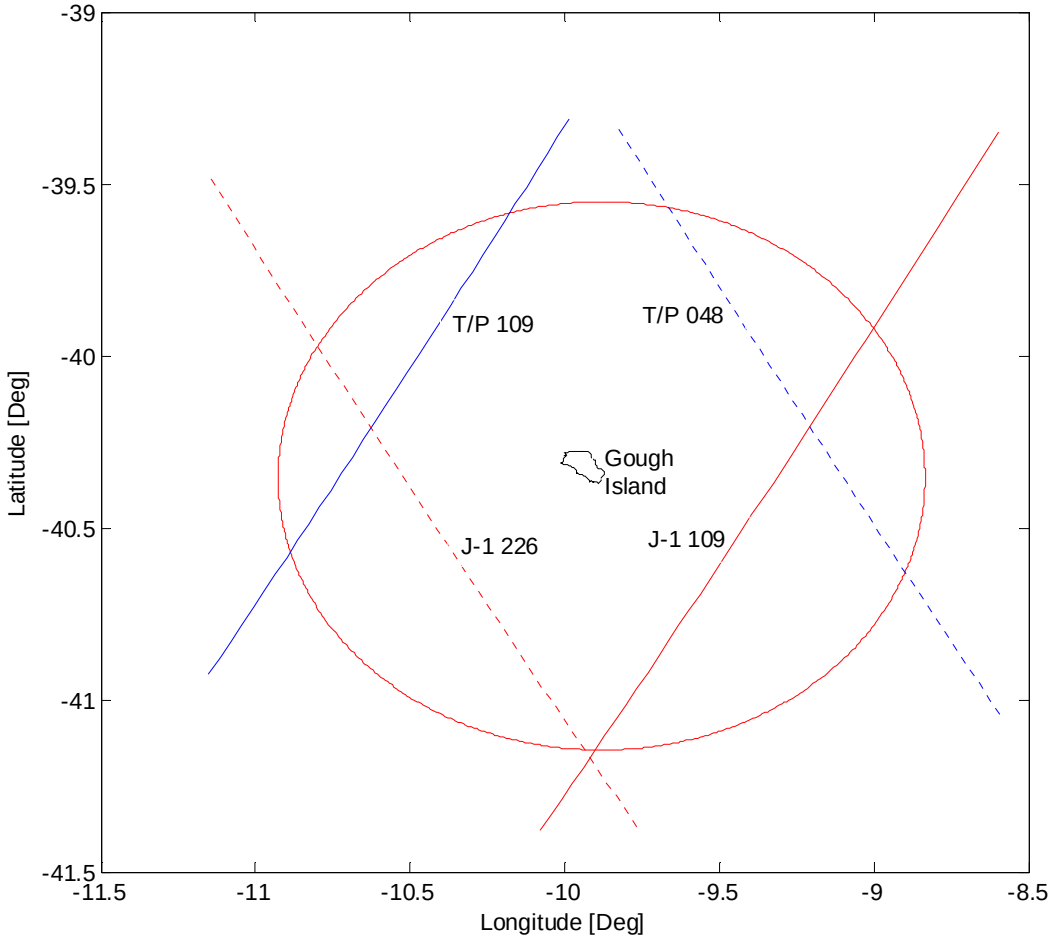

Figure 32. Enlarged view of relevant T/P and J-1 ground tracks (**Table 12**) intersecting the Gough GPS receiver's 15° zenith angle IPP footprint calculated using a 350 km assumed ionospheric shell height.

Data processing involved downloading the relevant MGDRB files, converting them to ASCII format, extracting the time, ground track co-ordinates and the ionospheric delay parameters and calculating TEC along the ground track using Eq. 4.5. The calculated TEC was smoothed using 25 and 35 point windows on measurements respectively taken between 06:00-24:00 and 00:00-06:00. Examples of smoothed T/P and J-1 TEC values over Gough Island close to 2005 equinox and solstice dates are presented in **Figure 33.**

As none of the selected T/P J-1 orbits pass vertically over the receiver on Gough Island, ASHA's capability at consistently estimating TEC at locations distinct from the receiver location had to be evaluated prior to interpolating GPS TEC along the satellites' off-zenith ground footprint. For this purpose, a 15° zenith (75° elevation) angle IPP footprint was defined around the receiver and diurnal vertical TEC was calculated at three distinct locations (P1, P2, P3) on a J-1 ground track intersecting this footprint (**Figure 35**). The comparative diurnal TEC results at these locations are presented in **Figure 36**. The good agreement between the resulting diurnal TEC profiles illustrates the algorithm's capability at estimating TEC away from the receiver, giving confidence to proceed with the T/P and J-1 TEC comparison.

Finally, ASHA-derived GPS TEC values, calculated along T/P and J-1 satellite ground tracks intersecting the 15° zenith footprint, were compared to the corresponding T/P and J-1 TEC measurements. To this end, the intersection times of T/P and Jason-1 ground tracks with the GPS zenith footprint were determined and ASHA coefficients were estimated from 24-hour period RINEX observation files. GPS-TEC was interpolated along the relevant T/P and J-1 ground tracks sections by applying Eq. 5.1 to the estimated ASHA-coefficients, the satellite time measurement and corresponding satellite geographic position. The ASHA-interpolated TEC and T/P and J-1 TEC for these dates are presented respectively in **Figure 37** and **Figure 38**. The effect of using different ionospheric shell heights in estimating GPS-TEC was investigated and the results compared with J-1 TEC close to 2005 equinox and solstice days (**Figure 39**).

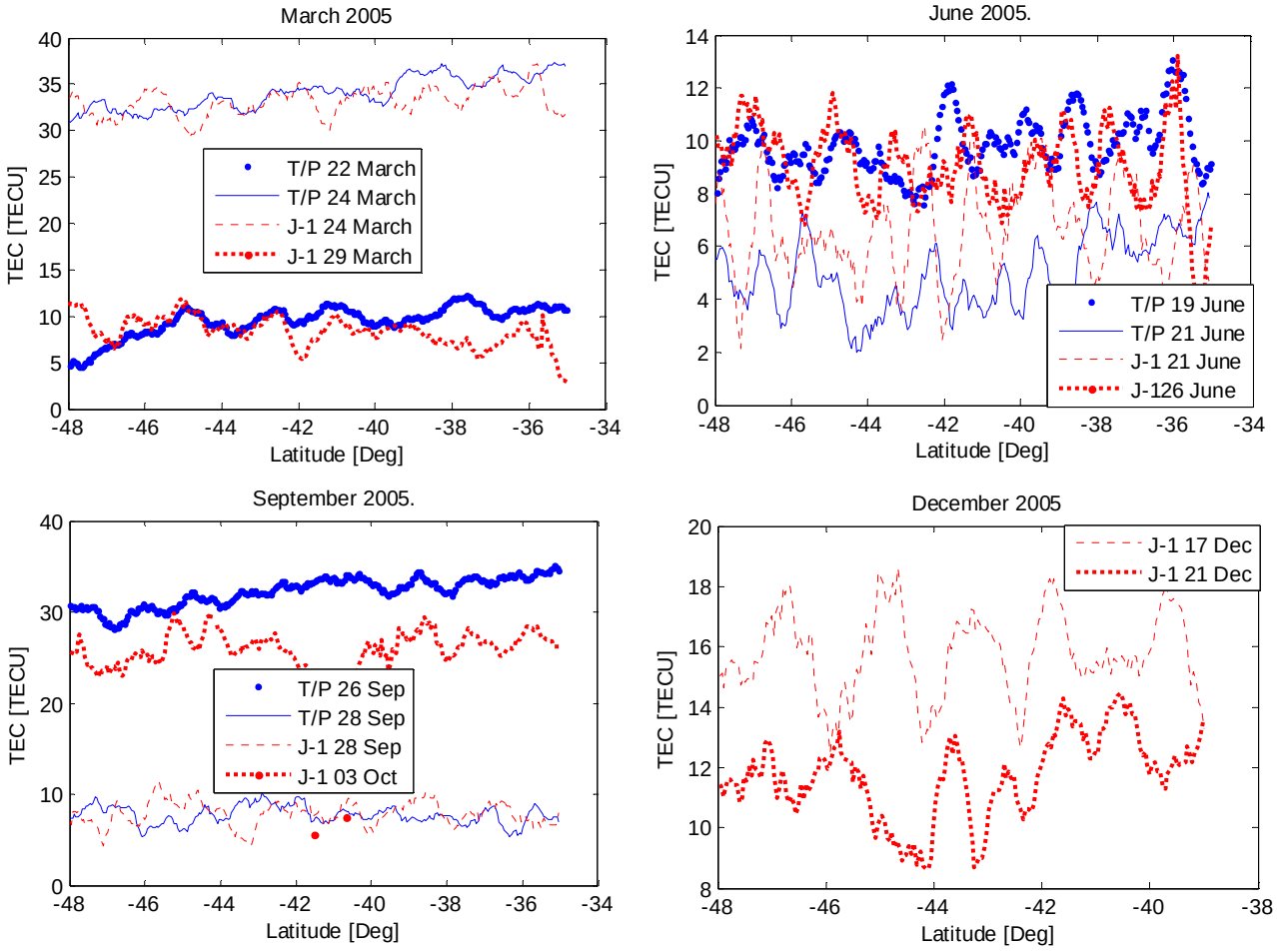

Figure 33. Smoothed T/P and Jason-1 (J-1) TEC calculated along sections of their respective orbits transecting the Gough Island GPS receiver's 40° elevation footprint close to 2005 equinox and solstice dates. No T/P data was available for December. The day-night TEC difference and solstice instability is apparent in the data. See **Table 12** for satellite orbit details.

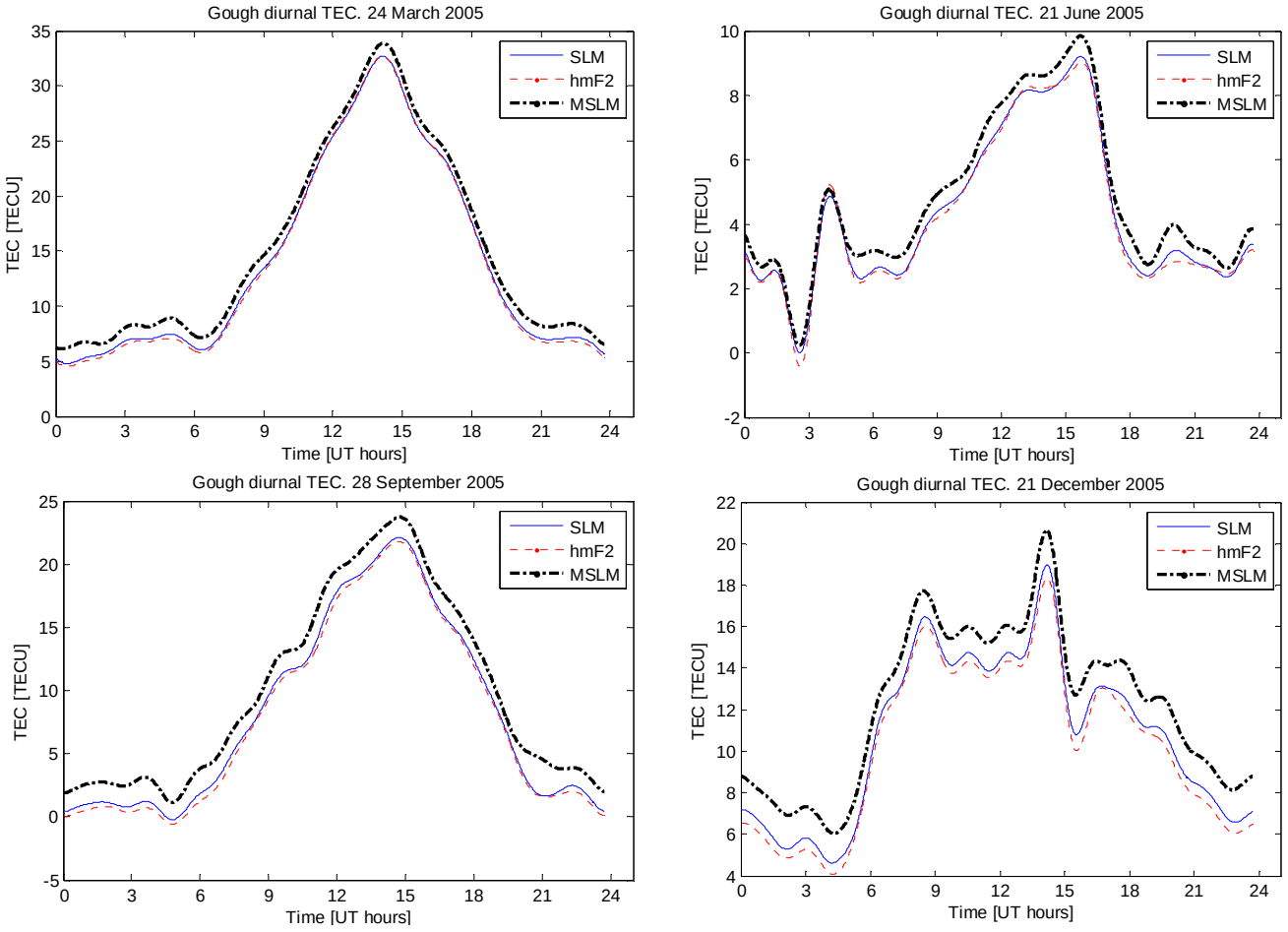

Figure 34. Diurnal GPS-TEC variation close to 2005 equinox and solstice dates at Gough island using the ASHA algorithm with different slant to vertical mapping functions: Fixed shell height Single Layer Model (SLM, 350 km), varying shell height (IRI-derived *hmF2*) and Modified Single Layer Model (MSLM, 570 km shell height). These dates to coincide with the times of T/P and Jason-1 orbits passing near vertical over the island (**Table 12**). Note the low winter TEC values and the high ionospheric variability associated with solstice dates.

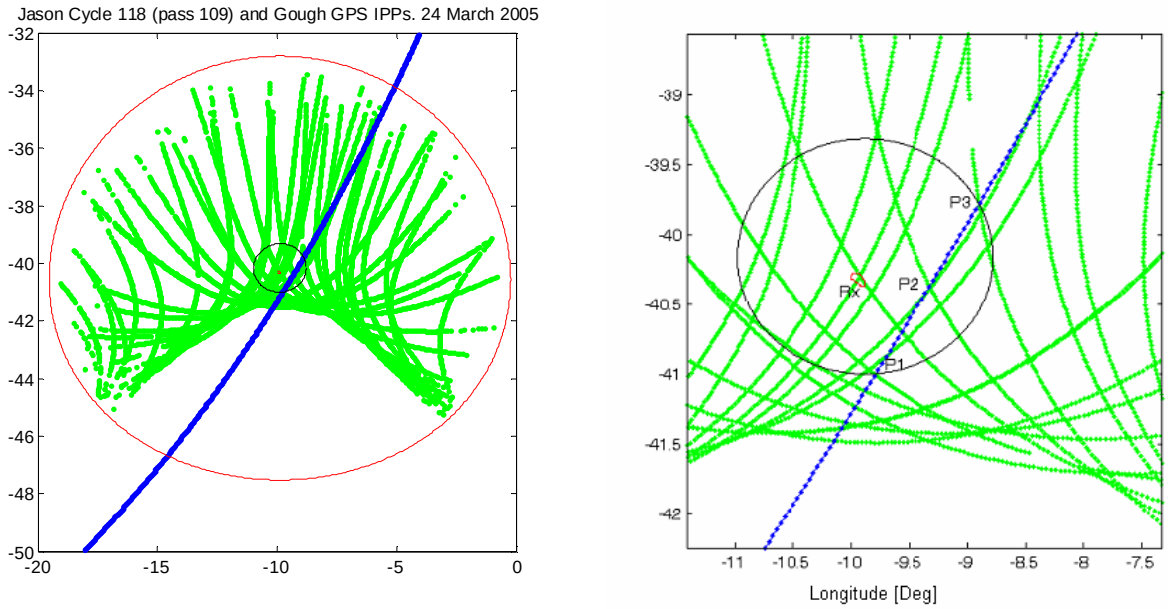

Figure 35. Jason-1 pass 109 (Cycle 118) footprint transecting Gough Island GPS receiver 40° (red) and 75° (black) IPP footprint on 24 March 2005. The enlarged section (right) illustrates the location of three distinct points along the satellite ground track at which ASHA diurnal TEC was calculated to verify it's ability to interpolate within the vicinity of the receiver.

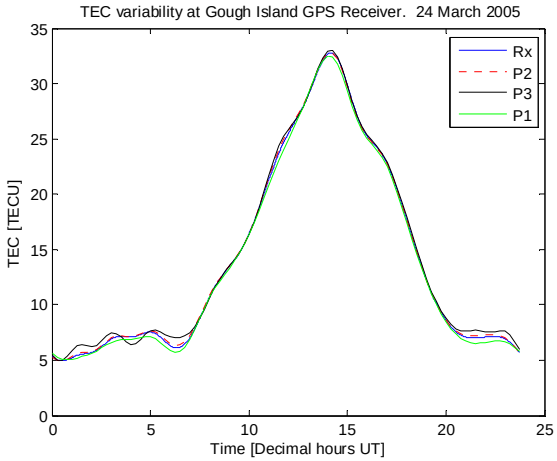

Figure 36. ASHA-derived diurnal TEC variability at four distinct locations on Gough Island illustrated in **Figure 35**.

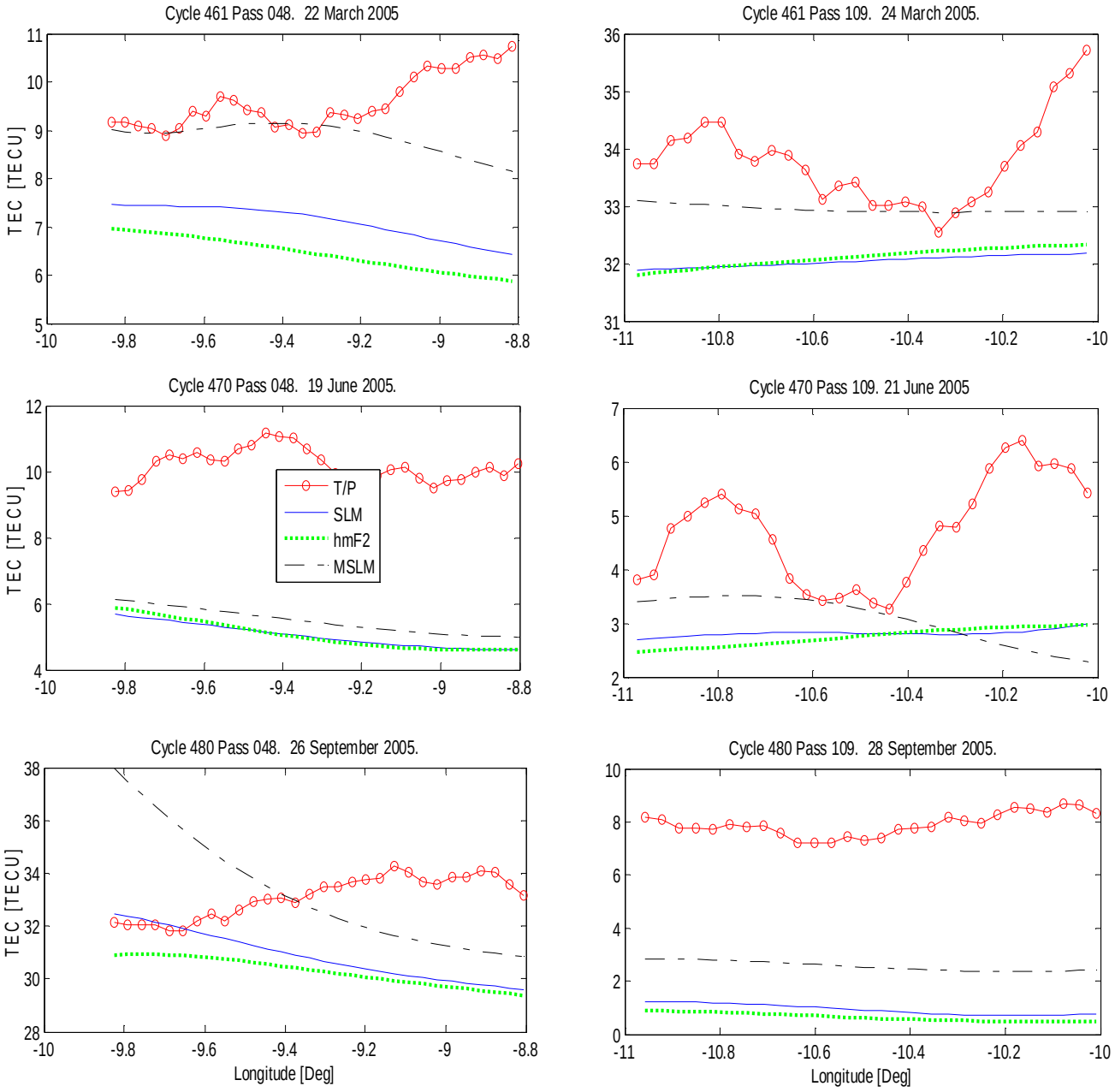

Figure 37. Comparison between T/P and ASHA-derived TEC observed from Gough Island close to 2005 solstice and equinox dates. These results correspond to the satellite transition time through the 15° zenith angle footprint and illustrate the difference in TEC at different times of day. Transition times are listed in **Table 12**. No T/P MGDRB files were available after September 2005.

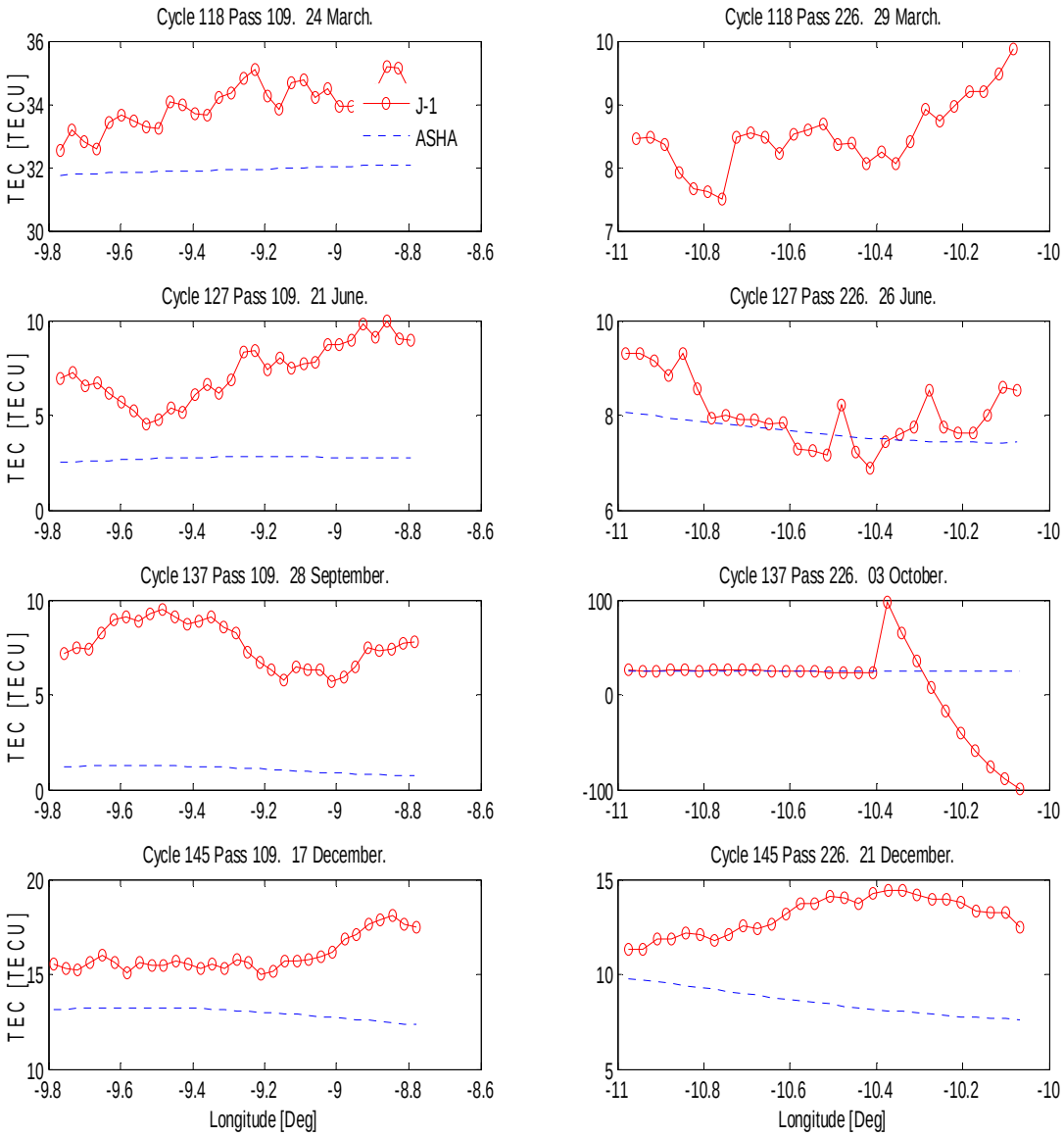

Figure 38. Comparison between Jason-1 (red) and ASHA-derived TEC (blue) observed from Gough Island close to 2005 solstice and equinox dates. These results correspond to the satellite transition time through the 15° zenith angle footprint and illustrate the difference in TEC at different times of day. Transition times are listed in **Table 12**. No GPS data was available for 29 March and Jason-1 TEC for 03 October is suspect.

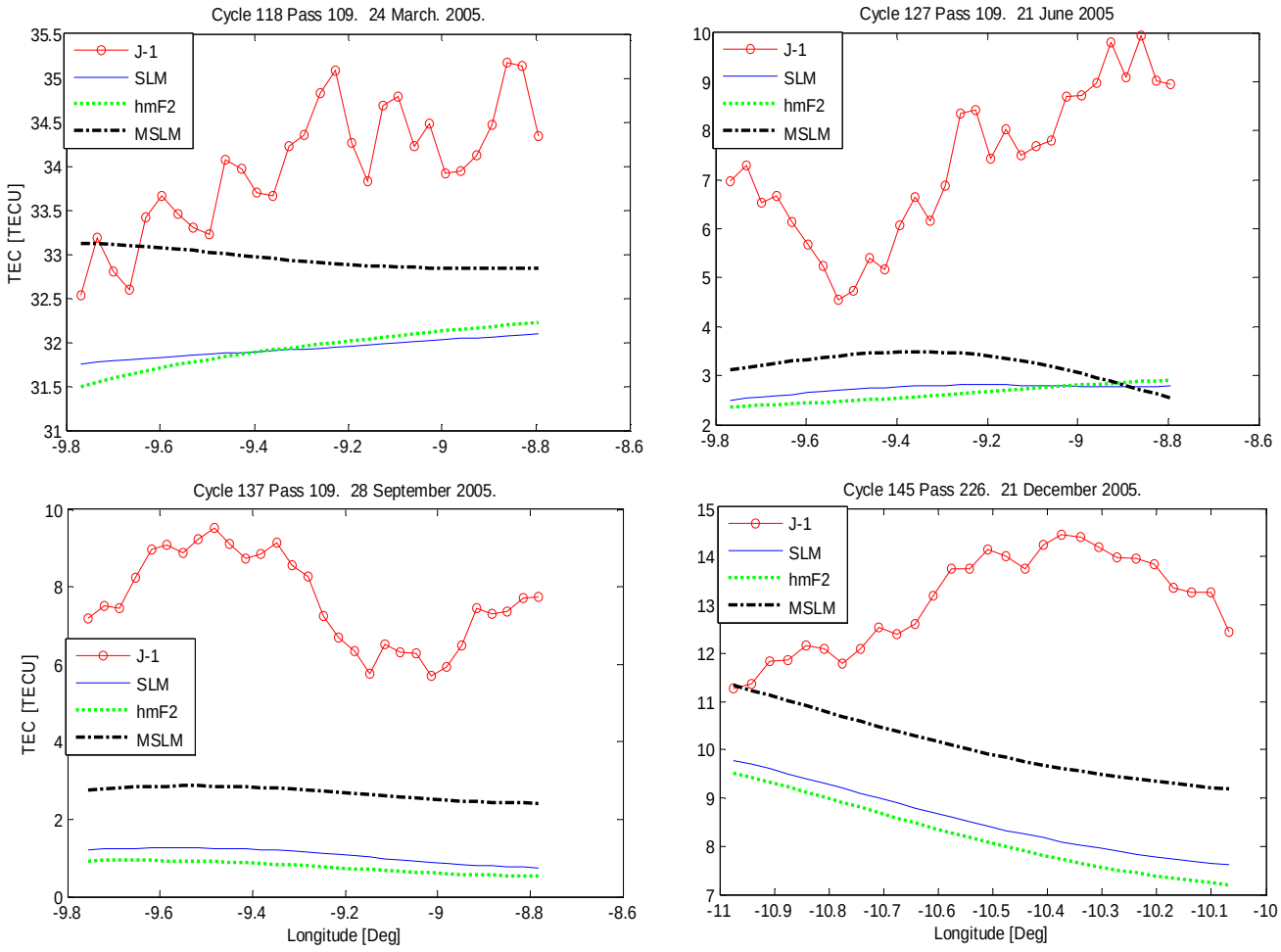

Figure 39. Comparison between Jason-1 and ASHA-derived TEC observed from Gough Island close to 2005 solstice and equinox dates. These results correspond to the satellite transition times through the 15° zenith angle footprint and illustrate the difference in TEC at different times of day and season. The results for three different ionospheric shell models are illustrated: The fixed height (350 km) Single Layer Model (SLM), the variable shell height model (using IRI-derived *hmF2*) and the Modified Single Layer Model (MSLM). Transition times are listed in **Table 12**.

5.5 Discussion

The IRI is a complex data-driven model which was developed using long-term monthly mean values of ionospheric observations from instruments distributed across the globe, *sans* Southern Africa. The IRI reflects our current understanding of the ionosphere but, as with any model, only approximates reality. For the purpose of generating simulation and reference data for software testing and evaluation, the IRI sufficiently describes general diurnal mid-latitude ionospheric behaviour. Given these known model limitations, a qualitative TEC-comparison is discussed for the simulation results. The ASHA-IRI interpolated results (**Figure 20**) follow expected diurnal TEC variations with low nighttime TEC values and midday peaks with no negative TEC values. It appears that the magnitude of TEC derived values using the *hmF2* varying shell height approximated the reference vertical IRI diurnal values slightly better than fixed height SLM. The relatively good comparison between the single receiver ASHA-interpolated profiles and the reference profile, combined with the relatively small difference between the reference and estimated satellite DCBs for the test case, is encouraging and gives an indication of the correct software implementation of the ASHA algorithm. Comparisons of the difference between reference and estimated TEC, receiver DCB and satellite DCB reveal a marginally smaller rms error for CSHA results than for results from the newly introduced ASHA methodology (**Figure 21** and **Table 2**). The rms errors for both methods were less than 0.5 ns for estimated DCBs and better than 0.6 TECU for the estimated TEC.

In all the single receiver test cases, **Test cases 1A-C** (**Figure 23 - Figure 25**), GPS-derived TEC values exceed ionosonde-derived TEC. This is as expected as ionosondes only measure up to the F_2 peak density height (*hmF2* ~ 350 km) and the top side Chapman extrapolation (Reinisch *et al.*, 2004) may contain some uncertainties. A significant component of the TEC difference, however, can be attributed to the plasmaspheric TEC contribution. The plasmasphere extends 1200-35000 km above the Earth's surface and contains charge densities (mostly H^+), which are considerably lower than those of the ionosphere. The large extent of the plasmasphere, however, can produce significant integrated charge column densities (TEC) along signal paths passing through the plasmasphere. The daytime plasmasphere contribution to GPS-TEC is approximately ten percent, but increases to 20-35% at night (Webb, 1997). Plasmaspheric TEC separated from GPS-TEC supplies a novel means of

investigating plasmaspheric charged densities evolution and dynamics (Mazzella, 2002; Belehaki, 2002 and 2003; McKinnell *et al.*, 2007).

Apart from the plasmaspheric TEC offset, the ASHA and MIDAS solutions tracked the diurnal ionosonde TEC profiles consistently with the exception of larger MIDAS nighttime TEC for June and September of **Test case 1A** (Grahamstown), where MIDAS appears to over-estimate the nighttime TEC. This might be attributed to the solstice instability for the June case, but cannot be explained for the September case as yet. The GIM-TEC also followed the general diurnal ionosonde TEC profiles in all the test cases, but because of the standard IGS two-hour resolution, fails to reveal finer detail such as the June and December daytime dynamics, which are clearly illustrated by ASHA and MIDAS. MIDAS and GIM TEC values are generally higher than ASHA. The higher GIM values might be attributed to the higher, fixed assumed ionospheric shell height of 350 km, compared to the variable *hmF2*-height employed by ASHA.

The two-dimensional TEC maps presented in **test cases 2A-D** (**Figure 27** - **Figure 29**) illustrate the difference between ASHA and CSHA estimated TEC maps and reference vertical TEC maps. The maximum differences between the estimated and reference maps appear around 12:00 UT with maximum TEC differences for both methodologies between 3-4 TECU. The statistics in **Table 5**-**Table 8** reveal that the ASHA and IRI difference maps have a slightly higher maximum rms value at midday (2.4 TECU) than the corresponding CSHA midday difference rms value (1.95 TECU). For **test cases 2A-D**, the statistics on the difference between the CSHA estimated and the reference TEC maps point to a slightly better estimation by CSHA than the newly developed ASHA algorithm. This is evident from the marginally smaller rms TEC values (**Table 5** - **Table 8**).

The terrestrial wavelength for a 12-degree CSHA model is 30° and the equivalent, scaled terrestrial wavelength for a 12-degree ASHA model is 6.67° (Eq. 5.3). The apparent horizontal structures in the difference maps between the ASHA and CSHA estimated 2D GPS TEC maps (**Figure 30**) can be attributed to the amplitude difference between the 2/3 terrestrial wavelength (20°/30°) and the 3 scaled wavelengths (20°/6.67°) of the 12-degree Legendre function (see paragraph **5.2.2.2**). The relatively small difference in TEC (rms < 1 TECU) and estimated DCBs is a good indication of the ASHA algorithm's comparability with the CSHA algorithm. The apparent discrepancy between

CODEs satellite DCBs and those estimated by the ASHA and CSHA methods may be attributed to the statistical process by which satellite DCBs are calculated from DCBs estimated from global observations by several institutions using different methodologies, *eg* CODE and JPL.

In the TOPEX/Poseidon and Jason-1 TEC analyses, ASHA-derived TEC consistently appears lower than the satellite-measured TEC. This is contrary to what is expected as the longer GPS signal path (20 200 km) should render a higher TEC value than the T/P or J-1 which orbits at 1 300 km. While T/P TEC has been used extensively for GPS-TEC comparisons (Mannucci *et al.*, 1994; Imel, 1994; Ho *et al.*, 1997; Jee *et al.*, 2004; Ping, 2004), long-term studies of TOPEX/Poseidon TEC have shown that a bias exists in its data (Zhao *et al.*, 2004). The apparent ASHA under-estimation subsequently does not necessarily imply an inferior TEC estimation model. It should also be pointed out that in GPS-TEC studies similar to this research work, the GPS model's ionospheric shell height was adjusted to improve agreement between T/P TEC and GPS-derived TEC (Mannucci *et al.*, 1994). This improved agreement by using a higher shell height is illustrated by the MSLM results in **Figure 39**. By increasing the shell height to 600-800 km, better agreement between GPS-TEC and T/P and J-1 TEC may be achieved. This, however, is not advisable for studies over South Africa, as a bias will be introduced in the model, resulting in over-estimated TEC values. The good agreement of ASHA with MIDAS in these test cases, gives sufficient confidence in the ASHA model to accurately estimate TEC from GPS observations to within expected limits.

5.6 Conclusions

A new methodology was developed and evaluated to estimate ionospheric Total Electron Content from GPS observations over South Africa. Results from this study show favourable comparisons with measured ionosonde data and two independent GPS-based methodologies. Simulation results for two-dimensional TEC maps calculated over the region are promising and the small TEC error between the CSHA and ASHA algorithms indicate the suitability of both algorithms for constructing regional TEC maps from estimated coefficients. The algorithms and software developed in this study supplies the means for observing and investigating ionospheric dynamics over Southern Africa and investigating the constitution of plasmaspheric TEC in the near-Earth region. The developed ASHA methodology is the first of its kind for South Africa and may be adapted for application in other

regions. With code optimising, a near real-time TEC mapping system for South Africa is feasible with either of the presented ASHA or CSHA methodologies.

Chapter 6

Application to the Square Kilometer Array

6.1 Introduction

Astronomical radio signals were discovered by Jansky (Jansky, 1932) and early pioneers in this field included Reber, who first mapped the Milky Way using a home made antenna (Reber, 1949) and Kraus (Kraus, 1986). Since its inception, radio astronomy (RA) has contributed significantly to science, leading to the discovery of pulsars, quasars, neutron stars and the cosmic background emission (CBE) for which the 1978 Nobel prize was awarded to Penzias and Wilson. It also contributed significantly to our understanding of the earth and its near space environment through applications such as space geodesy using Very Long Baseline Interferometery (VLBI). Modern operational RA observatories include the American Very Large Array (VLA), Aricebo, the world's largest single dish at 305 m diameter, the Indian Giant Metrewave Radio Telescope (GMRT), the British MERLIN and Australian Compact Telescope Array (ACTA). Present efforts include the European Low Frequency Array (LOFAR) operating below 300 MHz and the South African Karoo Array Telescope (KAT-7) and meerKAT ("more" KAT, 80 antennas) operating at 1.2 – 2.0 GHz (Horrel, 2007). Though South Africa has been involved in radio astronomy since the 1950s, its single 26-metre telescope at Hartebeesthoek has to date limited research to pulsar search and timing and VLBI.

6.2 Square Kilometre Array

New developments in all fields of astronomy have brought the next generation of astronomers to the brink of probing the origin and evolution of the universe as a whole. To address these questions directly, a new generation of astronomical facilities is needed with a revolutionary new instrument at radio wavelengths playing a critical role. To this end the international radio astronomy community is

proposing the Square Kilometre Array (SKA), which will have a 10^6 m^2 collecting area (International SKA Project Office, 2004).

The proposed SKA receiving area would probably contain several thousand small diameter dishes (large N-small D), or a small number (50-60) of large dishes (large D-small N), with 20% of the dishes contained withing a 1 km diameter core (or hub). The remaining 80% of the dishes will be distributed at remote locations (stations). Each station will have a footprint of between 200-400 m. The initial site suitability study assumed 48 stations for large D-small N and 100 stations for large N-small D configuration. A preliminary proposed South African SKA configuration, including remote stations, is illustrated in **Figure 40**. At the time of this thesis research, South Africa and Australia have been shortlisted to host the SKA with a final decision awaited towards the end of 2008.

6.3 SKA requirements

As part of the site suitability requirements to host the SKA, several suitability criteria such as radio frequency interference (RFI), infrastructure, climate *etc* required investigation and quantification (International SKA Project office, 2004; SKA steering commitee, 2005). Because the ionosphere affects the propagation of, especially, lower frequency radio signals, as will be discussed in following paragraphs, a throrough ionospheric stability study was required to investigate the following aspects:

- Total electron Content (TEC) variation over the SKA facility including diurnal, annual and variation with solar activity
- Ionospheric scintillation (S4 index) at various frequencies and at various times of the year
- Description of large scale phenomena in the ionosphere such as gravity waves, Travelling Ionospheric Disturbances (TIDs) and presence or proximity to the equatorial anomaly.
- The effect of particle precipitation rates in regions falling within the South Atlantic Anomaly (SAA)
- Possible impact of the equatorial electrojet on SKA.

At the time of the site suitability study, this thesis research on developing a South African GPS-based ionospheric TEC model had just commenced and, within the study's short time frame, the conventional spherical harmonic analysis model (Schaer, 1999) was implemented for deriving GPS-

TEC and conducting the ionospheric TEC-related investigation of the site suitability study. The implementation of a GPS-TEC model and subsequent ionospheric GPS-TEC studies were scientific firsts in South Africa and significantly contributed to this research thesis. Selected TEC-related results from the study presented in this chapter subsequently constitute the first South African GPS-TEC observations. The reader is referred to (Opperman *et al*., 2005) for the complete ionospheric stability study which was included in South Africa's official bid to host the SKA (SA SKA, 2005).

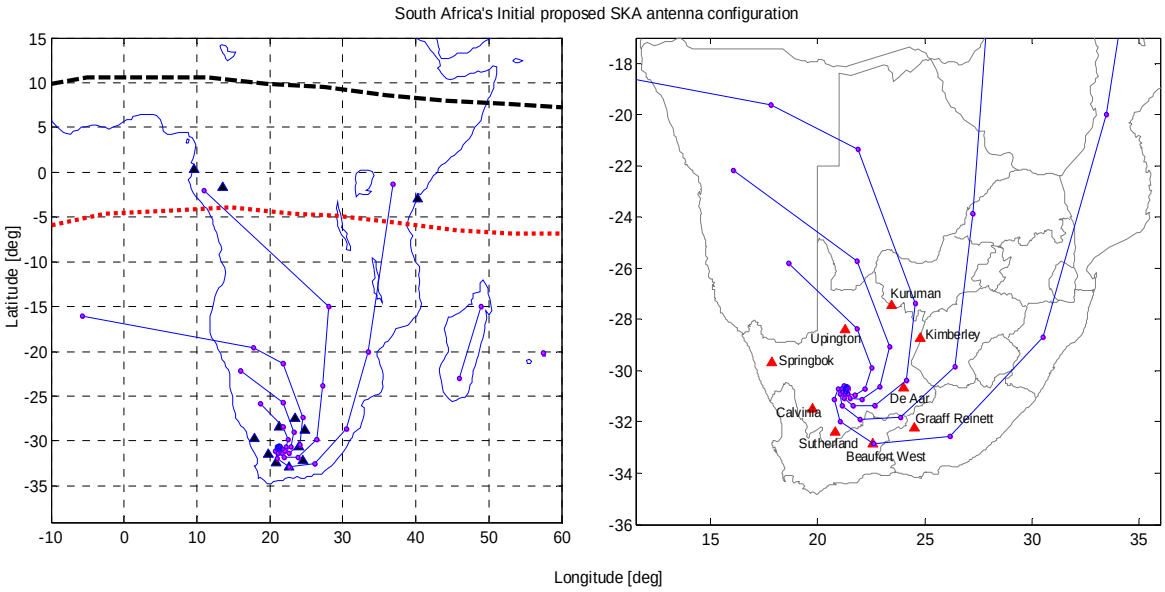

Figure 40. Initial proposed South African SKA logarithmic-spiral antenna configuration used in the site suitability study. The black and red broken lines (left) respectively represent the geomagnetic equator and (southern) equatorial anomaly. The triangles (blue, left and red, right) indicate locations of GPS receivers used in the ionospheric stability study. The core (hub) is located at (21.39°E, 30.71°S).

6.4 Scientific background

6.4.1 Resolution

Because of the large distances involved, it is assumed that an extra-terrestrial radio signal of frequency f and wavelength λ reaches Earth in the form of an oblique planar wave. The angular

resolution, θ in radians, which may be resolved of a radio astronomy source using a telescope of diameter *D* is given by [AIPS++]

$$\theta = \frac{D}{\lambda} \qquad 6.1$$

From Eq. 6.1 it follows that the dish diameter required to observe, *eg* the 21 cm Hydrogen line at an angular resolution of 30", is 1.4 km, which is technically unfeasibile. This resolution, however, is feasible by using the techniques of *interferometry* and *earth rotation synthesis*, by placing two or more antennas 1.4 km apart and integrating the observation over several hours.

6.4.2 Interferometry

The combination of two or more antennas (telescopes) in an array to form a larger receiving antenna the size of their seperation baseline is termed an *interferometer* and it operates on wave interference principle similar to the two-split experiment. Because of the spatial seperation of the individual antennas and the oblique incidence of the radio wave, the wave front reaches antenna 2 before it reaches antenna 1 (**Figure 41**). This is compensated for in hardware by delaying the signal from antenna 2 by the time τ_g, it takes the same wave front to reach antenna 1 (Thompson, 2004). As illustrated in further paragraphs, the ionosphere introduces a frequency-dependent phase shift which needs to be compensated for and is not always a trivial task, especially at long baselines and low frequencies.

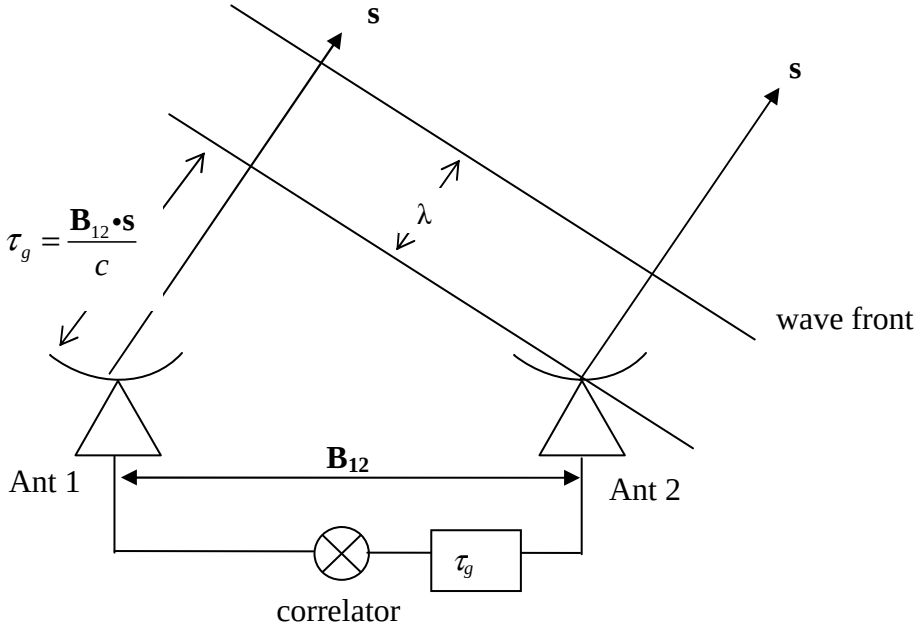

Figure 41. Schematic presentation of a simple two-antenna interferometer. The vector $\mathbf{B_{12}}$ represents the baseline co-ordinates projected on the equatorial plane and **s** represents the pointing vector in the direction of the astronomical the source.

6.4.3 Earth rotation synthesis

The process of earth rotation synthesis renders a projection of each baseline pair on a plane orthogonal to the interferometer's pointing vector. By integrating over time, all baselines pairs will trace a pattern in this *uv* plane, which will serve as the basis for reconstructing the astronomical object in study. For *N* telescopes in a telescope array, there are $N(N\text{-}1)/2$ baselines. Given the East-North-Up co-ordinates of antennas *i* and *j* w.r.t. a known local origin at latitude ϕ, the antenna co-ordinates are transformed to the equatorial plane through Eq. 6.2, (**Figure 42**). The baseline co-ordinates $\mathbf{B}_{ji}$ of each antenna pair *ij* is calculated (Eq. 6.3) and projected onto the *uv* plane using the right ascension and declination values of the pointing vector (Eq. 6.4).

$$\mathbf{x}_i = \begin{bmatrix} x \\ y \\ z \end{bmatrix}_i = \begin{bmatrix} 0 & -\sin\phi & \cos\phi \\ 1 & 0 & 0 \\ 0 & \cos\phi & \sin\phi \end{bmatrix} \begin{bmatrix} E \\ N \\ U \end{bmatrix}_i \qquad 6.2$$

The baseline co-ordinates of each antenna pair, *ij*, is then given by

$$\mathbf{B}_{ji} = \mathbf{x}_j - \mathbf{x}_i \qquad 6.3$$

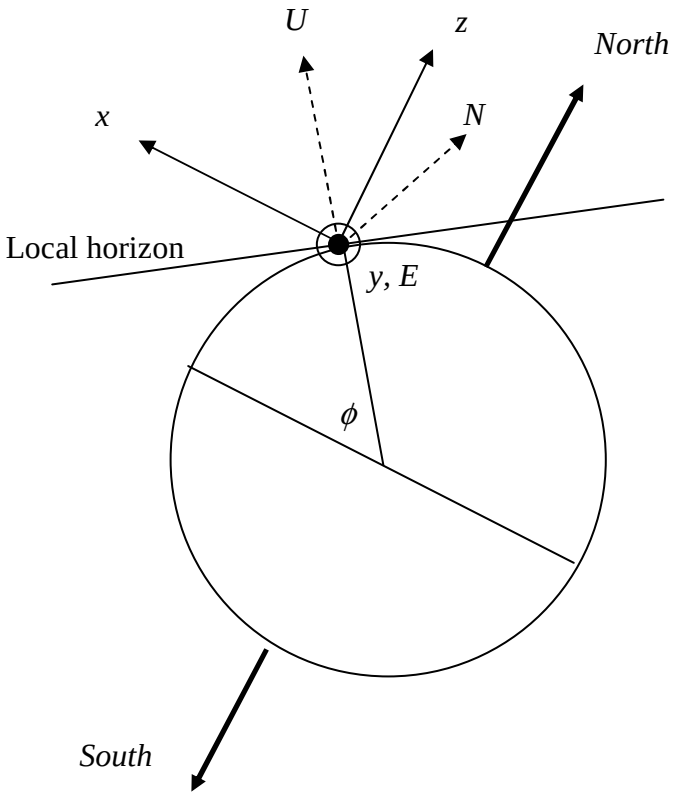

Figure 42. Relationship and geometry of the ENU and equatorial co-ordinate systems.

The (equatorial) baseline co-ordinates are finally transformed to *uvw* co-ordinates which are orthogonal to the interferometer pointing vector.

$$\begin{bmatrix} u \\ v \\ w \end{bmatrix}_{ji} = \frac{1}{\lambda} \cdot \begin{bmatrix} \sin h & \cos h & 0 \\ -\sin\delta \cdot \cos h & \sin\delta \sin h & \cos\delta \\ \cos\delta \cos h & -\cos\delta \sin h & \sin\delta \end{bmatrix} \begin{bmatrix} B_x \\ B_y \\ B_z \end{bmatrix}_{ji} \qquad 6.4$$

where

λ = signal wavelength in metres

δ, h = declination and hour angle of the celestial object under consideration.

The baseline projection in the *uv*-plane is essentially the natural 2D Fourier transformation of the object in consideration, hence the term *complex visibility*, i.e., the interferometer response to the sky intensity distribution of the astronomical object. Ideally the antenna array should constitute a dense gaussian-distributed antenna configuration to facilitate a very dense complex visibility trace when integrating over a period. This, however, is not always feasible because of financial and technical restrictions. An example of the proposed KAT-7 antenna configuration and associated complex visibility is given in **Figure 43**.

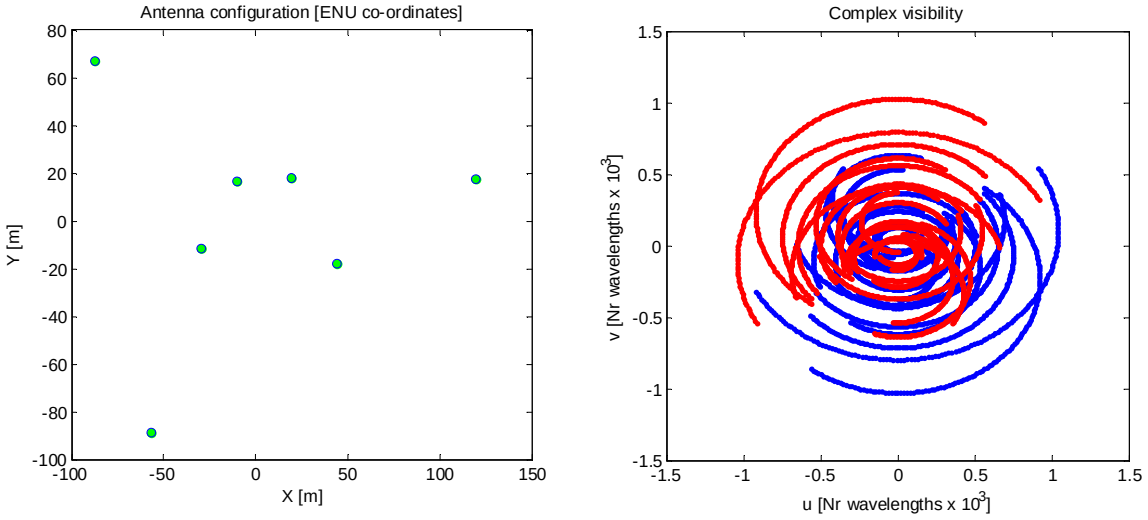

Figure 43. The complex visibility (right), associated with the proposed KAT-7 antenna configuration (left), located at (21.388°E, 30.715°S) is illustrated for a 1.5 GHz signal from a fictitious object located at right ascension-declination [10:00:00, 60:00:00S] for a 12-hour integration period starting 21 March 2005 at 08:00 UT. (Antenna co-ordinates courtesy of Jasper Horrell, KAT manager).

Let the complex visibility obtained through earth rotation synthesis be denoted by $f(u,v)$. The spatial domain image, $F(l,m)$, is then inferred from $f(u,v)$ by the inverse Fourier transform

$$F(l,m) = \iint f(u,v) e^{2\pi(ul+vm)} du dv \,,\; l = u.\lambda,\; m = v.\lambda$$

Due to antenna density restrictions and observation noise, the inferred radio image contains uncertainties and noise which have to be removed through cleaning algorithms and techniques that are beyond the scope of this study. The reader is referred to (Krauss, 1986; Taylor *et al*., 1999; Thompson *et al*., 2004 and Rohlfs *et al*., 2006) for further details.

6.5 Ionospheric influence on radio astronomy

The effect of the ionosphere on radio waves includes phase change, Faraday rotation and ionospheric scintillation. These phenomena are briefly discussed.

6.5.1 Phase change

The refractive index of a cold, neutral plasma is given by (Chen, 1984)

$$n(f) = \sqrt{1 - \frac{f_p^2}{f^2}}$$

where the plasma frequency f_p (re-written from Eq. 2.1) is given by

$$f_p = \sqrt{\frac{N_e e^2}{\pi m_e}} \approx 9\sqrt{N_e} \text{ kHz}$$

Because of the refraction index's f^{-2}-dependence, the propagation of lower frequency waves is affected more by the electron density in the Earth's ionosphere than by high frequency waves. *Eg*, at $f < f_p$, the refractive index becomes imaginary and radio waves do not propagate through the ionosphere. With nominal ionosphere electron densities ~ 10^4–10^5 cm^{-3}, this implies that extra-

terrestrial radio waves in the ~ 1-10 MHz range will not reach the Earth's surface and can only be studied using space telescopes. The ionospheric effect on higher frequencies is illustrated (**Figure 44**) by considering the phase shift expressed in number of wavelength cycles per 1 TEC unit, obtained by dividing the signal path delay in Eq. 3.30 by the wavelength, i.e. $\Delta^{ion}\lambda^{-1}$. For a nominal midday TEC value of 25 TECU, a 1.5 GHz signal, *eg*, will experience a 22 wavelength shift compared to a 336 wavelength shift at 100 MHz.

In the context of an interferometer, the phase shift plays a significant role at low frequencies and large baseline-arrays, such as SKA, which are subject to a non-uniform, time-varying ionosphere. Knowledge of the state of the ionosphere over proposed locations is therefore very important.

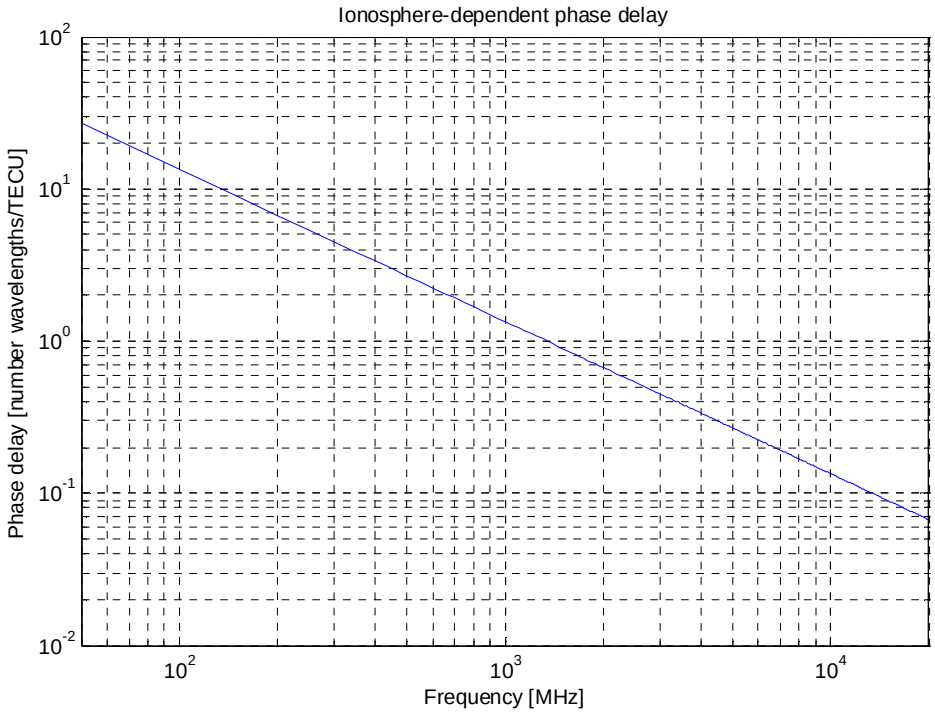

Figure 44. Logarithmic plot of ionosphere-dependent phase shift expressed as the number of wavelengths per 1 TECU in the frequency range 50MHz-20GHz. The phase shift is the largest at lower frequency waves because of the f^{-2}-dependence.

6.5.2 Faraday rotation

If the plasma contains a magnetic field (*B*, in Tesla), the refractive index differs for right and left-handed circular-polarised waves propagating through it and right and left circularly polarised components are phase shifted by different amounts (Chen, 1984). This rotation is called *Faraday rotation* and has significant implication on polarmetric studies of radio astronomy signals. The angle of rotation, Ω (in mks units) for a signal of wavelength λ propagating through the ionosphere at an angle θ to the magnetic field is given by (Kraus, 1986)

$$\Omega = \frac{e^3}{8\pi^2 \varepsilon_0 m_e c^3} \lambda^2 \int_0^d N_e B \cos\theta ds$$
$$= 2.62 \times 10^{-13} \lambda^2 \int_0^d N_e B \cos\theta ds$$

By definition, the integral over the electron density distribution along the signal path constitutes the total electron content and could be substituted as such

$$\Omega = 2.62 \times 10^{-13} \lambda^2 \cdot TEC \cdot B \cos\theta$$
$$= \mathrm{RM} \cdot \lambda^2$$

RM represents the *rotation measure* expressed in radians.m^{-2}. For an assumed B value of 2.3x10^{-5} T at 400 km altitude and nominal TEC value of 25 TECU, the RM will be ~1.5

6.5.3 Ionospheric scintillation

Scintillation is caused by rapid short period variations of small scale ionospheric irregularities causing a change in the observed radio signal's amplitude and phase. Scintillation is more pronounced at frequencies < 1.5 GHz and is more prevelant at very high and very low latitudes. The standard index for measuring ionospheric scintillation is the S4 index which is derived from the normalised standard deviation of the rate of change of TEC (Du *et al*., 2000).

6.6 Methodology

The conventional spherical harmonic analysis model was used to calculate ionospheric TEC at the centre of the proposed SKA hub in South Africa (21.39°E, 30.71°S) using historic (2000-2004) GPS measurements from the nearest nine dual-frequency GPS receivers in the CDSM network and one IGS receiver operated by the Hartebeesthoek Radio Astronomy Observatory (HartRAO). TEC was also calculated at remote stations indicated in **Figure 40** using IGS GPS receivers in close proximity, where available, or at similar latitudes in the absence of GPS receivers in proximity of the proposed SKA antenna location. All available IGS GPS for remote stations were downloaded *via* ftp using automated scripting in MATLAB®. To improve processing speed, all GPS RINEX observation files were decimated to 60-second intervals prior to processing. Significant time was spent removing post processing splicing comments from several IGS receivers' RINEX observation files. RINEX navigation files were initially used for satellite position calculation, but as these weren't available for several remote IGS GPS receivers, post-processed sp3 files, containing precise satellite positions in ECEF co-ordinates at 15-minute intervals, were obtained from [SOPAC]. The processing was conducted on fifteen P4 personal computers (3.2 GHz CPU, 1 GB RAM) at the HMO in Hermanus. The resultant diurnal TEC profiles were subsequently processed further to represent the ionospheric TEC results in the format required by (International SKA Project office, 2004; SSC, 2005).

6.7 Results

Only selected GPS-TEC results from the ionospheric stability study that were obtained using the CSHA model applied to the proposed South African SKA hub and Zambia are presented. Similar GPS-TEC results for the remote locations, as well as other non-TEC ionospheric results can be found (Opperman *et al*., 2005). Results illustrating the diurnal, seasonal and solar cycle TEC variation at the proposed SKA hub are presented in **Figure 45** with mean monthly TEC variation illustrated in **Figure 46**. Similar TEC and TEC variation for Zambia are illustrated in **Figure 47** and **Figure 48.** The correlation between ionosonde-measured foF2 and GPS-derived TEC is illustrated in **Figure 49**.

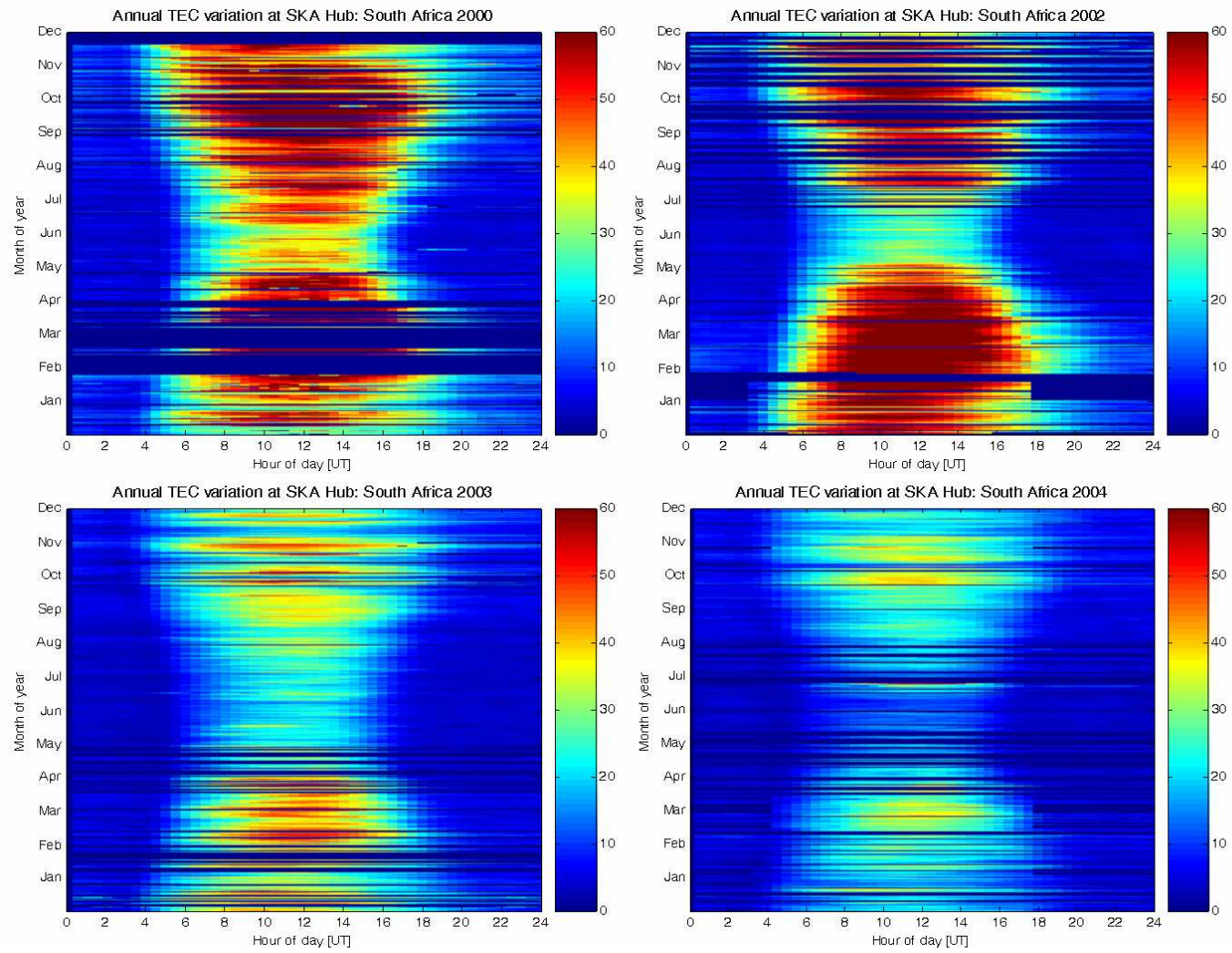

Figure 45. Diurnal (time of day), seasonal (time of year) variation of ionospheric TEC at the proposed SKA hub in TECU for 2000 and 2002-2004. The solar cycle variation is evident in the progressively decreasing TEC values at solar maximum (2000) to solar minimum (2004).

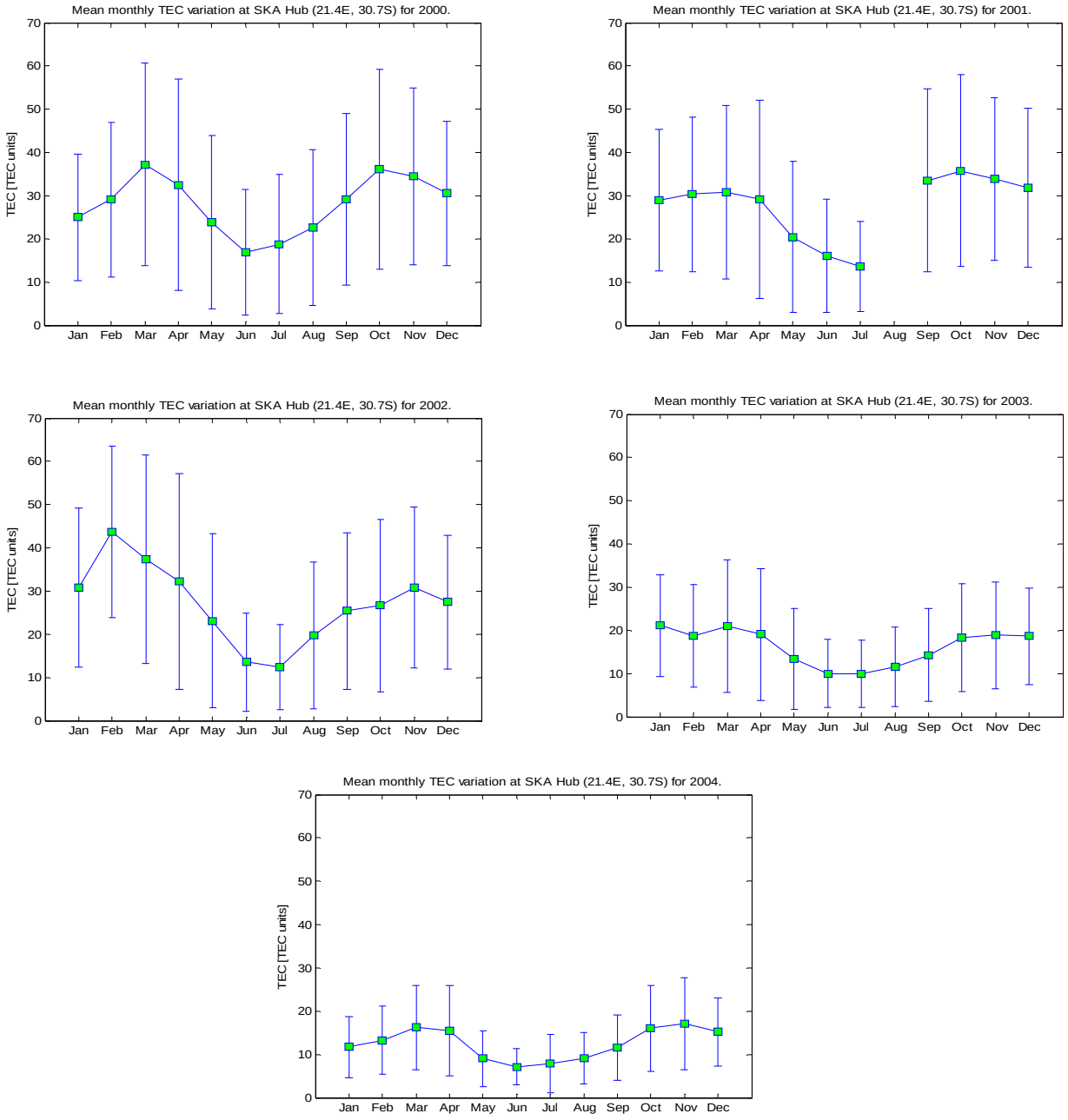

Figure 46. Mean monthly TEC variation for SKA hub with error bars showing 1 standard deviation for 2000-2004 . Note the decrease in the mean TEC values with the decline in the solar activity from 2000 to 2004.

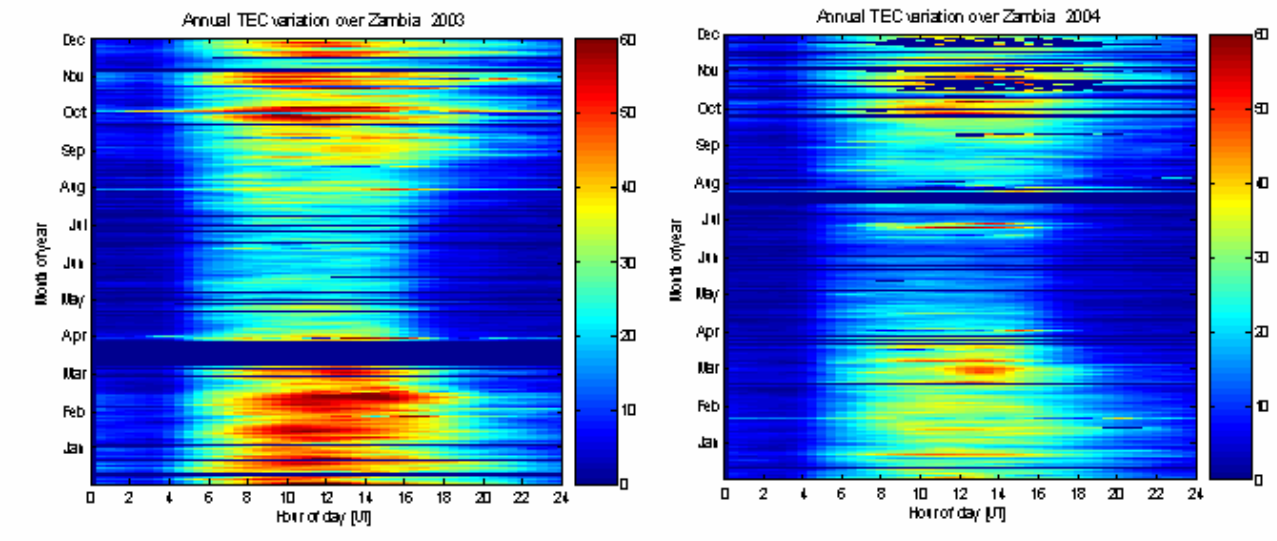

Figure 47. Diurnal (time of day), seasonal (time of year) variation of ionospheric TEC at the Zambian GPS receiver (28.31°E, 15.32°S) for 2003-2004. Measurements are in TECU.

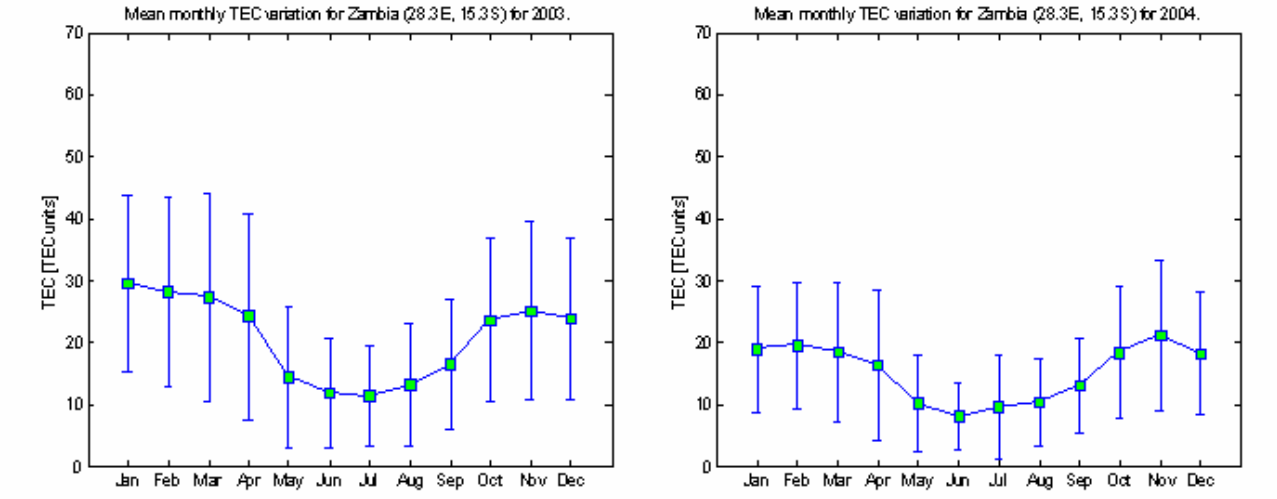

Figure 48. . Mean monthly TEC variation with for Zambia with error bars showing 1 standard deviation for 2003-2004 . Note the decrease in the mean TEC values with the decline in the solar activity from 2003 to 2004

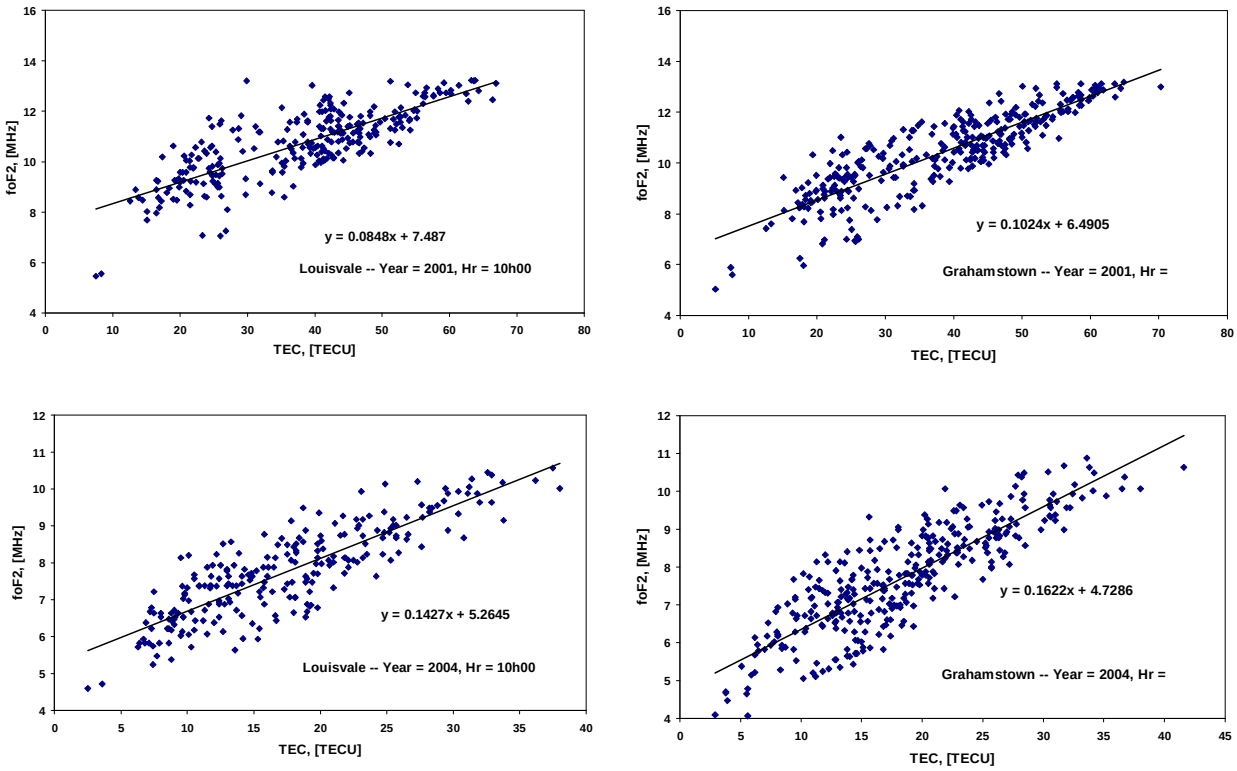

Figure 49. The correlation between ionosonde-measured foF2 and GPS-derived TEC for the years 2001 (top panel) and 2004 (bottom panel), and for Louisvale (left panel) and Grahamstown (right panel).

6.8 Conclusions

The seasonal, diurnal and solar cycle TEC variation at the proposed South African SKA hub appear to follow expected trends of the mid-latitude ionosphere. The linear foF2-TEC correlation illustrates the potential use of GPS-derived TEC as an approximation of the critical frequency of the F2-layer in the absence of ionosonde measurements. The stability study concluded that South African ionospheric conditions were sufficiently stable for radio astronomy observations in the frequency spectrum of the proposed Square Kilometre Array.

Chapter 7

Response of the ionosphere to a severe geomagnetic storm in November 2004

7.1 Scope

This chapter reports on the relevance of adverse space weather to society and the importance of investigating African mid-latitude ionospheric dynamics. After presenting necessary concepts for understanding the solar-terrestrial environment, the development of the November 2004 geomagnetic storm is discussed, followed by an investigation into the associated ionospheric response by using African-based GPS receivers and ground-based magnetometers.

7.2 Introduction

Technology-dependent society has become increasingly vulnerable to adverse space weather as demonstrated *eg*, by power failures due to geomagneticly induced currents in powerlines and the integrity compromising of safety-of-life (SoL) devices such as communication systems and GPS-dependent aircraft navigation and landing systems; calling for an improved understanding of the ionosphere to support the development and improvements of accurate forecasts. To a large extent, the study of geomagnetic storms in mid-latitudes has been neglected for the study of polar and equatorial effects (Kintner *et al.*, 2007). Advances in ionospheric imaging techniques using ground-based GPS receiver networks, however, have revealed that the most extreme examples of ionospheric volume in the form of TEC occur at mid-latitudes during geomagnetic storms where TEC can change by factors of 3-10 (Tsuratani *et al.*, 2005) and TEC values in excess of 300 TECU have been observed in the South Pacific (Mannucci *et al.*, 2005). GPS has subsequently been proven an indispensible instrument for investigating ionospheric dynamics.

Recently observed sharp gradients in storm-induced ionospheric TEC, extending thousands of kilometres over North America **(Figure 50**), are created by unknown factors (Foster and Rideout, 2005) and have lead scientists to theorise that their origin might be be in the African equatorial region (Fuller-Rowell, 2007). To facilitate higher density ionospheric observations on the continent, endevours are underway by a consortium constituting NASA, NOAA, NSF, EOARD (European Office for Aerospace Research and Development), ICTP (International Centre for Theoretical Physics) and others to densify GPS receiver networks on the African continent.

By describing the development of the November 2004 geomagnetic storm and investigating the associated ionospheric response by using African-based GPS receivers and ground-based magnetometers, this chapter serves as demonstrating a practical application of the developed ASHA model in the hope it will lead to further research in this field.

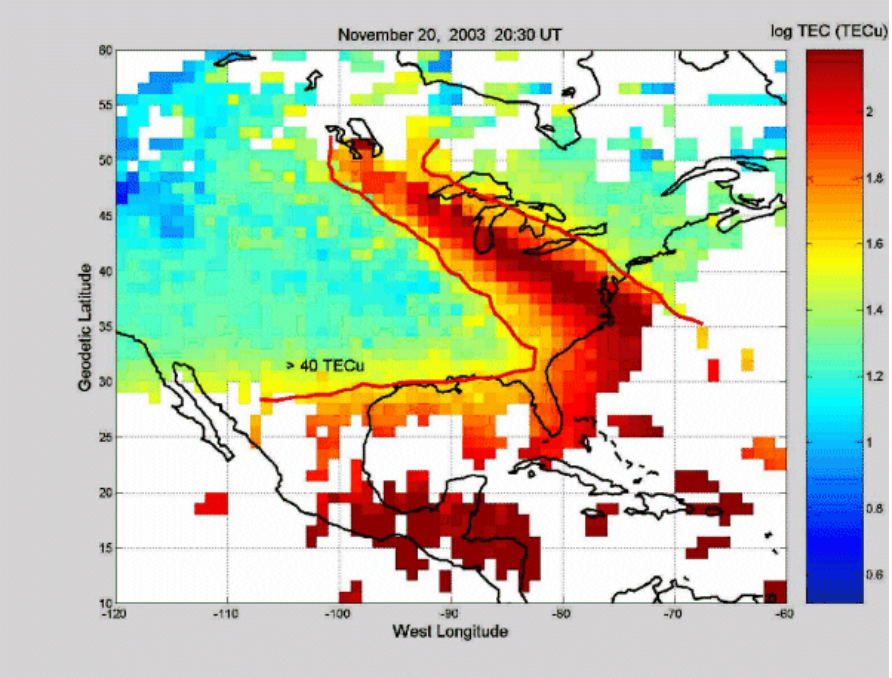

Figure 50 A plume of excess electron density over the USA, 20 November 2003. Image courtesy of Andrea Coster and John Foster, MIT.

7.3 Necessary concepts

A few concepts are presented to facilitate understanding of geomagnetic storms.

7.3.1 Coronal Mass Ejection

A Coronal Mass Ejection (CME) is a large-scale disturbance propagating from the Sun's outer corona into the solar wind and is associated with solar flares. An optical flare such as a CME may be accompanied by X-ray, EUV and radio bursts. The importance of a X-ray flare peak is indicated by a class number with each class assigned according to the flux (E) measured in the 0.1-0.8 nm range by the Geostationary Operational Environmental Satellite (GOES). The major class definitions are

- C-class: $10^{-6} < E < 10^{-5}$ W.m^{-2},
- M-class: $10^{-5} < E < 10^{-4}$ W.m^{-2},
- X-class: $E > 10^{-4}$ W.m^{-2}.

An additional digit added to the class number indicates the flux coefficient, *eg* M5 = $5x10^{-5}$ (Davies, 1989).

7.3.2 Sun's magnetic field and solar wind

The Sun's magnetic field, the Interplanetary Magnetic Field (IMF), extends from the Sun to the outer solar system. The IMF is embedded in the heavier, positively charged ions which, along with other charged particles, constitute the *solar wind* which propagates fom the Sun at a nominal speed of 300-400 km.s^{-1}. During perturbed solar conditions such as CMEs, the solar wind speed increases to more than 1000 km.s^{-1}.

7.3.3 Ring current

Electrically charged particles trapped in the Earth's magnetic field experience an equatorial drift motion resulting in a westward-flowing ring current in the equatorial plane (Baumjohann and Treumann, 1999). The ring current's associated magnetic field constitues about 5% of the measureable geomagnetic field and is sensitive to magnetospheric disturbances. Major perturbations

in the magnetospheric plasma are subsequently observed as changes in the geomagnetic field monitored by terrestrial magnetometers.

7.3.4 Disturbance storm time index

The disturbance storm-time index (Dst), measured in nano tesla (nT), is an index of magnetic activity. The Dst is derived from a network of near-equatorial geomagnetic observatories that measure the intensity of the globally symmetrical equatorial ring current. These observatories are located at San Juan (Puerto Rico), Honolulu (Hawaii), Hermanus (South Africa) and Kakioka (Japan).

7.3.5 Relevant satellite measurements

Data from the following satellites are used in investigating the effects of solar flares and CMEs:

- The Geostationary Operational Environmental Satellite (GOES) orbits Earth at 36 000 km and measures EM radiation associated with solar flares and CMEs. EM radiation travelling at the speed of light reaches Earth eight minutes after the event and is a first quantifying indicator of the event magnitude.
- The Solar and Heliospherical Observatory (SOHO) is located at the L1-libration point, a point on the Sun-Earth gravity vector where the Sun and Earth's gravitational attraction is in equilibrium. The L1-libration point is located approximately 1.5×10^6 km from Earth and 148.5×10^6 km from the Sun. SOHO images the Sun's coronna in several EM frequencies including X-ray and UV and gives the first visual indication of solar flares and CMEs.
- The Advanced Composition Explorer (ACE) satellite orbits around the L1-libration point. ACE measures the velocity, particle composition and strength and orientation of the IMF embedded in the solar wind.

7.3.6 General dynamics of a geomagnetic storm.

Earth-directed CMEs travelling with velocities of about 1000 $km.s^{-1}$, give rise to shock-waves in the solar wind which reaches Earth 24-36 hours after the CME event. The shockwave interaction with the Earth's magnetosphere compresses it and increases the eastward-flowing magnetopause current, resulting in an increase of a few tens of nano teslas (nT) in the geomagnetic Horizontal (H)

component observed at low-latitude ground-based magnetometers. This H-component increase typically lasts some tens of minutes. The onset of the shockwave-magnetosphere interaction is called a Sudden Storm Commencement (SSC) and signifies the *initial phase* of a geomagnetic storm. If the IMF's z-component is orientated southwards, it couples strongly with the Earth's day-side magnetic field, causing magnetic reconnection of the day-side magnetopause, rapidly injecting magnetic and particle energy into the magnetosphere from the magnetotail and creates a storm ring current, an increased westward-flowing ring current which initiates a decrease in the H-component. The *main phase* commences when the H-component decreases below its prestorm value and ends when the H-component reaches a minimum. The main phase may be characterised by substorms, a series of events in the magnetosphere in which energy is suddenly dissipated in association with auroral breakup. This explosive dissipation represents unloading of energy previously stored in the magnetotail, in the form of the westward ring current enhancement and auroral particle precipitation (Davies, 1989). The *recovery phase* follows the main phase and may take several hours or days for the H-component to reach pre-storm levels (Gonzalez *et al.*, 1994).

During a magnetic storm the plasmasphere opens up due to magnetic reconnection and loses its plasma to the magnetotail, depleting plasma in the ionosphere in the processs (Fuller-Rowell *et al.*, 1994). In the process the F2-layer becomes unstable, fragmented and even disappears (Davies, 1989). Three interrelated causal mechanisms are available for explaining storm dynamics: mechanical, electrical and chemical (Kintner *et al.*, 2007). Transitionary electric fields from the solar wind propagate into the inner magnetosphere and to the mid-latitude and low latitude over a 1-2 hour period, leading to ionospheric uplift due to enhanced **E**x**B** drift and increased TEC during the day (Fejer and Scherliess, 1998). The mechanical process begins when the high-latitude thermosphere is heated up by auroral processes (Joule heating). This drives thermospheric winds equatorward, also lifting the ionosphere. Accompanying the thermospheric winds are composition changes in the thermosphere which chemically remove plasma. Understanding the competition among electric fields as well as thermospheric dynamics and composition changes, is required to explain mid-latitude ionospheric storms (Kintner *et al.*, 2007).

Prior to the introduction of GPS-derived ionospheric measurements in South Africa, ionosonde measurements, subject to perturbed ionospheric behaviour under disturbed geomagnetic conditions, remained the only source for investigating storm-time ionospheric behaviour. Preliminary results investigating the November 2004 geomagnetic storm affects on the South African ionosphere by using GPS were first presented by (Cilliers *et al.*, 2005). This storm is investigated in more detail in the following paragraph.

7.4 Methodology for investigating the November 2004 Solar storm

To investigate the development of the geomagnetic storm from 3-16 November 2004, SOHO and GOES data from this period were used to identify solar flares and sunspots associated with large CMEs. Ground based magnetometer data from Hermanus, South Africa for the period 5-16 November 2004 was used to calculate the change in the local geomagnetic field's horizontal (H) component and compared to official Dst index for the same period. Both measurements are in nT and should reveal Sudden Storm commencements (SSCs) due to sudden changes in the ring current. Planetary K-index values were obtained as measure of the severity of the disturbed geomagnetic conditions. IMF field and solar wind speed data were obtained from the ACE satellite for the same period to identify rapid direction changes in the IMF Bz-component and rapid velocity changes in the solar wind. The SOHO, ACE, Dst and H-component observations/measurements were used to correlate flare or CMEs events and shockwave arrivals evidenced in IMF Bz direction change and rapid solar wind speed changes (shock waves), with probable SSCs identified in the Dst and Hermanus H-component data. These results are presented in Table 13.

The ionospheric response to the geomagnetic storm was investigated comparing profilograms from the Grahamstown ionosondes for the period and by comparing changes in diurnal Grahamstown ionosonde-TEC and GPS-TEC calculated from the Sutherland receiver data using ASHA. At the time of this solar storm event, the Grahamstown GPS receiver had not been installed and Sutherland is in sufficient proximity to Hermanus and Grahamstown. Two-dimensional ionosphere GPS-TEC images were also constructed over the country using eight GPS receivers in the CDSM network.

7.5 Results

7.5.1 Storm development

A major sunspot group, AR 10696, with a complex magnetic field produced several Earth-directed CMEs and solar flares from 3-10 November 2004 as observed by SOHO. Comparison of ACE solar wind velocity and IMF z-component (Bz) data, with hourly Dst measurements and groundbased magnetometer data at Hermanus, South Africa, revealed eight identifiable SSCs from 7-12 November (**Figure 51**). The occurrence and magnitude of notable solar events identified by the GOES satellite from 3-10 November were correlated with the identified SSCs to determine the probable events initiating the identified SSCs (Table 13).

Table 13. Notable SSCs and probable solar flare and CME originating events observed in sunspot group AR10696 by SOHO, ACE and GOES in November 2004.

Event	ACE shockwave arrival timing (UTC)	Velocity increase $km.s^{-1}$	IMF Bz (nT)	Minimum Dst (nT)	Probable flare or CME time (UTC)	Class
SSC1	7 Nov 01:54	317 - 365	-5.5	+7	4 Nov 23:19	M5.4
SSC2	7 Nov 10:02	344 - 408	-1.4	-29	5 Nov 11:30	M4.0
SSC3	7 Nov 17:55	490 - 602	+19.8	-90	6 Nov 00:34	M9.3
SSC4	7 Nov 21:51	611 - 660	-44.4	-273	6 Nov 00:51	M5.0
SSC5	9 Nov 09:15,	580 - 750	+4.8	-155	7 Nov 16:06	X2.0
SSC6	9 Nov 18:27	632 - 800	-29.7	-223	8 Nov 03:29	C7.9
SSC7	10 Nov 00:00	small	-31.3	-289	8 Nov 15:49	M2.3
Shock, no SSC	12 Nov 01:26	610 - 715	+9.7	na	9 Nov 17:23	M8.9
SSC8	12 Nov 05:02	small	+7.9	-109	10 Nov 02:13	X2.8

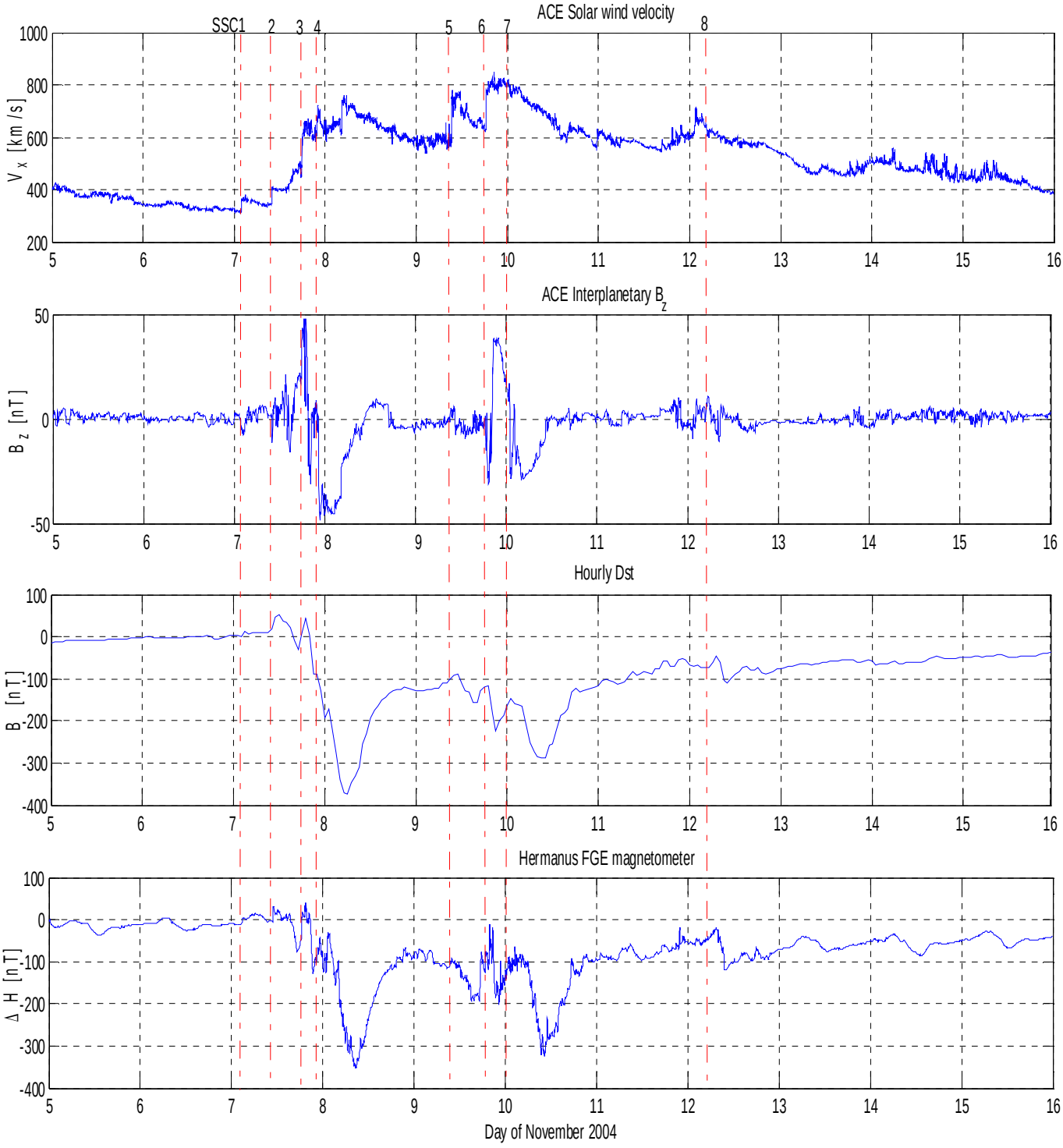

Figure 51 Comparison of solar wind velocity (top), IMF z-component, Dst index and magnetometer H-component changes (bottom) for 5-16 November 2004.

On 7 November, four distinct solar wind shockwaves were observed by the ACE satellite and the IMF was highly variable with several north-south direction changes through the course of the day. The first commencement (01:54 UTC, 7 Nov) was very small and insignificant. Increased solar wind velocity and south-turning Bz initiated the second SSC (10:02UTC, 7 Nov) which saw a prominent initial phase of peak Dst index of +51 nT. The main phase of SSC2, however, was interrupted by SSC3 (17:55 UTC), which initiated another, but smaller, initial phase with +40 nT peak value. The resultant geomagnetic storm severity increased substantially when Bz rapidly swung south from +47.83 nT to -30.9 nT around 19:12 UTC, substantially contributing to the main phase decrease. Increased solar wind velocity and further decreasing Bz (-48.4 nT) at 21:51 UTC initiated another commencement (SSC4) which merged with the main phase of the storm associated with SSC3. The storms associated with SSC2, 3 and 4 contributed significantly to the main phase decrease which ended when Dst reached a minimum of -373 nT at 06:00 UTC on 8 November. No identifiable SSCs were observed on November 8, which saw the main phase and recovery phase of the geomagnetic storm.

Another SSC(5), attributed to the X2.0 flare on 7 November, commenced on 9 November with a shockwave registered at 09:15, the initial phase clearly identifiable. This was followed later in the day by SSC6 around 18:27, probaly due to the C7.9 event on 8 November. The latter associated Dst value of -220 nT was observed around 21:00. These two SSCs followed text-book progression of a geomagnetic storm. Bz gradually turned South between 21:36 on 9 November and 01:24 on 10 November with a rapid southward change between 00:00 and 01:24 on 10 November. This change was not associated with any apparent solar wind shock, but the high solar wind velocity (817km/s) coupled with the rapid southward change in Bz, initiated a strong storm which lasted for the major part of 10 November, registering a minimum Dst of -289 nT around 10:00 on 10 November. Geomagnetic conditions appeared to remain relatively quiet on 11 November with constant solar wind velocity and Bz orientation, a sign of the recovery phase. Around 04:48 on 12 November, Bz started turning South, reaching -10.2 nT at 07:15 and, coupled with the relative high solar velocity (606 km/s) initiated SSC8 which lasted a few hours and reached minimum Dst of -109 nT around 10:00 on 12 November. From the development of SSCs 7 and 8, it appears that an SSC can be

initiated by a southward-turning Bz without an apparent accompanying solar wind shock. Apart from a smaller disturbance later on 12 November, geomagnetic conditions gradually stabilised and Dst gradually increased to -39 nT by 16 November. The severity of the magnetic storm is indicated by the Kp index values illustrated in **Figure 52**.

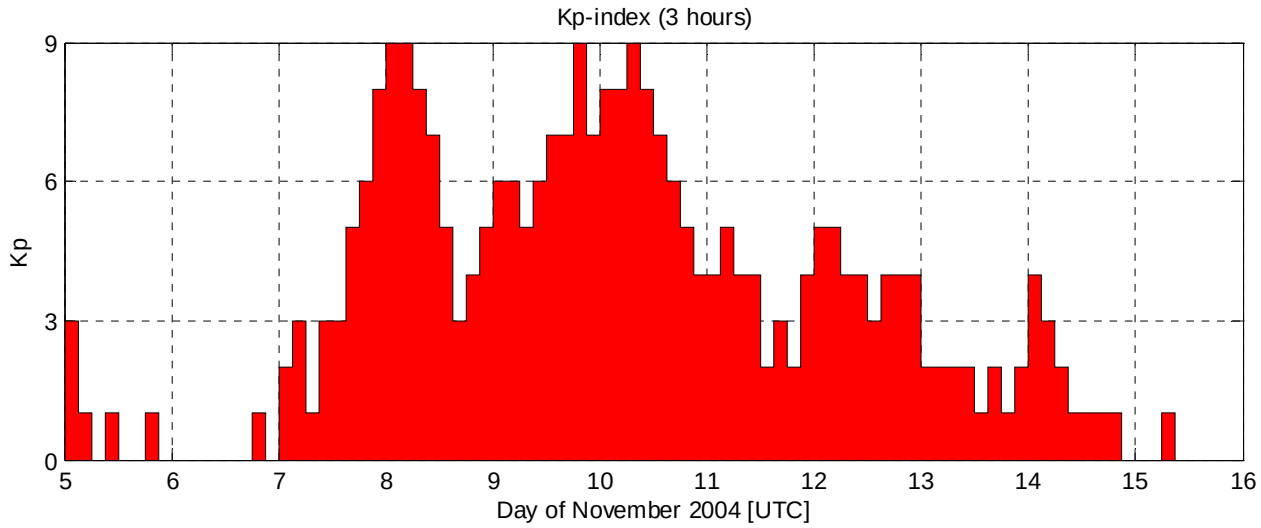

Figure 52. The K_p index indicates the geomagnetic storm intensity for 5-16 November 2004. The high (>6) values indicate severely disturbed geomagnetic conditions for 8, 10 and 11 November.

7.5.2 Ionospheric response

During and following a geomagnetic storm, ionospheric changes around the globe can appear chaotic and both positive and negative changes in ionospheric density are observed, markedly noticeable in the F2-layer. The occurrence of positive or negative ionospheric storm effects show strong local-time dependence (Prölss, 1993) with negative storm effects being the dominant characteristic in the ionospheric response to geomagnetic activity enhancements (Belehaki and Tsagouri, 2001). It is generally accepted that negative storm effects are attributed to neutral composition changes where upwelling and increases in molecular ion species tend to hasten the ion recombination and either slows the rate of increase or causes a decrease in plasma density (Fuller-Rowell *et al.*, 1994).

The increased ionisation associated with positive storms are attributed to the global manifestation of the neutral wind effect starting at auroral latitudes where perturbed interactions between the solar wind and the magnetosphere yield increased energetic particle precipitation, convection electric fields and associated Joule heating. The Joule heating raises the thermosphere temperature at auroral latitudes, resulting in enhanced equatorward winds and travelling ionospheric disturbances (Jodogne and Stankov, 2002).

A negative storm is characterised by decreased electron densities and structure changes in the ionsophere. Studies (Daniell and Strickland, 2001; Crowley *et al.,* 2006), confirmed by satellite-based ultraviolet measurements, attribute the electron density decrease to lower ionisation rates associated with thermosphere wind-driven regions of reduced O/N2 ratios.

The decrease in electron density observed at the Grahamstown ionosonde between 7 and 8 November is clearly visible in the Grahamstown profilogram (**Figure 53**), signifying a negative storm. In **Figure 54** the ionospheric TEC observed by the Grahamstown ionosonde and Sutherland GPS receiver is compared with the Dst and the change in horisontal geomagnetic field component observed at Hermanus. The TEC decrease on 8, 10 and 11 November 2004, associated with the large negative Dst values on 8-10 November, is evident in both ionosonde and GPS data. The "normal" TEC values on November 9 might be attributed to the temporary recovery of the ionosphere as evidenced in the increased H-component, signifying a decrease in the storm-time ring current. The subsequent SSCs, however, resulted in higher recombination and subsequent lower ionisation rates on 10 and 11 November. Finally, the comparison of two-dimensional TEC maps over Southern Africa on 7 and 8 November 2004 (**Figure 55**) illustrates the plasma depletion associated with the negative storm.

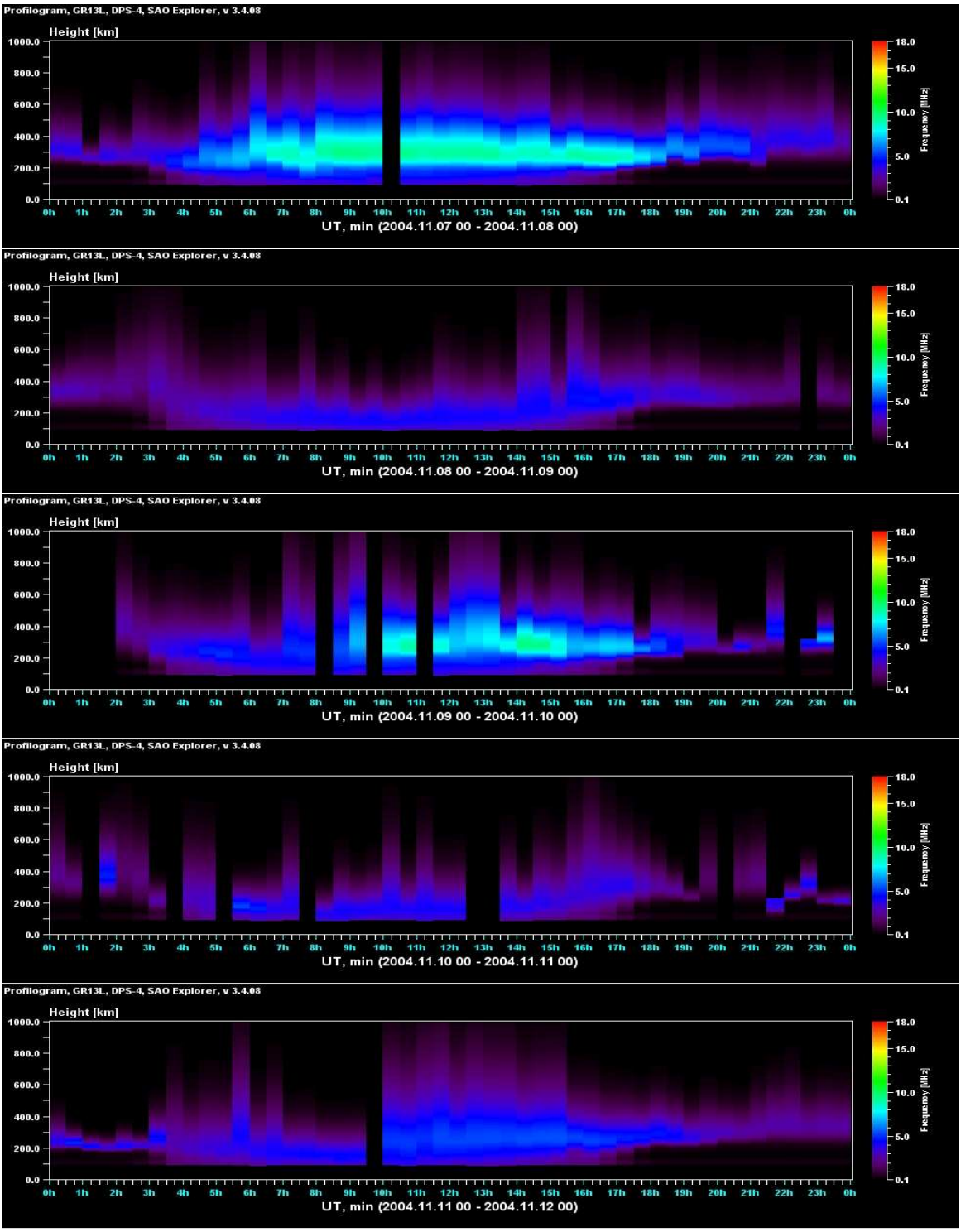

Figure 53 Grahamstown ionosonde profilograms for 7-11 November 2004 (top-bottom). Colour intensity is an indication of the critical plasma frequency, hence electron density, at different altitudes.

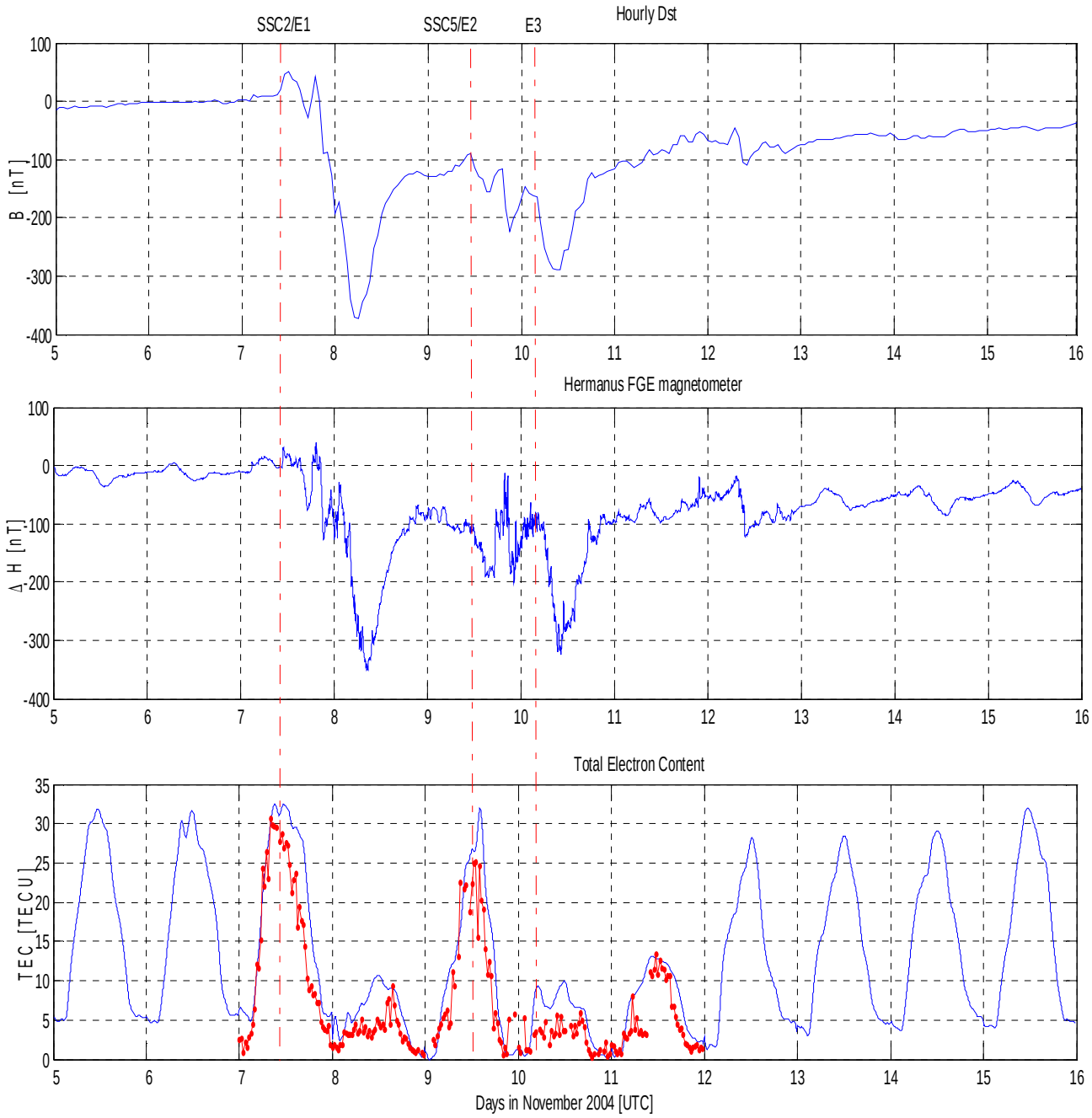

Figure 54. Comparison of hourly Dst index (top), change in the geomagnetic field's horizontal component at Hermanus (middle) and total electron content (bottom) derived from the Sutherland GPS (blue) and Grahamstown ionosonde (red).

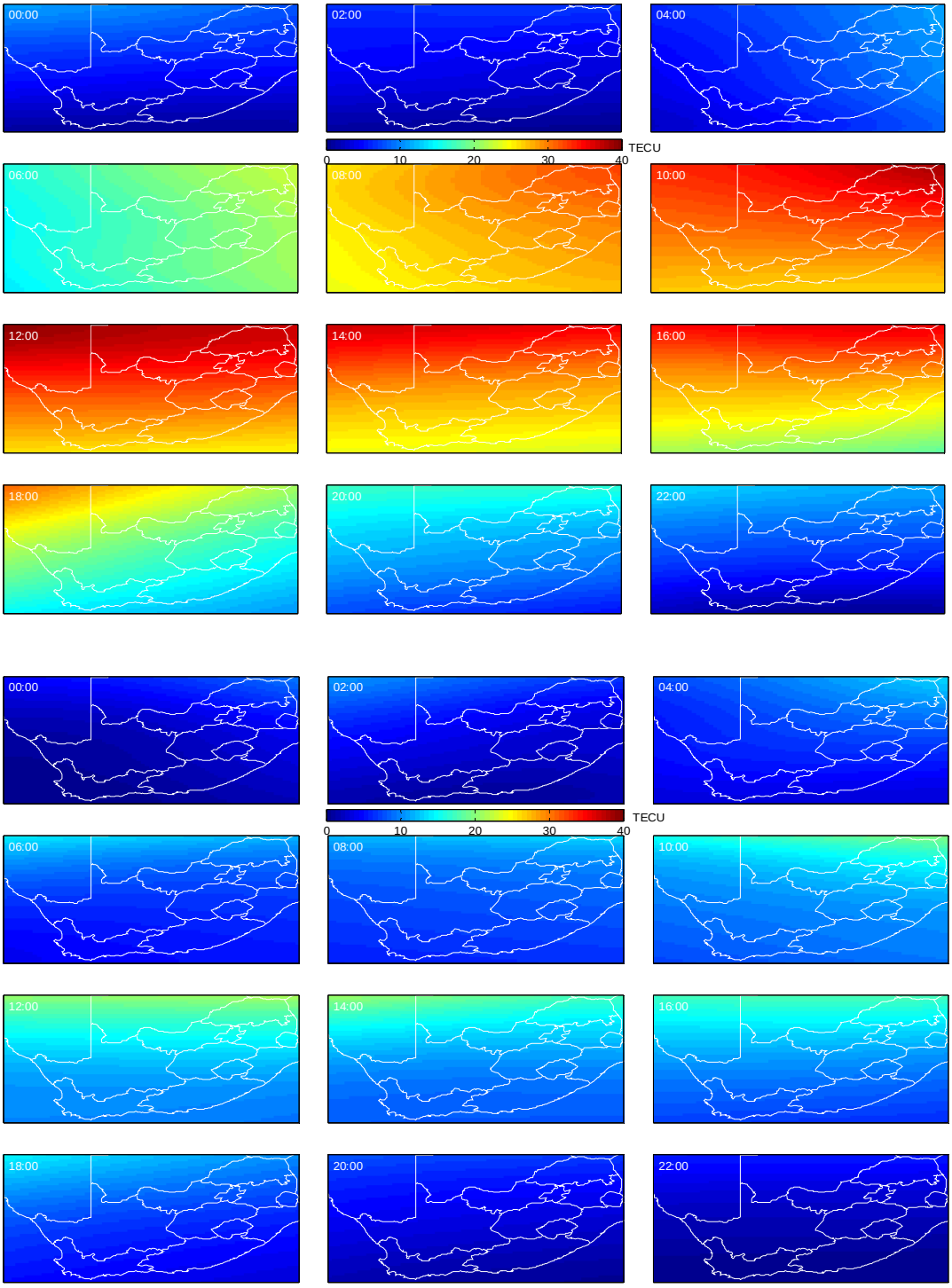

Figure 55. Two-hourly GPS-derived TEC maps for 7 (top) and 8 November 2004 (bottom) illustrate the plasma depletion associated with lower ionisation rates/higher recombination rates during a negative storm.

7.6 Conclusions

In this chapter necessary concepts required for understanding geomagnetic storms were presented. The progress of the 8-12 November 2004 geomagnetic storm was described using results from ground- and space-based instruments. Decreased ionospheric TEC results from ground-based ionospndes and GPS receivers revealed charactersitic of a negative storm. Comparisons of The 2D ionospheric maps for 7-8 November reveal the extent of the plasma depletion and serve to illustrate the ionospheric imaging capability of GPS receivers, something not feasible with a sparse ionosonde network. The demonstration of the GPS-TEC application to investigate mid-latitude ionispheric storms should lay the foundation for further research in this field.

7.7 Future work

To better monitor the change of ionospheric content and to improve our understanding of the latitudinal movement of ionospheric plasma during storms, a longitude meridian of instruments through southern Africa equatorward would supply valuable information. The author suggests a meridian along the west coast through South Africa, Namibia, Angola and further North. Secure locations with sufficient infrastructure at the existing magnetometic observatories at Keetmanshoop and Tsumeb in Namibia might be considered as initial locations for such a new meridian.

Chapter 8

Conclusions and future work

8.1 Conclusions

In this study an overview was given of historic ionospheric research conducted in South African and the state of the art on South Africa ionosonde measurements and their associated time and spatial limitations were discussed. The relevance of GPS-derived ionospheric TEC as supportive measurements for improving the time and spatial resolution of ionosonde soundings were presented and the difference between global and regional GPS-derived TEC models were discussed and several state of the art models discussed. The propagation of GPS signals through the ionosphere was discussed and relevant ionospheric phase advance and group delay equations and geometry-free equations were presented. An adjusted spherical harmonic-based TEC model using ionospheric delay observations observed by a network of South African dual frequency GPS receivers and expressed in a Sun-fixed longitude and adjusted co-latitude co-ordinate system was derived, tested and evaluated. The performance of the ASHA model to estimate time-varying one and two-dimensional TEC values from a single receiver and multiple receivers respectively was extensively evaluated by comparison with simulated data, ionosonde measurements and two independent GPS methodologies. Results of the developed ASHA model were also compared with TOPEX/Poseidon and Jason-1 satellite-based measurements. Comparisons with ionosonde measurements and the other GPS methodologies were encouraging, but for the T/P and Jason-1 test cases, the results were inconclusive as biases in T/P have been pointed out in other studies. The practical application of the presented model was demonstrated in two studies; an ionospheric stability investigation in support of South Africa's SKA bid and the ionospheric response to a severe geomagnetic storm in November 2004. From the

encouraging test case and practical studies' results it may be concluded that the presented model is well suited for estimating ionospheric TEC from a regional network of dual frequency GPS receivers.

8.2 Future work

The presented ASHA model might be further refined by incorporating a slab thickness model, investigating alternative latitude scaling factors and by comparing estimated satellite and receiver DCBs with those derived from alternative methods, including methods involving hardware/electronic procedures.

The investigation of mid-latitude geomagnetic storms and their driving mechanisms is an important research field requiring urgent attention. It is proposed that a longitude GPS receiver chain, co-located with magnetometers, be installed along the African west coast equatorward to improve and densify ionospheric measurements. The presented ASHA or CSHA GPS-TEC models could subsequently be used to investigate latitudinal TEC changes from the magnetic equator in a southward direction.

An immediate and pressing application of the presented GPS-TEC model is its near real-time implementation for South African space physics and radio astronomy applications. To this end, the author has established a near real-time GPS data dissemination and access system between CDSM in Cape Town and the HMO in Hermanus (**Figure 56**), approximately 120 km apart. This system involves an HMO computer (HMO-1) set up at CDSM which receives a continuous 1 Hz GPS data stream from 23 South African GPS receivers. After every five minutes, the most recent five minutes' data from all these receivers are sub-sampled to 30 seconds, compressed into a single file and copied to the CDSM ftp-server (ftp:///www.trignet.co.za/GPS_Downloads/HMO). A software script running on HMO-2 in Hermanus retrieves this compressed file *via* ftp within 2-3 minutes after the previous five-minute time-stamp. On successful download, the previous five minutes' GPS RINEX files for each of the 23 receivers are reconstructed from the compressed file and made available for near real-time use. This system is presently operational. It is foreseen that a real-time version of ASHA, running on HMO-3, will retrieve the most recently reconstructed GPS data to update the Jacobian from an existing twenty-four hour solution by removing the oldest five-minutes observations and

updating the Jacobian with the latest five-minutes observation, advancing a new solution at five-minute intervals. Resultant two-dimensional TEC maps will then be published on the HMO web-server in support of space weather studies or related disciplines. Analyses indicate that state of the art bandwidth and computational infrastructure permits an updated solution within five minutes with realistic 10-15 minute latency.

Though a substantial historic South African TEC database was established during the SKA ionospheric stability study, it was restricted to a region in the Northern Cape Province. All historic South African GPS data should be processed to extend the existing database.

Access to GPS receivers in neighbouring Southern African countries should be pursued to extend the TEC mapping region to cover Southern Africa up to the equator. This will permit investigation of ionospheric dynamics over the sub-continent.

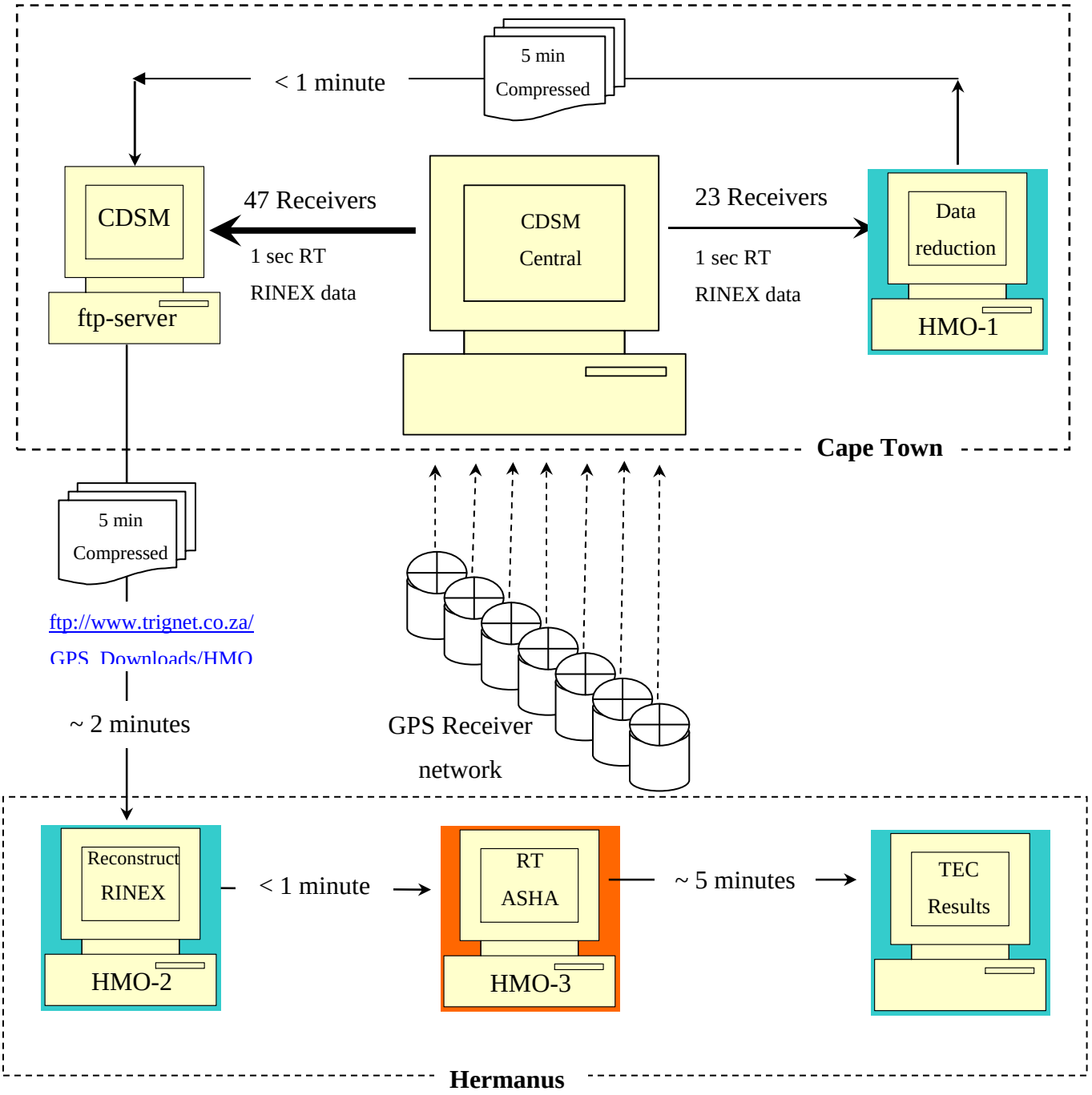

Figure 56. Schematic presentation of the existing near real-time GPS data dissemination infrastructure from CDSM in Cape Town to the Hermanus Magnetic Observatory in Hermanus, South Africa. Given bandwidth limitations and processing resources, near real-time TEC maps with 10-15-minute latency may be realistically realised.

Appendix A

Relevant GPS co-ordinate transformations

Relevant GPS co-ordinate systems and transformations referred to in Chapter 3. (Grewel, 2001; Hofmann-Wellenhof, 2001). These parameters are required to propagate satellite positions from broadcast ephemerides.

Table A.1 GPS broadcast ephemeris

Parameter	Description	Units
M_0	Mean anomaly at reference time	rad
Δn	Mean motion difference from calculated value	rad/s
E	Orbit eccentricity	dimensionless
$\sqrt{a}$	Square root of semi-major axis	$m^{1/2}$
Ω_0	Right ascension of ascending node (RAAN) at weekly epoch	rad
I_0	Inclination angle at reference time	rad
ω	Argument of perigee	rad
$\dot{\Omega}$	Rate of change of RAAN	rad/s
$\dot{i}$	Rate of change of inclination	rad/s
C_{uc}	Amplitude of cosine harmonic correction term to arg. of latitude	rad
C_{us}	Amplitude of sine harmonic correction term to arg. of latitude	rad
C_{rc}	Amplitude of cosine harmonic correction term to radius	m
C_{rs}	Amplitude of sine harmonic correction term to radius	m
C_{ic}	Amplitude of cosine harmonic correction term to inclination	rad
C_{is}	Amplitude of sine harmonic correction term to inclination	rad

t_{0e}	Ephemeris reference time	s
Af_0	Satellite clock offset	s
Af_1	Satellite clock drift	s/s
Af_2	Satellite clock frequency drift	s/s^2

Table A.2 Algorithm for propagating GPS satellite position

$n_0 = \sqrt{\frac{\mu}{a^3}}$	Mean motion
$\Delta t = t - t_{0e}$	Time elapsed from reference epoch
$n = n_0 + \Delta n$	Corrected mean motion
$M = M_0 + n\Delta t$	Corrected mean anomaly
$M = E - e\sin E$	Kepler's equation; Solve iteratively for eccentric anomaly, E
$\nu = \cos^{-1}\left(\frac{\cos E - 1}{1 - e\cos E}\right)$	True anomaly
$\theta = \nu + \omega$	Argument of latitude
$\delta_u = C_{uc}\cos 2\theta + C_{us}\sin 2\theta$	2^{nd} harmonic perturbation correction to argument of latitude
$\delta_r = C_{rc}\cos 2\theta + C_{rs}\sin 2\theta$	2^{nd} harmonic perturbation correction to radius
$\delta_i = C_{ic}\cos 2\theta + C_{is}\sin 2\theta$	2^{nd} harmonic perturbation correction to inclination
$u = \theta + \delta_u$	Corrected argument of latitude
$r = a(1 - e\cos E) + \delta_r$	Corrected radius
$i = i_0 + \delta_i + \dot{i}\Delta t$	Corrected inclination
$x_p = r\cos u$ $y_p = r\sin u$	x, y co-ordinates in orbital plane

$\Omega = \Omega_0 + \left(\dot{\Omega} - \dot{\Omega}_e\right)\Delta t - \dot{\Omega}_e t_{0e}$	Corrected right ascension of ascending node
$X = x_p \cos\Omega - y_p \cos i \sin\Omega$	
$Y = x_p \sin\Omega - y_p \cos i \cos\Omega$	Satellite ECEF co-ordinates
$Z = y_p \sin i$	

8.3 Co-ordinate Transformations

A1. ECEF to ENU

The ENU co-ordinate system is defined as a local horizontal system with X-axis pointing East, Y-axis pointing North and Z-axis pointing vertically up, normal to the horizontal plane. This system is used for defining co-ordinates relative to a fixed position on the Earth's surface. A similar axis system is the North-East-Down (NED), which relates to ENU through an axis shift:

$$\mathbf{ENU} = \begin{bmatrix} 0 & 1 & 0 \\ 0 & 0 & 1 \\ 1 & 0 & 0 \end{bmatrix} \mathbf{NED}\text{, i.e. } \mathbf{ENU} = [\mathbf{S}]\mathbf{NED}$$

Transformation from ECEF to ENU involves a translation and two axes rotations.

Let

$\mathbf{r}_{ECEF}^{S}$ denote the satellite's ECEF position

$\mathbf{r}_{ECEF}^{R}$ denote the receiver's ECEF position

Translation:

Shift satellite axis origin to receiver origin

$$\mathbf{r} = \mathbf{r}_{ECEF}^{S} - \mathbf{r}_{ECEF}^{R}$$

Rotation:

Rotate the resulting vector 1) about the Z-axis through λ, 2) about the Y-axis through $-\phi$ and 3) shift axis from NED to ENU:

$$\mathbf{r}_{ECEF}^{ENU} = \mathbf{S} \cdot \mathbf{R}_y(-\phi) \cdot \mathbf{R}_z(\lambda) \cdot \mathbf{r}$$

$$\mathbf{r}_{ECEF}^{ENU} = \begin{bmatrix} 0 & 1 & 0 \\ 0 & 0 & 1 \\ 1 & 0 & 0 \end{bmatrix} \cdot \begin{bmatrix} \cos\phi & 0 & \sin\phi \\ 0 & 1 & 0 \\ -\sin\phi & 0 & \cos\phi \end{bmatrix} \cdot \begin{bmatrix} \cos\lambda & \sin\lambda & 0 \\ -\sin\lambda & \cos\lambda & 0 \\ 0 & 0 & 1 \end{bmatrix} \cdot \mathbf{r}$$

$$\mathbf{r}_{ECEF}^{ENU} = \begin{bmatrix} -\sin\lambda & \cos\lambda & 0 \\ -\sin\phi\cos\lambda & -\sin\phi\cos\lambda & \cos\phi \\ \cos\phi\cos\lambda & \cos\phi\sin\lambda & \sin\phi \end{bmatrix} \cdot \mathbf{r}$$

A2. Angular position

A satellite's Cartesian position in a local origin frame, such as the ENU, affords the means to calculate its position in spherical co-ordinates, azimuth, elevation, range. Let the satellite's position in the ENU frame be denoted by $\mathbf{r} = [X\ Y\ Z]^T$, then range, r, is defined as the geometrical distance between satellite and receiver:

$$r = \|\mathbf{r}\| = \sqrt{X^2 + Y^2 + Z^2}$$

Elevation is defined as the angular distance of the satellite above the observer's local horizon and is calculated as

$$\theta = \sin^{-1}(Z / r).$$

Azimuth is defined as the angle measured from True North to the horizontal component of **r**, over East and calculated as

$$\alpha = \text{atan2}(Y, X)$$

Note: atan2 is a software version of the inverse tan function which returns the angle α in the correct quadrant.

A3. Ionospheric Pierce Point (IPP) geographic co-ordinates

For a given receiver location (λ, ϕ), satellite azimuth and elevation angles (α, θ) and assumed shell height H, the IPP sub-point's geographic position (λ_{ipp}, ϕ_{ipp}), is calculated as follows:

Calculate the suspended Earth-angle, ψ, between the satellite, geocentre and receiver position:

$$\psi = \frac{\pi}{2} - \theta - \sin^{-1}\left(\left(\frac{R_e}{R_e + H}\right) \cdot \cos\theta\right)$$

IPP latitude:

$$\sin\phi_{ipp} = \sin\phi\cos\psi + \cos\phi\sin\psi.\cos\alpha$$

IPP longitude:

IF $\phi >$ 70° AND $\tan(\psi.\cos\alpha) > \tan\left(\frac{\pi}{2} - \phi\right)$

OR

IF $\phi <$ -70° AND $-\tan(\psi.\cos\alpha) > \tan\left(\frac{\pi}{2} + \phi\right)$

THEN

$$\lambda_{ipp} = \lambda + \pi - \sin^{-1}\left(\frac{\sin\psi.\sin\alpha}{\cos\phi_{ipp}}\right)$$

OTHERWISE

$$\lambda_{ipp} = \lambda + \sin^{-1}\left(\frac{\sin\psi.\sin\alpha}{\cos\phi_{ipp}}\right)$$

A4. ECEF to Geocentric co-ordinates

Transform ECEF co-ordinates to geographic co-ordinates

Latitude (geocentric): $\phi = \text{atan2}\left(Z_{ecef}, \sqrt{X_{ecef}^2 + Y_{ecef}^2}\right)$

Longitude: $\lambda = \text{atan2}\left(Y_{ecef}, X_{ecef}\right)$

A5. Geocentric latitude to geodetic latitude

$r = \sqrt{X^2 + Y^2 + Z^2}$

$P = \sqrt{X^2 + Y^2}$

Initial estimates for latitude and geodetic height

$\phi' = a\sin(Z/r)$

$h = r - a\left(1 - f \cdot \sin\phi'^2\right)$

Iterate until $\left|dP^2 + dZ^2\right| < \varepsilon$

set $\phi = \phi'$

$N_\phi = \dfrac{a}{\sqrt{1 - e^2 \sin^2\phi}}$

$dP = P - \left(N_\phi + h\right) \cdot \cos\phi$

$dZ = Z - \left(N_\phi(1 - e^2) + h\right) \cdot \sin\phi$

$h = h + dZ \cdot \sin\phi + dP \cdot \cos\phi$

$\phi' = \phi + \left(dZ \cdot \cos\phi - dP \sin\phi\right) / \left(N_\phi + h\right)$

Appendix B

GPS Infrastructure

The GPS infrastructure of South Africa's Chief Directorate Surveys and Mapping is given in the table below. All receivers sample and store data at 1Hz. Non real-time receivers operate between 03:00-18:00 SA Standard Time. Data is archived at CDSM in Cape Town and at the HMO in Hermanus.

Station Code	Station name	Real-time	Longitude	Latitude
ANTH	Aliwal North	No	26.71601958	-30.6798096
BETH	Bethlehem	Yes	28.33416251	-28.2497714
BFTN	Bloemfontein	Yes	26.29781312	-29.10368331
BWES	Beaufort West	No	22.57356064	-32.8473825
CALV	Calvinia	Yes	19.76195407	-31.48207443
DEAR	De Aar	Yes	23.99269333	-30.66521083
DRBN	Durban	Yes	30.94667286	-29.96501359
ELDN	East London	Yes	27.8286806	-33.03813399
ERAS	Ellisras	Yes	27.69608784	-23.68666974
ERME	Ermelo	Yes	29.98384688	-26.49781008
GDAL	Groblersdal	No	29.41208168	-25.16145951
GEOR	George	Yes	22.38164178	-34.0014195
GFNT	Graaff Reinet	No	24.53450628	-32.24805144
GRHM	Grahamstown	Yes	26.50717005	-33.32006564
HERM	Hermanus	Yes	19.22305933	-34.42463455
KLEY	Kimberley	Yes	24.80646827	-28.74299075
KMAN	Kuruman	No	23.43247572	-27.46078462
KSTD	Kroonstad	No	27.24007606	-27.66358108
LGBN	Langebaan	Yes	18.15775901	-32.97249178
LSMH	Ladysmith	No	29.78148486	-28.55765614
MBRG	Middelburg	No	29.45420828	-25.77375894
MBRY	Mowbray	Yes	18.46854358	-33.95143815
MFKG	Mafikeng	Yes	25.53996986	-25.80518769
NSPT	Nelspruit	Yes	30.97516799	-25.47534017
NYLS	Nylstroom	No	28.40599618	-24.70299721
PBWA	Phalaborwa	No	31.13432659	-23.95150859
PELB	Port Elizabeth	Yes	25.61101643	-33.98455435
PMBG	Pietermaritzburg	Yes	30.38326646	-29.60072944
PRET	Pretoria	Yes	28.28263226	-25.73203014
PSKA	Prieska	No	22.74928998	-29.66680392
PTBG	Pietersburg	No	29.4657001	-23.92321009
QTWN	Queenstown	No	26.92166017	-31.90810524
SBOK	Springbok	Yes	17.87920868	-29.66932771
SPRT	Steelpoort	Yes	30.18522553	-24.67152353
TDOU	Thohoyandu	Yes	30.38400598	-23.07991352
ULDI	Ulundi	No	31.42092324	-28.29311986
UMTA	Umtata	Yes	28.67250571	-31.54877162
UPTN	Upington	Yes	21.25586903	-28.41365008

Appendix C
Kalman Filter

A Kalman filter is a stochastic optimization technique which effectively combines (noisy) sensor measurements with an uncertain (linear) time-dependent dynamic model, to render an optimised solution of required parameters (states, state vector). In the estimation process, the measured and modelled observations are weighed according to the data quality with stronger weights assigned to good measurements (low noise) and, during periods of poor or no measurements, stronger weights are assigned to modelled observations. At each time increment, a linear operator is applied to the state vector to generate a new state, with some noise mixed in and optionally, some information from the controls of the system. The Kalman filter assumes the true state at time *k* is evolved from the state at (*k*-1) according to the *system equation* (Strang and Borre, 1997):

$$\mathbf{x}_k = \mathbf{F}_k \mathbf{x}_{k-1} + \mathbf{B}_k \mathbf{u}_k + \mathbf{w}_k$$

where

$\mathbf{F}_k$ state transition model applied to previous state $\mathbf{x}_{k-1}$

$\mathbf{B}_k$ control-input model applied to control vector $\mathbf{u}_k$

$\mathbf{w}_k \sim N(0, \mathbf{Q}_k)$ process noise assumed to be derived from zero mean multivariate normal distribution with covariance $\mathbf{Q}_k$

At time *k* a measurement (observation), $\mathbf{b}_k$ of the true state $\mathbf{x}_k$, is made according to the *observation equation*:

$$\mathbf{b}_k = \mathbf{H}_k \mathbf{x}_{k-1} + \mathbf{v}_k$$

where

$\mathbf{H}_k$ state observation model, which maps the true state space into observed space

$\mathbf{v}_k \sim N(0, \mathbf{R}_k)$ observation noise assumed to be zero mean Gaussian noise with covariance $\mathbf{R}_k$

The Kalman filter is a recursive estimator, i.e. it only requires the current measurement and the estimated state from the previous time step to compute the state estimate for the current step. The update process is expressed in two stages, *viz.*, a *prediction* and *correction* (filtering) stage of the two Kalman filter variables, $\hat{\mathbf{x}}_{k|k}$ the state estimate at time k and $\mathbf{P}_{k|k}$, the error covariance matrix (measure of estimated accuracy of estimated state).

Prediction:

State $$\hat{\mathbf{x}}_{k|k-1} = \mathbf{F}_k \hat{\mathbf{x}}_{k-1|k-1} + \mathbf{B}_k \mathbf{u}_k$$

Error covariance matrix $$\mathbf{P}_{k|k-1} = \mathbf{F}_{k|-1} \mathbf{P}_{k-1|k-1} \mathbf{F}_{k|-1}^{\mathrm{T}} + \mathbf{Q}_{k-1}$$

Correction:

State $$\hat{\mathbf{x}}_{k|k} = \hat{\mathbf{x}}_{k|k-1} + \mathbf{K}_k \left(\mathbf{b}_k - \mathbf{H}_k \hat{\mathbf{x}}_{k|k-1} \right)$$

Error covariance matrix $$\mathbf{P}_{k|k} = \mathbf{K}_k \left(\mathbf{I} - \mathbf{K}_k \mathbf{H}_k \right) \mathbf{P}_{k|k-1}$$

The gain matrix $\mathbf{K}_k$ is given by

$$\mathbf{K}_k = \mathbf{P}_{k|k-1} \mathbf{H}_k^{\mathrm{T}} \left(\mathbf{H}_k \mathbf{P}_{k|k-1} \mathbf{H}_k^{\mathrm{T}} + \mathbf{R}_{k-1} \right)^{-1}$$

It is assumed that the initial state, $\mathbf{x}_0$ and noise vectors, $\mathbf{w}_j$ and $\mathbf{v}_j$ at each step are mutually independent and that the initial condition $\mathbf{x}_0$ is a random variable with a given mean

$$E\left(\mathbf{x}_0\right) = \hat{\mathbf{x}}_0 \text{ and covariance } E\left(\mathbf{x}_0 - \hat{\mathbf{x}}_{0|0}\right)\left(\mathbf{x}_0 - \hat{\mathbf{x}}_{0|0}\right)^{\mathrm{T}} = \mathbf{P}_{0|0}$$

Bibliography

Baker D. Ionosonde Stations in Southern Africa – A review of Current Status and Future Prospects. Proceedings of Session G6 at the URSI XXIVth General Assembly. Phil Wilkinson (Ed.). Kyoto, Japan. August 25-September 2, 1993.

Baker DN. Coupling Between The Solar Wind, Magnetosphere, Ionosphere And Neutral Atmosphere. Laboratory for Atmospheric and Space Physics. University of Colorado, Boulder, CO 80309. Booklet. 2004

Baumjohann W and Treumann RA. *Basic Space Plasma Physics*. Imperial College Press. ISBN 1-86094-079-X. 1999.

Belehaki A and Jakowski N. Comparison of Ionospheric Ionisation Measurements Over Athens Using Ground Ionosonde And GPS-Derived TEC Values. *Radio Science*. Vol 38 No 6. 2003.

Belehaki A, Jakowski N and Reinisch B. Study Of The Plasmaspheric Electron Content Using Ionosonde Derived ITEC And GPS TEC Values. Proc. 34th COSPAR Scientific Assembly, Second World Space Congress. Houston, TX, USA. October 2002.

Belehaki A and Tsagouri I. Study of the thermospheric-ionospheric response to intense geomagnetic storms at middle latitudes. *Physics and Chemistry of the Earth*, Part C. Vol 26, No 5. pp 353-357. January 2001.

Benada JR. PO.DAAC Merged GDR (TOPEX/POSEIDON) Generation B (MGDR-B) User's Handbook. Doc No D-11007. Vers. 2.0. July 1997.

Beutler G, Bauersima I, Botton S, Gurtner W, Rothacher M and Schildknecht T. Accuracy and Biases in the Geodetic Application of the Global Positioning System. *Manuscripta Geodaetica*, 14, pp28-35. 1989.

Beutler G. Extracting information concerning the ionosphere using the IGS network. EOS Transactions of the American Geophysical Union. Vol 76, No 17, Supplement, p86 (abstract). 1995.

Bilitza D. International Reference Ionosphere 2000. *Radio Science.* Vol 36 No 2. Pp 261-275. 2001.

Carpenter DL and Park CG. On What Ionospheric Workers Should know about the Plasmapause-Plasmasphere. *Reviews of Geophysics and Space Physics*, Vol. 11, No.1, Pp 133-154, February 1973.

Chappel CR. Recent Satellite Measurements of the Morphology and Dynamics of the Plasmasphere. *Reviews of Geophysics and Space Physics*, Vol. 10, No.4, Pp 951-979, November 1972.

Chen FF. *Introduction to Plasma Physics and Controlled Fusion*. Volume 1: Plasma Physics. Plenum Press. ISBN 0-306-41332-9. 1984.

Cilliers PJ, Gouws D, Opperman B, Wonnacott RT, Combrinck L. The South African network of dual frequency global positioning system satellite receiver base stations - a national asset with many applications and research opportunities, *South African Journal of Science,* Vol 99(1/2), pp 51-55, Jan/Feb 2003.

Cilliers PJ. Feasibility Study: Mapping and predicting the ionosphere using GPS signals, *Research Report Doc No: 6010-0001-711-A1, for Grintek Ewation*, 2003/02/07.

Cilliers PJ and Opperman BDL. Determination of the Total Electron Content and the vertical electron density in the Ionosphere, Phase 2, Research Report Doc No: 6010-0002-711-A1, 2003/08/28.

Cilliers PJ, Opperman B**,** Mitchell CN. Electron density profiles determined from tomogaphic reconstruction of total electron content obtained from GPS dual frequency data: First results from the South African network of dual frequency

GPS receiver stations, *Advances in Space Research, Vol 34/9, pp*. 2049-2055, November 2004.

Cilliers PJ and Opperman BDL. Real-time Determination of the Electron Density Distribution in the Ionosphere over South Africa Using Signals from a Single Dual Frequency GPS Receiver, Research Report Doc No: 6010-0001-712-A1, 2005/02/18.

Cilliers PJ, Opperman BDL, McKinnell LA and Mitchell CN. Investigations into ionosphere-plasmasphere coupling during a severe magnetic storm over South Africa. Abstract In: Proceedings URSI General Assembly, New Deli, India, 23-29 Oct 2005.

Coco DS, Coker CE, Dahlke SR and Clynch JR. Variability of GPS satellite differential group delay biases. *IEEE Trans. Aerosp. Electron. Syst.* 27(6), pp931-938, 1991.

Coster AJ, Foster JC, Erickson PJ, Rich FJ. Regional GPS mapping of storm-enhanced density during the 15-16 July 2000 geomagnetic storm. *In: Proceedings of ION GPS 2001*. Salt Lake City, Utah, pp2531-2539. 11-14 September 2001.

Daniell RE Jnr and Strickland DJ. Modeling negative ionospheric storm effects caused by thermospheric disturbances observed in UV satellites. *Journal of Gephysical research*, Vol 106, No 12, pp30307 – 30313. December 2001.

Davies, K. *Ionospheric Radio*. IEE Electromagnetic Wave Series 31. Short Run Prss Ltd, UK. ISBN 0 86341 186 X. 1989.

De Franceschi G, De Santis A and Pau S. Ionospheric Mapping By regional Spherical Harmonic nalysis: New Developments. *Advances in Space Research*. Vol 14 No 12. Pp 61-64. 1994.

De Santis A, De Franceschi G, Zolesi B, Pau S and Cander LR. Regional Mapping Of The Critical Frequency Of The F2 Layer By Spherical Cap Harmonic Expansion. *Annales Geophysicae*. Vol 9. Pp 401-406. 1991.

De Santis A. Conventional Spherical Harmonic Analysis For Regional Modelling Of The Geomagnetic Field. *Geophysical Research Letters*. Vol 9 No 10. Pp 1065-1067. 1992.

Du J., Caruana J., Wilkinson P, Thomas R, and Cervera M., Determination of Equatorial Ionospheric Scintillation S4 by dual frequency GPS. *Proceedings from Workshop on the Application of Radio Science.* La Trobe University, Australia, 27–29 April 2000.

Escobal PR. *Methods of Orbit Determination*. Krieger Publishing Co., Malabar, California. ISBN 0-88275-319-3. 1985.

Fejer BG and Schrliess. Mid- and low-latitude prompt-penetration ionospheric zonal plasma drifts. *Geophysical Research Letters*, 25(16), pp3071-3074. 1998.

Feltens J. Chapman Profile Approach for 3D Global TEC Representation. *In: Proceedings of the 1998 IGS Analysis Centres Workshop*, ESOC, Darmstadt, Germany, February 9-11, Pp. 285-297. 1998

Foster JC and Rideout W. Mid-latitude TEC enhancements during October 2003 superstorm. *Geophysical Research Letters*, 32, L12S04, doi:10.1029/2004GL021719. Vol 25, No 16. 2005

Frei E and Beutler G. Rapid Static Positioning Based on the Fast Ambiguity Resolution Approach FARA: Theory and First results. *Manuscripta Geoaetica*. Vol. 15, pp 325-356. 1990.

Fu LL, Christensen EJ, Yamarone Jr CA, Lefebrre M, Menard Y, Dorrer M and Escudier P. TOPEX/Poseidon mission overview. *Journal Geophysical Research*, 99, 24369, 1994.

Fuller-Rowell TJ, Codrescu MV, Moffet RJ and Quegan S. Response of the thermosphere and ionosphere to geomagnetic storms. *Journal of Geophysical Research*. Vol. 99, No A3. pp 3893-3914. 1994.

Fuller-Rowell T, Araujo-Pradere E, Minter C, Codrescu M, Spencer P, Robertson D and Jacobson AR. US-TEC: A new data assimilation product from the Space Environment Center characterising the ionosphere total electron content using real-time GPS data. *Radio Science*, Vol 41, No 6, RS6003, doi:10.1029/2005RS002293, 2006.

Fuller Rowell T. Quoted in "Strange Space Weather over Africa". NASA headline news (http://science.nasa.gov/headlines/y2007/). 13 November 2007.

Gao Y, Heroux P and Kouba J. Estimation of GPS receiver and satellite L1/L2 signal delay biases using data from CACS. KIS94, *Proceedings of the International Symposium on Kinematic Systems in Geodesy, Geomatics, and Navigation*. Banff, Alberta, 30 August-2 September, Department of Geomatics Engineering, The University of Calgary, Calgary, Alberta, Pp. 109-117. 1994.

Gao Y and Liu ZZ. Precise Ionosphere Modeling Using Regional GPS Network Data. *Journal of Global Positioning Systems*, Vol 1, No. 1:18-24. 2002.

Georgiadou Y and Kleusberg A. On the effects of Ionpsheric delay on Geodetic Relative GPS Positioning, *Manuscripta Geodaetica*, 13, pp1-8. 1988.

Ginzberg ,VL. The Propagataion of Electromagnetic Waves in Plasmas. 2nd Ed. Pergamon Press. 1970.

Gledhill JA and Szendrei ME. The behaviour of the F-region of the ionosphere over Grahamstown during the solar eclipse of the 14th January 1945, *Trans. Roy. Soc. S. Africa*, Vol. 31, pp. 147-152, 1947.

Gledhill JA. Thirty years of upper atmosphere research work at Rhodes, Part I, *The Radio Scientist*, Vol. 2, pp. 106-112, 1991.

Gonzalez WD, Joselyn JA, Kamide Y, Kroehl HW, Rostoker G, Tsurutani BT and Vasyliunas VM. What is a geomagnetic storm? *Journal of Geophysical Research*. Vol. 99, No A4, pp 5771-5792, April 1994.

Grewel MS, Weill LR and Andrews AP. *Global Positioning Systems, Inertial Navigation and Integration*. Wiley and Sons, Inc. Publication. ISBN 0-471-35032. 2001.

Haggard R. Particle precipitation effects in the daytime E-region in the South Atlantic Anomaly region. *South African Journal of Science*. Vol 100. November - December 2004.

Hajj GA, Wilson B, Wang C, Pi X and Rosen. Data assimilation of ground GPS TEC into a physics-based ionospheric model by use of Kalman filter. Radio Science 39, RS1S05, doi:10.1029/2002RS002859, 2004.

Hargreaves JK. The Solar-Terrestrial Environment. Cambridge University Press. Cambridge Atmospheric And Space Sciences Series. 1992.

Hernandez-Pajares M, Juan JM and Sanz J. New approaches in global ionospheric determination using ground GPS data, *Journal of Atmospheric and Solar Terrestrial Physics*, Vol 61, pp 1237-1247, 1999.

Hewitt F J (Miss), Hewitt J and Wadley T L. A frequency prediction service for South Africa, *Trans. SAIEE*, Vol. 38, pp. 180-197, July 1947.

Ho CM, Wilson BD, Mannucci AJ, Lindqwister UJ and Yuan DN. A Comparitive Study of Ionospheric Total Electron Content Measurements using Global Ionospheric Maps of GPS, TOPEX Radar and the Bent Model. *Radio Science*, Vol 32, Number 4, Pp1499-1512, Jul-Aug 1997.

Hobiger T, Kondo T and Schuh H. Very long baseline interferometry as a tool to probe the ionosphere. *Radio Science*, Vol. 41, RS1006, doi:10.1029/2005RS003297, 2006

Hofmann-Wellenhof B, Lichtenegger H and Collins J. *GPS Theory and Practice*, Fifth Ed. ISBN 3-211-83534-2. Springer. 2001.

Horel J. Karoo Array Telescope manager. Personal communication. November 2007.

Huang X and Reinisch BW. Vertical electron density profiles from the digisonde network. *Advances in Space Research*, Vol 18, No 6, pp121-129. 1996.

Hunsucker RD. Radio Techniques for Probing the Terrestrial Ionosphere. Physics and Chemistry in Space 22, Planetology. Springer-Verlag. ISBN 3-540-53406-7. 1991.

Imel DA. Evaluation of TOPEX/Poseidon dual frequency ionospheric correction. Journal Geophysical Research, Vol 99 No C12, p 24895, December 1994.

International SKA Project Office. Request for proposals for Siting the SKA. Version 13 2004.

Jansky KG. Directional studies of atmospherics at high frequencies. *Proceedings of the IRE*. Vol 20, p.1920. 1932.

Jansky KG. Electrical Disturbances Apparently of Extraterrestrial Origin. *Proceedings of the IRE*. Vol 21, No.10, Pp 1387 – 1398. Oct. 1933.

Jee G, Schunk RW and Scherliess. Analysis of TEC data from the TOPEX/Poseidon mission. *Journal of Geophysical Research*, Vol 109, A01301, doi:10.1029/2003JA010058, 2004.

Jodogne JC and Stankov SM. Ionosphere-plasmasphere response to geomagnetic storms studied with RMI-Dourbes comprehensive database. Annals of Geophysics. Vol 45, No 5. October 2002.

Kivelson MG and Russel CT. Introduction to Space Physics. Camridge University Press. ISBN 0-521-45104-3. 1995.

Kelley MC and Heelis RA. The Earth's Ionosphere. Plasma Physics and Electrodynamics. Vol 43 in the International Geophysics Series. Academic Press. ISBN 0-12-404012-8. 1989.

Kintner P, Coster A, Fuller-Rowell T and Mannucci AJ. Overview of Mid-latitude Ionospheric Storms. *EOS Transactions* AGU, Vol 88 No 37, pp358-359. 11 Sep 2007.

Klobuchar JH, Bishop GJ and Doherty PH. Total electron content and L-band amplitude and phase scintillation measurements in the polar cap ionosphere. In: Propagation

effect on Military Systems in the High latitude region. NATO AGARD Conference Proceedings No 382. 1985.

Klobuchar JA. Design and Characteristics of the GPS Ionospheric Time Delay Algorithm for Single-Frequency Users. Proceedings of the PLANS-86 Conference, Las Vegas, NV, 4-7 November, pp. 280-286, 1986.

Komjathy, A., R.B. Langley, and F. Vejrazka. Assessment of Two Methods to Provide Ionospheric Range Error Corrections for Single-frequency GPS Users. GPS Trends in Precise Terrestrial, Airborne, and Spaceborne Applications. *In: Proceedings of International Association of Geodesy Symposium*. No. 115, , Springer Verlag, New York, pp. 253-257. Boulder, CO, 3-4 July 1995.

Komjathy A and Langley RB. The effect of Shell Height on High Precision Ionospheric Modelling Using GPS. *In: Proceedings of the IGS Analysis Center Workshop*. Silver Spring, Maryland USA. RE Neilan et al. (Ed), pp 193-203. IGS Central Bureau, JPL, Pasadena, California, USA. March 19-21. 1996.

Komjathy, A. and R.B. Langley. An Assessment of Predicted and Measured Ionospheric Total Electron Content Using a Regional GPS Network. *In: Proceedings of the National Technical Meeting of the Institute of Navigation*, Santa Monica, CA, pp. 615-624, 22-24 January 1996

Komjathy A. Global ionospheric Total Electron Content Mapping Using the Global Positioning System. Ph.D Thesis, University of New Brunswick, Frederiction, New Brunswick, Canada. Department of Geodesy and Geomatics Engineering Technical Report No. 188. 1997.

Komjathy A, Sparks L, Wilson BD and Mannucci. Automated daily processing of more than 1000 ground-based GPS receivers for studying intense ionospheric storms. *Radio Science*, Vol (4), RS6006, doi:10.1029/2005RS003279, 2005.

Krauss JD. *Radio Astronomy*, 2nd Edition. Cygnus-Quasar Books. 1986.

Kühn C.J. Riometer absorption events at L=4 (Sanae, Antarctica) during years 1964 to 1966. PhD Dissertation. Northwest University, Potchefstroom, South Africa. 1968.

Liu Z, Skone S, Gao Y and Komjathy A. Ionpsheric Modelling using GPS data. *GPS Solutions*, doi:10.1007/s10291-004-0129-z, Vol 9, Number 1, pp63-66, April 2005.

Lanyi G and Roth T. A Comparison Of Mapped And Measured Total Ionospheric Electron Content Using Global Positioning Systems And Beacon Satellite Observations. *Radio Science*. Vol 4 No 23. Pp 483-492. 1988.

Ma G and Maruyama T. Derivation of TEC and estimation of instrumental biases from GEONET Japan. *Annales Geophysicae*, Vol 21 No. 10, pp 2083-2093. 2003.

Mannucci AJ, Wilson BD and Edwards CD. Global maps of ionospheric total electron content using the IGS GPS network (abstract). EOS Trans. AGU, 73(43), Spring meeting Suppl. 127, 1992.

Mannucci AJ, Wilson BD and Edwards CD. A New Method For Monitoring The Earth's Ionospheric Total Electron Content Using The GPS Global Network. *In: Proceedings Institute of Navigation*. Vol 2 No GPS-93. Pp1323-1332. 1993.

Mannucci AJ, Wilson BD and Yuan DN. Monitoring Ionospheric Total Electron Content using the GPS global network and TOPEX/Poseidon altimeter data. *In: Proceedings of the Beacon Satellite Symposium*, Ed (L Kersley), pp338-346, University of Wales, Aberystwyth, 1994.

Mannucci AJ, Wilson BD, Yuan DN, Ho CH, Lindqwister UJ and Runge TF. A global mapping technique for GPS-derived ionospheric total electron content measurements. *Radio Science*, Vol. 33, pp. 565-582, 1998.

Mannucci AJ, Wilson BD, Lindqwister UJ, Runge TF, Iijima BA, Edwards CD Jr, Sparks L, Reyes M, Muellerschoen RJ and Pi X. Generating Maps of the Ionosphere from GPS Measurements. NASA TECH BRIEF Vol. 25, No. 6, 6 Jan 2001.

Mannucci AJ, Tsurutani BT, Ikjima BA, Komjathy A, Saito A, Gonzalez WD, Guarnieri FL, Kozyra JU and Skoug R. Dayside global ionosphere response to the major interplanetary events of October 29-30, 2003, "Halloween storms". *Geophysical Research Letters*, 32, L12S02, doi:10.1029/2004GL021467. 2005

Mazzella AJ, Holland EA, Andreasen AM, Andreasen CC, Rao GS and Bishop GJ. Autonomous Estimation Of Plasmasphere Content Using GPS Measurements. *Radio Science*. Vol 37 No 6. 2002.

McKinnell Lee-Anne. *A neural network based ionospheric model for the bottomside electron density profile over Grahamstown, South Africa*. PhD thesis, Rhodes University. 2003.

McKinnell Lee-Anne and Poole AWV. Neural network-based ionospheric modelling over the South African region. *South African Journal of Science*, 100 (11 & 12). pp. 519-523. 2004.

McNamara LF. *The Ionosphere*: Communications, *Surveillance and Direction Finding*. Kriegler Publishing Company. Malibar California. 1991.

Mercer CC. The search for an ionospheric model suitable for real-time applications in HF radio communications. MSc thesis, Rhodes University, Grahamstown, South Africa. 1994.

Meeus J. *Astronomical Algorithms*. Willman-Bell, Inc. Richmond Virginia, 23235, ISBN 0-943396-35-2. 1991.

Mitchell CN and Spencer PS. Development of tomographic techniques for large scale ionospheric imaging. *In: Proceedings of ionospheric effects symposium*. JM Goodman (Ed), pp601-608, Natl. Tech. Inf. Serv. , Springfield Va. 2002.

Mitchell CN and Spencer PS. A Three dimensional Time-dependent Algorithm for Ionospheric Imaging. *Ann. Geophysics-ITALY*. Vol 46 No 4. Pp 687-. 2003.

Miyazaki S, Saito T, Sasaki M, Hatanaka and Iimura Y. Expansion GSI's nationwide GPS array. Bull. Geogr. Surv. Inst. 43, pp23-34, 1997.

Montenbruck and Gill E. *Satellite Orbits. Models, Methods, Applications.* Springer. ISBN 3-540-67280-x. 2000.

Newby SP. *An Assessment of Empirical Models for the Prediction of the Transionospheric Propagation Delay of Radio Signals*. M.Sc. thesis. Department of Surveying Engineering Technical Report No. 160, University of New Brunswick, Fredericton, N.B., Canada. 1992.

Odijk D. *Fast Precise GPS Positioning In The Presence Of Ionospheric Delays*. Netherlands Geodetic Commission, Delft, Netherlands. Publications on Geodesy 52. 2002. ISBN 906132 278 2.

Opperman BDL. Methodology for the Estimation and Mapping of Total Electron Content in the Ionosphere Using Dual Frequency GPS signals, *Research Report Doc No: 6010-0002-728-A1, for Grintek Ewation*, 2003/08/28.

Opperman BDL. Version Description Document For The Enhancement of Matlab Simulation of GPS Satellites and Determination of Ionospheric Total Electron Content (TEC) From Actual GPS data, *Research Report Doc No: 6010-0002-432-A1*, for Grintek Ewation, 2003/08/28.

Opperman BDL and Cilliers PJ. Test Result Record: The TECSIM Software (Version 2.0) for Predicting and Mapping The Ionosphere using GPS Signals, *Research Report Doc No: 6010-0002-722-A1*, for Grintek Ewation, 2003/08/29.

Opperman BDL and Cilliers PJ. GPS Technology: A New Resource For Space Physics Applications. *In: Proceedings 49th South African Institute of Physics Conference*. Bloemfontein June 2004.

Opperman BDL, Cilliers PJ and McKinnell LA. Information and analysis of ionospheric conditions at proposed SKA sites, *HMO Research Report Doc No: 6021-0001-709-A1, for SKA Bid Committee*, 19 July 2005.

Opperman BDL, Cilliers PJ, McKinnell LA and Haggard R. Development of a Regional GPS-based Ionospheric TEC model for South Africa. *Advances in Space Research*. Pp 808-815, Vol. 39, 2007.

Otsuka Y, Ogawa T, Saito A, Tsugawa T, Fukao S and Miyazaki S. A new technique for mapping of total electron content using GPS network in Japan. *Earth, Planets and Space*. Vol. 54, No1, pp. 63-70. 2002.

Papagiannis MD and Mullaney H. The Geographical distribution of the ionospheric evening anomaly and ist relation to the global pattern of neutral winds. Journal of Atmosphere and Terrestrial Physics 33, Pp 451-459. 1971.

Pi X, .Mannucci AJ, Lindqwister UJ and Ho CM. Monitoring of global ionospheric irregularities using the worldwide GPS network. Geophysical Research Letters, Vol. 24, No. 18, Pp 2283–2286, 1997.

Ping J, Matsumoto K, Shum C, Saito A, Callahan P and Heki K. Validation of JASON-1 nadir ionosphere TEC using GEONET. *Marine Geodesy*. Vol 27 No 3-4. Pp 741-752. 2004.

Poole AWV and Evans GP. Advanced sounding: (ii) First results from an advanced chirp ionosonde. *Radio Science*, Vol. 20, Pp. 1617-1623, 1985.

Poole AWV. Advanced sounding: (i) The FMCW alternative. *Radio Science*, Vol. 20, Pp. 1609-1616, 1985.

Poole AWV. Thirty years of upper atmosphere research work at Rhodes, Part II, *The Radio Scientist*, Vol. 2, pp. 112-114, 1991.

Prölss GW. On explaining the local time variation of ionospheric storm effects. Annales Geophysicae, Vol 11, pp 1-9, 1993.

Ratcliffe JA. The early days of ionospheric research. The early ionosphere investigations by Appleton and his colleagues. Phil. Trans. R. Soc. London. A. 280, pp 3-9. 1975.

Reber G. Galactic Radio Waves. *Sky and Telescope*. Vol.8, No.6, April, 1949.

Reinisch BW and Huang X. Deducing topside profiles and total electron content from bottomside ionogramms. *Advances in Space Research*. Vol 27. Pp 23-30. 2001.

Reinisch BW, Huang X, Belehaki A and Ilma R. Using scale heights derived from bottomside ionograms for modelling the IRI top side profile. *Advances in Radio Science*. Vol 2. Pp 293-297. 2004.

Rideout W and Coster A. Automated GPS processing for global Total Electron Content Data. GPS Solutions (2006)10. pp219-228. doi 10.1007/s10291-006-0029-5. 2006.

Rishbeth H and Garriott OK. *Introduction to Ionospheric Physics*. Academic Press. New York. 1969.

Rishbeth H, Zou L, Müller-Wodarg ICF, Fuller-Rowell TJ, Millward GH, Moffett RJ, Indenden DW and Aylward AD. Annual and semiannual variations in the ionospheric F2-layer: II Physical discussion. *Annales de geophysique* 18, pp 945-956. 2000.

Rohlfs K and Wilson TL. Tools of Radio Astronomy, 4th Edition, Springer 2006.

Royden HN, Miller RB and Buennagel LA. Comparison of NAVSTAR satellite L band ionospheric calibrations with Faraday rotation measurements. *Radio Science* 19(3), pp798-804, 1984.

Runge T, Lindqwister U, Mannucci AJ, Reyes M, Wilson BD and Yuan D. Generation of GPS Observables for Global Ionospheric Mapping, Presented at the AGU Spring Meeting 1995, Eos Trans, AGU, 76(17), Spring Meet. Suppl., S87, 1995.

Saito A, Fukao S and Miyazaki S. High resolution mapping of TEC perturbations with the GSI GPS network over Japan. Geophysical Research Letters, Vol 25 pp 3079-3082. 1998.

Sardon E, Rius A and Zarraoa N. Estimation of the transmitter and receiver differential biases and the ionospheric total electron content from Global Positioning System

observations, *Radio Science*, Vol. 29, Number 3, Pages 577-586, May-June 1994.

Schaer S, Beutler G, Mervart L, Rothacher M and Wild U. Global And Regional Ionosphere Models Using The GPS Double Difference Phase Observable. *Proceedings 1995 IGS workshop*, Potsdam, Germany. May 1995.

Schaer S, Beutler G, Rothacher M, Springer TA. Daily Ionosphere Maps Based on GPS Carrier Phase Data Routinely Produced by the CODE Analysis Center. Astronomical Institute, University of Berne, Switzerland. 1996.

Schaer S., Gurtner W and Feltens J. IONEX: The IONosphere Map EXchange Format Version 1. *Proceedings of the IGS AC Workshop*, Darmstadt, Germany. February 9-11 1998.

Schaer S. Mapping And Predicting the Earth's Ionosphere Using the Global Positioning System. *PhD dissertation*. Astronomical Institute, University of Berne, Berne, Switzerland. March 1999.

Scherliess L, Schunk RW, Sojka JJ and Thompson DC. Development of a Physics-Based Reduced State Kalman Filter for the Ionosphere. *Proceedings of 2002 Ionospheric Effects Symposium*. Ed. J.M. Goodman, JMG Associates, Alexandria, VA, 2002.

Scherliess L, Schunk RW, Sojka JJ and Thompson DC, Development of a Physics-Based Reduced State Kalman Filter for the Ionosphere, *Radio Science*, 39, RS1S04, doi:10.1029/2002RS002797, 2004.

Scherliess L, Schunk RW, Sojka JJ, Thompson DC and Zhu L. The USU GAIM Gauss-Markov Kalman Filter Model of the Ionosphere: Model Description and Validation. *Journal of Geophysical Research*, Vol 111, A11315, doi:10.1029/2006JA011712..

Schunk RW, Scherliess L, Sojka JJ and Thompson DC. Global Assimilation of Ionospheric Measurements (GAIM). *Proceedings of 2002 Ionospheric Effects Symposium*. Ed. J.M. Goodman, JMG Associates, Alexandria, VA, 2002.

Schunk RW, Scherliess L, Sojka JJ, Thompson DC and Zhu L. An Operational Data Assimilation Model of the Global Ionosphere. In: Proceedings of 2005 Ionospheric Effects Symposium. Ed. J.M. Goodman, JMG Associates, Alexandria, VA, 2005.

Seeber G. *Satellite Geodesy: Foundations, Methods and Applications*. Walter de Gruyter, Berlin New York. 1993.

Seidelmann, P. (Ed.). *Explanatory Supplement to the Astronomical Almanac*. University Science Books, Sausalito, California. ISBN 0-935702-68-7. 1992.

Sekido M, Kondo T, Kawai E and Imae M. Evaluation of GPS-based ionospheric TEC map by comparing with VLBI data. RADIO SCIENCE, VOL. 38, NO. 4, 1069, doi:10.1029/2000RS002620, 2003 .

SKA steering commitee. Requirements for the Ionospheric Condition at the SKA Radio Telescope sites: Request for Information and scope of Work., April 2005.

Stoker, PH. Riometer absorption and spectral index for precipitating electrons with exponential spectra. *Journal of Geophysical Research* Vol 92, Pp 5961-5968. 1987.

Spencer PSJ, Robertson DS and Mader GL. Ionospheric data assimilation methods for geodetic applications. Paper presented at IEEE PLANS 2004, Inst. Of Electron. And Electr. Eng., Montery, Calif., Apr. 2004.

Strang G and Borre K. Linear Algebra, Geodesy and GPS. Wellesley-Cambridge Press. ISBN 0-9614088-6-3. 1997.

Taylor GB, Carilli CL and Perley RA (Editors). *Synthesis Imaging in Radio Astronomy II.* Astronomical Society of the Pacific Conference Series. 1999

Thompson AR, Moran JM and Swenson GW. *Interferometry and Synthesis in Radio Astronomy*, 2nd Edition. Wiley-VCH. 2004.

Torr DG, Richards PG and Torr MR. Ionospheric composition: The seasonal anomaly explained. In: *AGARD The Physical Basis of the Ionosphere in the Solar-Terrest. System*. Dominici P and Zolesi B (Eds). SEE N81-23507 14-42. Feb 1981.

Vallado DA. Fundamentals of Astrodynamics and Applications. McCraw-Hill. Space Technology Series. 1997. ISBN 0-07-066834-5.

Wadley T L. A single-band 0-20-Mc/s ionosphere recorder embodying some new techniques, *Proc. Instn. Elect. Engrs.*, Pt. III, Vol. 96, pp. 483-486. 1949.

Walker ADM. The SHARE Radar at Sanae Antarctica. *South African Journal of Science*. Vol. 98, No 5-6, Pp. 257-263. 2002.

Walt M. *Introduction to Geomagnetically TrappedRadiation*. Cambridge University Press. Cambridge Atmospheric And Space Sciences Series. 1994. ISBN 0-521-43143-3.

Wang C., Hajj G., Pi X, Rosen IG and Wilson BD. Development of the Global Assimilative Ionospheric Model. *Radio Science*. Vol 39 No 1. 2004.

Webb PA and Essex EA. A Simple Model of the Ionosphere Plasmasphere System. *Proceedings of the Workshop on Applications of Radio Science, WARS97*, Barossa Valley, Australia. Kulessa A, James G, Bateman D and Tobar M (Eds). Pp 190-195. September 21 - 23, 1997.

Wielgosz P, Grejner-Brzezinska D and Kashani I. Regional Mapping with Kriging and Multiquadratic Methods. Journal of Global Positioning Systems. Vol 2, No 1, pp48-55. 2003.

Wild U. Ionosphere and Satellite Systems: Permanent GPS Tracking Data for Modelling and Monitoring. *Geodatisch-geophysikalische Arbeiten in der Sweiz*. Vol 48. 1994.

Wilson A, Stoker PH and Mathews MJ. The 64-beam imaging riometer array on Vesleskarvet, Antarctica. 1, Evaluation of the viewing directions. SA Journal Science. Volume 98 No. 5/6 May/June 2002.

Wilson BD, Mannucci AJ, Edwards CD and Roth T. Global Ionospheric Maps using a global network of GPS receivers. *In: Proceedings of the International Beacon Satellite Symposium*, Cambridge MA, July 6-10, 1992.

Wilson BD and Mannucci AJ. Instrumental Biases in Ionospheric Measurements derived from GPS data. *Proceedings Institute of Navigation*. Vol 2 No GPS-93. Pp 1343-1351. 1993.

Wilson BD and Mannucci AJ. Extracting ionospheric measurements from GPS in the presence of anti-spoofing. Proceedings of the 7th International Technical Meeting of the Satellite Division of The Institute of Navigation, Salt Lake City , Utah, 20-23 September 1994, The Institute of Navigation, Alexandria, Va., ION GPS-94, Vol. 2, pp. 1599-1608. 1994.

Wilson BD, Mannucci AJ and Edwards CD. Subdaily Northern Hemisphere Ionopheric Maps using an extensive network of GPS receivers. Radio Science. Vol 3 No 30. Pp 639-648. 1995.

Wilson, BD, Mannucci AJ, Yuan D, Christian H, Pi X, Runge T and Lindqwister U. Global Ionospheric Mapping Using GPS: Validation and Future Prospects. *Proceedings of the 1996 IGS Workshop*, Silver Spring, MD, 19-21 March 1996.

Yunck T, Liu CH and Ware R. A History of GPS Sounding. Applications of Constellation Observing System for Meteorology, Ionosphere and Climate. Springer-Verlag. Hong Kong. 2001.

Zhao C, Shum CK , Yi Y, Ge S, Bilitza D and Callahan P. Accuracy Assessment of the TOPEX/Poseidon Ionosphere Measurements. *Marine Geodesy*. Volume 27, Number 3-4 / July-December 2004.

Zumberge JF, Liu R and Neilan RE (Eds). International GPS Service for Geodynamics 1994 Annual report. JPL Publication 95-18, p329. 1994.

Internet Resources

[AIPS++] Astronomical Information Processing System. http://aips2.nrao.edu/weekly/docs/aips++.html

[CDSM] Chief Directorate Surveys and Mapping. http://w3sli.wcape.gov.za

[DCB] Inter-frequency (differential) clock bias for all GPS satellites ftp://ftp.unibe.ch/aiub/CODE/

[GAIM] Global Assimilitve Ionospheric Model. http://iono.jpl.nasa.gov

[GEONET] GPS Earth Observation Network http://stegps.kugi.kyoto-u.ac.jp/tec-cgi

[GMRT]. Great Metrewave Radio Telescope. http://www.gmrt.ncra.tifr.res.in/

[IGSCB] ftp://igscb.jpl.nasa.gov/pub/product/

[IRI] International Reference Ionosphere Model of National Space Science Data Center, Greenbelt, Maryland, ftp://nssdcftp.gsfc.nasa.gov/models/ionospheric/iri/

[NGDC] National Geophysical Data Center www.ngdc.noaa.gov

[PO.DAAC]. Physical Oceanography Distributed Active Archive Center http://podaac-www.jpl.nasa.gov/cdrom/mgdr-b/Document/HTML/usr_toc.htm

[RINEX] The Receiver Independent Exchange Format, Werner Gurtner, Astronomical Institute, University of Berne http://pangea.stanford.edu/GP289/rinex.format or ftp://igscb.jpl.nasa.gov/igscb/data/format/rinex210.txt

[SOPAC] Scripps Orbit and Permanent Array Center http://sopac.ucsd.edu

[SPIDR] Space Physics Interactive Data Resource http://spidr.ru.ac.za/spidr/

[TEQC] TEQC: The Toolkit for translation, editing, and quality checking of GPS/GLONASS data http://www.unavco.ucar.edu/software/teqc/teqc.html

[Trignet] South African permanent GPS network operated by Chief Directorate Surveys and Mapping (CDSM) www.trignet.co.za

[US_TEC] United States Total Electron Content www.sec.noaa.gov/ustec